Nonlinear Screening of External Charge by Doped Graphene

by

Mahmoudreza Ghaznavi

A thesis
presented to the University of Waterloo
in fulfillment of the
thesis requirement for the degree of
Master of Mathematics
in
Applied Mathematics

Waterloo, Ontario, Canada, 2010

I hereby declare that I am the sole author of this thesis. This is a true copy of the thesis, including any required final revisions, as accepted by my examiners.

I understand that my thesis will be made electronically available to the public.

Abstract

In the first part of this thesis we discuss some details of properties of graphene and we explain the tight-binding approach to find the energy spectrum in graphene. In the second part of the thesis, we solve a nonlinear integral equation for the electrostatic potential in doped graphene due to an external charge, arising from a Thomas-Fermi (TF) model for screening by graphene's π electron bands. In particular, we study the effects of a finite equilibrium charge carrier density in graphene, non-zero temperature, non-zero gap between graphene and a dielectric substrate, as well as the nonlinearity in the band density of states. Effects of the exchange and correlation interactions are also briefly discussed for undoped graphene at zero temperature. Results from the nonlinear model are compared with results from both the linearized TF model and the dielectric screening model within the random phase approximation (RPA). In addition, the image potential of the external charge is evaluated from the solution of the nonlinear integral equation and compared to the results of linear models. We have found generally good agreement between the results of the nonlinear TF model and the RPA model in doped graphene, apart from Friedel oscillations in the latter model. However, relatively strong nonlinear effects in the TF model are found to persist even at high doping densities and large distances of the external charge.

Acknowledgements

I express my gratitude to my supervisors Prof. Zoran L. Mišković, and Prof. Frank O. Goodman, who have been very good friends, excellent advisors, and with whom it has been a pleasure and privilege to work. I thank them for their excellent advice and donation of their time. My research was greatly improved by the high standards with which my supervisors conduct their own work.

During this project I also benefitted from useful discussions with Prof. Matthew Scott and Prof. Marek Stastna, and here I thank them.

I also acknowledge my beloved parents, brothers and sisters, for their love and support, without which I should not have succeeded. I am forever indebted to them.

I also acknowledge all of my friends who helped to make my period of study here more satisfying.

Dedication

To my beloved parents.

Contents

List of Figures

Chapter 1

Introduction

1.1 History and Motivation

Carbon is the most fascinating element in nature. Because of the flexibility of their bonding, carbon atoms are able to form many different structures. Carbon is the fundamental element in organic chemistry and is the basis for the existence of life as we know it. There are also many different systems made of only carbon atoms. Diamond and graphite are known from antiquity, but some of the other structures of carbon networks, e.g. fullerenes [1, 2, 3] and nanotubes [4], were discovered 10-20 years ago. The different physical properties of different allotropes of carbon originate, in great part, from the dimensionality of those structures. However, we have been studying the theory of the systems with fewer or more than 3 dimensions for more than 50 years, but before discovering the nanotubes, it seemed that in nature we are stuck with three spatial dimensions. For example, physicists have studied the physical properties of layered semiconductors, as a two dimensional system, but any layered semiconductor has a thickness of typically from 10 to 100 atomics layers. In 2004, a research group led by Andre Geim and Kostya Novoselov [5], at the University of Manchester, succeeded in obtaining graphene, which is a one atom thick sheet of carbon atoms. They used an unusual approach to isolate graphene, starting with three dimensional graphite, and extracted a single graphene layer. Graphite may be viewed as a stack of graphene layers weakly coupled together by van der Waals forces. Therefore by pressing graphite against a SiO_2 substrate, one produces graphene stacks, and somewhere among them, there could be individual graphene. Because electron microscopy cannot distinguish monolayers from nanometer thick flakes, it cannot help much in finding individual graphene; on the other hand, the atomic-force and scanning-tunneling microscopes need an atomically smooth substrate to provide the required atomic resolution to detect the step

between the substrate and the monolayer of graphene. The optical properties of graphene allow its observation with an optical microscope [6]. The interference pattern on the reflected light from the substrate, produced by layers of graphene, provides a visible contrast, such that the human eye can detect it using an optical microscope. This simple method makes large (up to 100 μm in size) and high quality graphene crystallites. However, although these high quality crystals are sufficient for physical studies, proof-of-concept devices, and electronic circuits, the drawing technique is not appropriate for industrial-scale applications.

Graphene is one of the best studied carbon allotropes theoretically. It is the starting point for studying graphite, carbon nanotubes and fullerenes. Graphene is made of a honeycomb structure of carbon atoms. Fullerenes may be assumed as wrapped-up graphene, where, replacing some of the hexagons of the graphene lattice by pentagons creates the needed curvature defects; therefore, from a physical point of view, they are considered as zero dimensional objects with discrete energy states. Carbon nanotubes may be viewed as rolled graphene along a given direction and reconnected carbon bonds, and may be considered as one dimensional systems. Graphite, made out of a stack of graphene layers, has been known for a long time. However, graphene was isolated in 2004 for the first time, while P. R. Wallace in 1946 [7] studied the band structure of graphene as a starting point to study graphite, and he showed the unusual semimetallic behavior of graphene. A simple nearest-neighbor tight-binding approximation (see the next chapter), describes the electronic structure of graphene. The symmetry of the honeycomb lattice causes electrons in graphene to mimic a relativistic behavior, i.e., the speed of electrons is independent of the momentum; in other words, electrons act like massless particles, so-called massless Dirac fermions. Because of this similarity of the graphene hamiltonian to that of massless relativistic particles, it has many properties related to

relativistic quantum mechanics. For example, an interesting feature of a massless Dirac fermion is its ability to penetrate a potential barrier of any height and width without making a reflective component; in other words, the transmission probability is 1. This effect, which is called the Klein paradox and predicted decades ago in quantum electrodynamics, has never been observed in particle physics experiments. But it occurs in graphene routinely, in the tunneling of Dirac fermions without reflection through potential barriers and contributes to enhance graphene's conductivity.

Since 1991, the research on nanotubes has led to many applications. The similarity between graphene and nanotubes, and the unusual electronic properties of graphene, makes it a promising candidate in many electronic applications. Some possibilities that comes to mind are as follows: using its tunability by an external electric field in superconductivity and in ultra-sensitive chemical detectors, using its robustness and light weight in micromechanical resonators, and using its atomic thinness in field emitters and in transparent membranes for electron microscopy. Because of the negligible spin-orbit interaction, graphene is a promising candidate for spin-value transistors [8], where spin polarization should survive over submicron distances.

Another possibility for graphene application is that it may be a replacement for silicon in smaller integrated circuits. Because of the stability and conductivity of graphene at the molecular scales, it may be scaled down even to a single benzene ring to be used in the circuits. The ultranarrow strips of graphene, nanoribbons, may behave as semiconductors with gaps due to quantum confinement of electrons [9], which make it possible to have graphene based semiconductors, operating in the same way as silicon based ones.

Graphene may be used in some other applications such as gas sensors. It has

been shown [10] that graphene can absorb gas molecules from the environment, which leads to doped graphene with electrons or holes depending on the nature of the absorbed gas. One can find the concentrations of gases by measuring the change in resistivity of graphene.

Over the period of just 5 years since its first inception in the laboratory [5], graphene has developed into one of the currently most active research areas in the nano-scale physics [11]. One of the most important, and certainly most elusive, problems in graphene research is concerned with its electrical conductivity, especially in the regime close to zero doping of graphene, where the conductivity exhibits a peculiar minimum [12, 13, 14, 15, 16]. Besides several other scattering mechanisms for charge carriers in graphene, it is believed that a special role in graphene's conductivity is played by the carrier scattering on charged impurities, which are ubiquitous in graphene's surroundings. In that context, significant progress has been made in understanding the conductivity of graphene by using the Boltzmann transport theory for charge carrier scattering on linearly screened charged impurities within the random phase approximation (RPA)[17, 18, 19]. However, because of the reduced dimensionality, and especially because of the semi-metallic nature of graphene's π electron bands, the problem of screening of charged impurities remains open. In that context, other approaches have also been undertaken, including a full scattering theoretical treatment of Coulomb impurities embedded within the graphene plane [20, 21, 22, 23], as well as nonlinear screening of external charges studied by means of the Thomas-Fermi (TF) [24, 25, 26, 27], Thomas-Fermi-Dirac (TFD) [28], and Density Functional Theoretical (DFT) schemes [29].

While graphene's applications in nanoelectronics are primarily concerned with charged impurities trapped in an insulating substrate [30, 31], screening of external charges is also of interest for sensor applications of graphene in detecting atoms

or molecules [10], which may be either adsorbed on the upper surface of graphene [32, 33], or intercalated in the gap between the graphene and the substrate [34]. Further applications include image-potential states of electrons near graphene [35, 36], as well as the image and friction forces on slowly moving ions that may affect the kinetics of chemical reactions taking place in the vicinity of graphene [27, 37]. All these aspects of screening of external charges by graphene are expected to be strongly influenced by the presence of nearby dielectric materials [38, 39, 40, 41, 42].

One of the most important issues in theoretical studies of screening of external charges is concerned with applicability of the linear response theory for intrinsic, or undoped, graphene. Namely, with its valence and conducting π electron bands touching each other only at the K and K' points of the Brillouin zone [11], graphene behaves as a zero-gap semiconductor, so that its polarizability is greatly reduced when its Fermi level lies close to the neutrality point characterizing the regime of zero doping. In that context, it was shown within the RPA approach that screening of external charges by intrinsic graphene at $T = 0$ is characterized merely by a renormalization of graphene's background dielectric constant due to inter-band electron transitions [17, 43, 44]. However, when graphene is doped up to a certain number density n (per unit area) of charge carriers, e.g., by applying an external gate potential, then its Fermi level shifts away from the neutrality point and the linear screening theory is expected to become appropriate, even at $T = 0$. It is therefore desirable to determine the parameter range where nonlinear effects in screening of an external charge set in, by comparing the results from linear screening models with those from available nonlinear models, such as TF and DFT.

In that context, Katsnelson [25] and Fogler *et al.* [26] have solved the nonlinear TF model, first proposed by DiVicenzo and Mele [24] for intrinsic graphene (i.e., $n = 0$) in the presence of an external point charge. These authors found unusually

long ranged induced density of charge carriers in the plane of graphene [26], and showed that the linear approximation to the TF model for the induced potential is likely to overestimate the contribution of scattering on charged impurities to the resistivity of graphene [25]. However, performance of the TF model has been recently criticized for intrinsic graphene in the presence of sufficiently weak periodic perturbations validating linear screening within the RPA [45]. On the other hand, the above nonlinear TF model, augmented by the exchange (or Dirac) interaction in the local density approximation (LDA), proved to be valuable in estimating the effective potential fluctuations in doped graphene due to randomly distributed multiple charged impurities [28]. A similar problem in the presence of multiple charged impurities was also tackled by a more advanced DFT approach including both the exchange and correlation (XC) interactions in LDA [29]. All the above models were formulated assuming $T = 0$, linear density of states (DOS) of the π electron bands, and no gap between graphene and substrate.

1.2 Thesis Summary

In this work, we take up the simple TF model for a single point charge Ze, a distance z_0 away from graphene [24, 25, 26, 45], where $e(> 0)$ is the charge of a proton. and generalize it to include the effects of a non-zero ground-state charge carrier density n, a non-zero temperature T, and the presence of a substrate at a non-zero distance h from graphene [27]. We assume that the external charge is weak/distant enough to have negligible effects on the structures of graphene's DOS, apart from its shift due to local charging of graphene, but we allow for large displacements of the Fermi level away from the neutrality point by including the nonlinear corrections to the DOS in our model [11]. By varying the magnitude $|n|$,

we are able to examine the effects of doping, whereas any dependence on the sign of n will be a signature of nonlinear effects in screening by graphene. (Note that changing the sign of n with fixed sign of the external charge Z in the TF model is equivalent to changing the sign of Z with fixed sign of n.)

We perform a series of numerical solutions of the nonlinear integral equation resulting from the TF model for the in-plane value of total electrostatic potential for a range of values of n and z_0, for both zero and room temperature, in the cases of both free graphene and an SiO_2 substrate with the gaps $h = 0$ and 1 Å. In a special case of free, intrinsic graphene at $T = 0$, we also solve the nonlinear TF model augmented by the XC energy terms of Polini *et al.* [29] in order to estimate the importance of the exchange and correlation interactions within the TF approach to screening of an external charge. While the results obtained for the radial dependence of the in-plane potential could be directly used to discuss nonlinear effects in graphene's conductivity within the Boltzmann transport theory, we turn our attention in the present work to using our numerical solutions of the TF model to evaluate the nonlinear image potential of an external charge, which provides an integrated measure of graphene's screening ability and is also of interest in recent studies of the electron image states [35, 36]. Finally, we compare our nonlinear results for both the in-plane potential and the image potential with those from the linearized TF (LTF) model and the temperature dependent RPA dielectric-function approach [17, 43, 44].

In chapter 2, we discuss Dirac fermions and the energy spectrum of graphene using a tight-binding approach, and we find the densities of energy and electrons in graphene. The definition of the problem is mentioned in the chapter 3, where we go through the details of the Thomas-Fermi method deriving a nonlinear integral equation for the electrostatic potential, Density Functional Theory (DFT), and

the Random Phase Approximation (RPA). In chapter 4 we discuss the numerical method we use to solve the nonlinear integral equation. We discuss the results in chapter 5 and present our concluding remarks in chapter 6. Note that gaussian electrostatic units are used throughout unless otherwise explicitly indicted.

Chapter 2

Properties of Graphene

2.1 Properties of Graphene

Graphene is a 2-dimensional honeycomb lattice of carbon atoms, as shown in Fig. 2.1(a). The orbital structure of the 6 electrons in a carbon atom is $1s^2\,2s^2\,2p^2$. The $1s$ electrons are close to the nucleus and strongly bound so that they do not contribute to the chemical bond. The hexagonal atomic structure in graphene is constructed from the σ bond joining a carbon atom to each of its three neighbors. When carbon atoms are placed in the graphene lattice, the orbitals of the atoms overlap. Considering symmetry, one realizes that the electron in the $2p_z$ orbital does not overlap with the $2s$, $2p_x$ or $2p_y$ orbitals, because carbon atoms are in a plane (a hybridization of $2s$, $2p_x$, $2p_y$ and $2p_z$ forms the sp^3 orbital which causes the three-dimensional lattice of diamond). The $2s$, $2p_x$ and $2p_y$ orbitals (in-plane orbitals) hybridize to form three sp^2 orbitals. Each atom shares one electron in an sp^2 orbital with a neighboring atom to form a σ bond. Because of symmetry, the angle between those chemical bonds is 120^o. Those strong σ bonds are responsible for the mechanical properties of graphene. The energy spectrum originating from the σ bands in the Bloch bond description contains a large energy gap of $\sim$ 12 eV between the bonding and antibonding states. Since the separations between the two states and the Fermi level are large, σ bonds are usually neglected in the theory of explaining the electrical properties of graphene related to the energies around the Fermi energy. The p_z orbitals, which are perpendicular to the graphene plane, hybridize to form the π bonds and each p_z orbital contributes one electron. Such a system with one electron per lattice site is called a "half-filled" system. The unusual electronic properties of graphene are determined by the π orbitals which form the electronic valence and conduction bands.

The graphene lattice may be seen as a set of two triangular sublattices (denoted

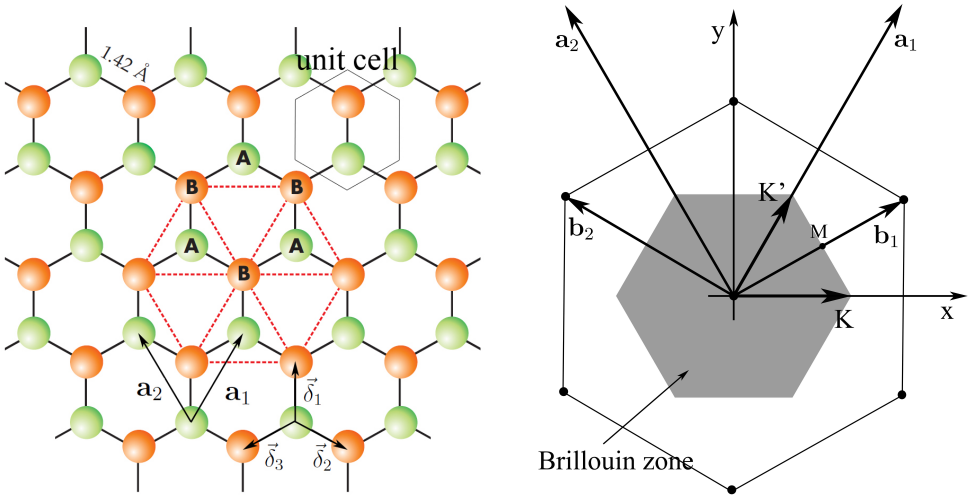

(a) The honeycomb lattice of graphene (b) The reciprocal lattice of graphene

Figure 2.1: (a) The honeycomb lattice of graphene. The unit cell contain two atoms, denoted A and B. $\mathbf{a}_1$ and $\mathbf{a}_2$ are the lattice vectors. (b) The reciprocal-lattice of graphene. The shaded hexagon is the first Brillouin zone. $\mathbf{b}_1$ and $\mathbf{b}_2$ are the reciprocal-lattice vectors. The Dirac points are denoted by $\mathbf{K}$ and $\mathbf{K}'$, placed at the corners of the first Brillouin zone.

by A and B in Fig. 2.1(a)). However, the other possibility is to consider the lattice as a triangular lattice with basis of two atoms per unit cell, one A and one B. The π orbitals contribute to the bonding and antibonding π states in the energy spectrum. The bonding π states (at lower energies) form the valence band and the antibonding π states (at higher energies) form the conduction band. The valence and conduction bands touch each other at the six corners of the Brillouin zone and have a quasi-linear dispersion. Since each carbon atom shares one electron in a π bond, the valence band in graphene is completely filled; therefore graphene is a zero-gap semiconductor or a semi-metal. The (quasi-) linear dispersion is responsible for the unusual electronic properties of graphene. The linear dispersion leads to

massless Dirac fermions, and the six corners of the Brillouin zone are called the Dirac points.

2.2 Tight-Binding Approach

As mentioned before, the structure of graphene may be viewed as a triangular lattice with a basis of two atoms per unit cell. An option of the lattice vectors is

$$\mathbf{a}_1 = \frac{a}{2}(\sqrt{3},\, 3),\ \mathbf{a}_2 = \frac{a}{2}(-\sqrt{3},\, 3), \tag{2.1}$$

where $a \approx 1.42\,\text{Å}$ is the carbon-carbon distance in the lattice. Respectively, the reciprocal-lattice vectors are given by

$$\mathbf{b}_1 = \frac{2\pi}{3a}(\sqrt{3},\, 1),\ \mathbf{b}_2 = \frac{2\pi}{3a}(-\sqrt{3},\, 1). \tag{2.2}$$

Note that the nearest neighbors in real space are

$$\vec{\delta}_1 = \frac{a}{2}(\sqrt{3},\, 1),\ \vec{\delta}_2 = \frac{a}{2}(-\sqrt{3},\, 1),\ \vec{\delta}_3 = -a(0, 1), \tag{2.3}$$

and the position of the Dirac points in the momentum space are given by

$$\mathbf{K} = \left(\frac{4\pi}{3\sqrt{3}a},\, 0\right),\ \mathbf{K}' = \left(\frac{2\pi}{3\sqrt{3}a},\, \frac{2\pi}{3a}\right). \tag{2.4}$$

Painter and Ellis [46] applied an *ab initio* type of variational approach to find the energy spectrum of graphite in a monolayer crystal model (graphene). In their approach they used a linear combination of the atomic orbitals basis of Bloch states. Their result shows a linear dispersion close to the Dirac points (see Fig. 2.2). The group speed at the linear dispersion regime (around Dirac points) is very high, that is $\sim c/300$, where c is the speed of light in vacuum. Charged

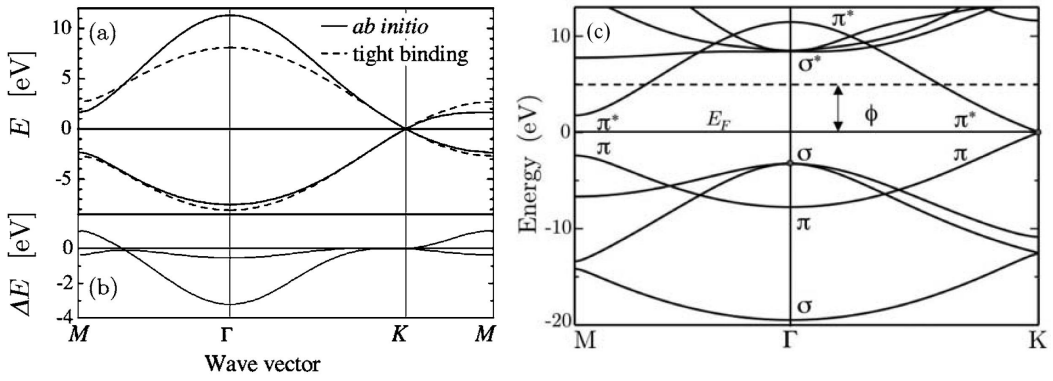

Figure 2.2: (a) Electronic band structure of graphene's π and π^* bands from *ab-initio* calculation [solid lines] and nearest neighbor tight binding [dashed lines]. (b) Difference ΔE between the *ab-initio* and tight binding band structures. Adapted from Reich *et al.*, 2002 [48]. (c) More detail of band structure from *ab-initio* calculations. The bonding σ and the antibonding σ^* bands are separated by a large energy gap ($\sim$ 12 eV). The highest valence band, π, and the lowest conduction band, π^*, show a quasi-linear behavior around the Dirac point **K** (**K**'). Note that the Fermi energy is set to zero. Adapted from Charlier *et al.* [47].

particles should be described by the relativistic Dirac equation rather than the non-relativistic Schrödinger equation, because, as mentioned before, charge carriers in the linear dispersion mimic the behavior of the massless Dirac fermions.

In the tight-binding approach, one considers the solution of the corresponding Schrödinger equation

$$H\Psi(\mathbf{r}) = \varepsilon\Psi(\mathbf{r}), \tag{2.5}$$

where $H = -\frac{\hbar^2}{2m}\nabla^2 + V(\mathbf{r})$. The many-body potential energy $V(\mathbf{r})$ has the symmetry of the lattice

$$V(\mathbf{r} - \mathbf{R}) = V(\mathbf{r}), \tag{2.6}$$

where $\mathbf{R} = n_1\mathbf{a}_1 + n_2\mathbf{a}_2$ is a lattice vector (n_1 and n_2 are integers). The symmetry of the graphene lattice requires the wave function to satisfy the Bloch theorem

$$\Psi(\mathbf{k}, \mathbf{r} - \mathbf{R}) = \exp(-i\mathbf{k} \cdot \mathbf{R})\Psi(\mathbf{k}, \mathbf{r}), \tag{2.7}$$

where $\hbar\mathbf{k}$ is the electron momentum. The overlap between the π (p_z) orbitals and the s, p_x and p_y is strictly zero by symmetry; therefore we use the p_z orbitals as the basis for the wave functions. Each atom is defined by one orbital per atom site $p_z(\mathbf{r} - \mathbf{r}_i - \mathbf{r}_{A/B})$ where $\mathbf{r}_i$ is the site vector and $\mathbf{r}_{A/B}$ is the position of the atom A/B in the site. The wave function may be expanded as:

$$\Psi(\mathbf{k}, \mathbf{r}) = c_A(\mathbf{k})P_z^A(\mathbf{k}, \mathbf{r}) + c_B(\mathbf{k})P_z^B(\mathbf{k}, \mathbf{r}), \tag{2.8}$$

where

$$\begin{aligned} P_z^A(\mathbf{k}, \mathbf{r}) &= \frac{1}{\sqrt{N}} \sum_i \mathrm{e}^{i\mathbf{k}\cdot\mathbf{r}_i} p_z(\mathbf{r} - \mathbf{r}_i - \mathbf{r}_A), \\ P_z^B(\mathbf{k}, \mathbf{r}) &= \frac{1}{\sqrt{N}} \sum_i \mathrm{e}^{i\mathbf{k}\cdot\mathbf{r}_i} p_z(\mathbf{r} - \mathbf{r}_i - \mathbf{r}_B), \end{aligned} \tag{2.9}$$

N is the number of the unit cells and i is the cell position index. We neglect the overlap integrals of two p_z orbitals of two atoms (orthogonal tight-binding scheme); therefore,

$$\begin{aligned} \langle P_z^A | P_z^A \rangle &= \frac{1}{N} \sum_{i,j} \mathrm{e}^{i\mathbf{k}\cdot(\mathbf{r}_i - \mathbf{r}_j)} \int d\mathbf{r}\, p_z^*(\mathbf{r} - \mathbf{r}_j - \mathbf{r}_A)\, p_z(\mathbf{r} - \mathbf{r}_i - \mathbf{r}_A) \\ &\simeq \frac{1}{N} \sum_{i,j} \mathrm{e}^{i\mathbf{k}\cdot(\mathbf{r}_i - \mathbf{r}_j)} \delta_{i\,j} \\ &= 1, \end{aligned} \tag{2.10}$$

and, in the same way, $\langle P_z^A | P_z^B \rangle = 0$. $P_z^{A/B}(\mathbf{k}, \mathbf{r})$ and hence $\Psi(\mathbf{k}, \mathbf{r})$ satisfy the Bloch

condition, Eq. (2.7):

$$\begin{aligned} P_z^{A/B}(\mathbf{k}, \mathbf{r}-\mathbf{R}) &= \frac{1}{\sqrt{N}} \sum_i \mathrm{e}^{i\mathbf{k}\cdot\mathbf{r}_i} p_z(\mathbf{r}-\mathbf{R}-\mathbf{r}_i-\mathbf{r}_{A/B}) \\ &= \frac{1}{\sqrt{N}} \sum_j \mathrm{e}^{i\mathbf{k}\cdot(\mathbf{r}_j-\mathbf{R})} p_z(\mathbf{r}-\mathbf{r}_j-\mathbf{r}_{A/B}) \\ &= \mathrm{e}^{-i\mathbf{k}\cdot\mathbf{R}}\, P_z^{A/B}(\mathbf{k}, \mathbf{r}), \end{aligned} \tag{2.11}$$

where we have used the periodicity of the lattice and renamed $\mathbf{r}_j = \mathbf{r}_i + \mathbf{R}$. Using this notation, the Schrödinger equation becomes

$$\begin{pmatrix} H_{AA}(\mathbf{k}) & H_{AB}(\mathbf{k}) \\ H_{BA}(\mathbf{k}) & H_{BB}(\mathbf{k}) \end{pmatrix} \begin{pmatrix} c_A(\mathbf{k}) \\ c_B(\mathbf{k}) \end{pmatrix} = \varepsilon \begin{pmatrix} c_A(\mathbf{k}) \\ c_B(\mathbf{k}) \end{pmatrix} \tag{2.12}$$

where

$$H_{AA}(\mathbf{k}) = \langle P_z^A | H | P_z^A \rangle = \frac{1}{N} \sum_{i,j} \mathrm{e}^{i\mathbf{k}\cdot(\mathbf{r}_j-\mathbf{r}_i)} \langle p_z^{A,i} | H | p_z^{A,j} \rangle, \tag{2.13}$$

$$H_{BB}(\mathbf{k}) = \langle P_z^B | H | P_z^B \rangle = \frac{1}{N} \sum_{i,j} \mathrm{e}^{i\mathbf{k}\cdot(\mathbf{r}_j-\mathbf{r}_i)} \langle p_z^{B,i} | H | p_z^{B,j} \rangle, \tag{2.14}$$

$$H_{AB}(\mathbf{k}) = \langle P_z^A | H | P_z^B \rangle = \frac{1}{N} \sum_{i,j} \mathrm{e}^{i\mathbf{k}\cdot(\mathbf{r}_j-\mathbf{r}_i)} \langle p_z^{A,i} | H | p_z^{B,j} \rangle, \tag{2.15}$$

where $p_z^{A/B,i} = p_z(\mathbf{r}-\mathbf{r}_i-\mathbf{r}_{A/B})$. Hence, solving the Schrödinger equation reduces to diagonalization of a 2×2 matrix or

$$\det \begin{pmatrix} H_{AA}(\mathbf{k})-\varepsilon & H_{AB}(\mathbf{k}) \\ H_{BA}(\mathbf{k}) & H_{BB}(\mathbf{k})-\varepsilon \end{pmatrix} = 0. \tag{2.16}$$

To go further, we redefine the energy reference of the system such that $\langle p_z^{A,i} | H | p_z^{A,i} \rangle = \langle p_z^{B,j} | H | p_z^{B,j} \rangle = 0$. As a good approximation we restrict the interaction to first and next-nearest neighbors only, namely

$$\langle p_z^{A,i} | H | p_z^{B,j} \rangle = \begin{cases} -t & \text{for nearest neighbor atoms} \\ 0 & \text{otherwise} \end{cases} \tag{2.17}$$

and

$$\langle p_z^{A,i}|H|p_z^{A,j}\rangle = \langle p_z^{B,i}|H|p_z^{B,j}\rangle = \begin{cases} -t' & \text{for second nearest neighbor atoms} \\ 0 & \text{otherwise} \end{cases} \tag{2.18}$$

where $t(\approx 3\,\mathrm{eV})$ [47] is the nearest-neighbor hopping energy (transfer integral) and t' is the next nearest neighbor hopping energy (hopping in the same sublattice). The value of t' is not well known but, Reich *at al.* [48], by *ab initio* calculation showed that $0.02\,t \lesssim t' \lesssim 0.2\,t$. Deacon *et al.* [49] by a tight-binding fitting to the cyclotron resonance experiments found $t' \approx 0.1$ eV. Note that the hamiltonian of the system satisfies the spin constancy in hopping. Therefore, up to the second nearest neighbor interactions, one gets

$$\begin{aligned} H_{AB}(\mathbf{k}) &= \frac{1}{N}\sum_i \left[\langle p_z^{A,0}|H|p_z^{B,0}\rangle + \mathrm{e}^{-i\mathbf{k}\cdot\mathbf{a}_1}\langle p_z^{A,0}|H|p_z^{B,-\mathbf{a}_1}\rangle + \mathrm{e}^{-i\mathbf{k}\cdot\mathbf{a}_2}\langle p_z^{A,0}|H|p_z^{B,-\mathbf{a}_2}\rangle\right] \\ &= -t\left(1+\mathrm{e}^{-i\mathbf{k}\cdot\mathbf{a}_1}+\mathrm{e}^{-i\mathbf{k}\cdot\mathbf{a}_2}\right) \\ &= -t\,\alpha(\mathbf{k}), \end{aligned} \tag{2.19}$$

and

$$\begin{aligned} H_{AA}(\mathbf{k}) &= \frac{1}{N}\sum_i [\mathrm{e}^{-i\mathbf{k}\cdot\mathbf{a}_1}\langle p_z^{A,0}|H|p_z^{A,-\mathbf{a}_1}\rangle + \mathrm{e}^{i\mathbf{k}\cdot\mathbf{a}_1}\langle p_z^{A,0}|H|p_z^{A,\mathbf{a}_1}\rangle \\ &\quad + \mathrm{e}^{-i\mathbf{k}\cdot\mathbf{a}_2}\langle p_z^{A,0}|H|p_z^{A,-\mathbf{a}_2}\rangle + \mathrm{e}^{i\mathbf{k}\cdot\mathbf{a}_2}\langle p_z^{A,0}|H|p_z^{A,\mathbf{a}_2}\rangle \\ &\quad + \mathrm{e}^{i\mathbf{k}\cdot(\mathbf{a}_2-\mathbf{a}_1)}\langle p_z^{A,0}|H|p_z^{A,\mathbf{a}_2-\mathbf{a}_1}\rangle + \mathrm{e}^{-i\mathbf{k}\cdot(\mathbf{a}_2-\mathbf{a}_1)}\langle p_z^{A,0}|H|p_z^{A,\mathbf{a}_1-\mathbf{a}_2}\rangle] \\ &= -t'\,[2\cos(\mathbf{k}\cdot\mathbf{a}_1)+2\cos(\mathbf{k}\cdot\mathbf{a}_2)+2\cos[\mathbf{k}\cdot(\mathbf{a}_2-\mathbf{a}_1)]] \\ &= -t'\,f(\mathbf{k}). \end{aligned} \tag{2.20}$$

Similarly,

$$H_{BB} = -t'\,f(\mathbf{k}). \tag{2.21}$$

The hamiltonian determinant, Eq. (2.16), reduces to

$$\det \begin{pmatrix} -t'\, f(\mathbf{k}) - \varepsilon & -t\, \alpha(\mathbf{k}) \\ -t\, \alpha^{\star}(\mathbf{k}) & -t'\, f(\mathbf{k}) - \varepsilon \end{pmatrix} \tag{2.22}$$

The assumptions mentioned above may be clarified more if we use the creation and annihilation operators:

$$\begin{aligned} H &= -t \sum_{\langle i,j\rangle,\,\sigma} \left(a^{\dagger}_{\sigma,\,i} b_{\sigma,\,j} + \text{h.c.} \right) \\ &\quad -t' \sum_{\langle\langle i,j\rangle\rangle,\,\sigma} \left(a^{\dagger}_{\sigma,\,i} a_{\sigma,\,j} + b^{\dagger}_{\sigma,\,i} b_{\sigma,\,j} + \text{h.c.} \right), \end{aligned} \tag{2.23}$$

here, $\sigma(=\uparrow, \downarrow)$ denotes the electron's spin and $a_{i,\sigma}$ ($a^{\dagger}_{i,\sigma}$) annihilates (creates) an electron with spin σ on site i on sublattice A (an analogous definition is used for sublattice B). $\langle i,j\rangle$ and $\langle\langle i,j\rangle\rangle$ denotes that the summation applies only on the first and second nearest neighbors atoms.

By diagonalizing the matrix of hamiltonian, we find the energy eigenvalues:

$$\begin{aligned} \varepsilon^{\pm}(\mathbf{k}) &= \pm t\, |\alpha(\mathbf{k})| - t'\, f(\mathbf{k}) \\ &= \pm t \sqrt{3 + 2\cos(\mathbf{k}\cdot\mathbf{a}_1) + 2\cos(\mathbf{k}\cdot\mathbf{a}_2) + 2\cos[\mathbf{k}\cdot(\mathbf{a}_2 - \mathbf{a}_1)]} - t'\, f(\mathbf{k}) \\ &= \pm t \sqrt{3 + f(\mathbf{k})} - t'\, f(\mathbf{k}) \cdot \end{aligned} \tag{2.24}$$

Substituting the lattice vectors we find

$$\begin{aligned} f(\mathbf{k}) &= 2\cos\left(\frac{3}{2}k_y a + \frac{\sqrt{3}}{2}k_x a\right) + 2\cos\left(\frac{3}{2}k_y a - \frac{\sqrt{3}}{2}k_x a\right) + 2\cos\left(\sqrt{3}k_x a\right) \\ &= 4\cos\left(\frac{\sqrt{3}}{2}k_x a\right)\cos\left(\frac{3}{2}k_y a\right) + 2\cos\left(\sqrt{3}k_x a\right), \end{aligned} \tag{2.25}$$

where the plus sign gives the upper band $\pi^{\star}$ and the minus sign gives the lower band π. If $t' = 0$, at Dirac points, $\mathbf{K}$ and $\mathbf{K}'$ (Eq. (2.4)), the energy is zero and

the spectrum around them is symmetric. Since we are interested in the spectrum around Dirac points, it is useful to redefine the vectors of momentum space as $\mathbf{k} = \mathbf{K} + \mathbf{q}$, or $\mathbf{k} = \mathbf{K}' + \mathbf{q}$ where $|\mathbf{q}| \ll |\mathbf{K}|$. Then for case $\mathbf{k} = \mathbf{K} + \mathbf{q}$

$$\begin{aligned} f_{\mathbf{K}}(\mathbf{q}) &\equiv f(\mathbf{K}+\mathbf{q}) = 4\cos\left(\frac{2\pi}{3} + \frac{\sqrt{3}}{2}q_x a\right)\cos\left(\frac{3}{2}q_y a\right) + 2\cos\left(\frac{4\pi}{3} + \sqrt{3}q_x a\right) \\ &= \left[-2\sqrt{3}\sin\left(\frac{\sqrt{3}}{2}q_x a\right) - 2\cos\left(\frac{\sqrt{3}}{2}q_x a\right)\right]\cos\left(\frac{3}{2}q_y a\right) \\ &\quad -\cos(\sqrt{3}q_x a) + \sqrt{3}\sin(\sqrt{3}q_x a), \end{aligned} \tag{2.26}$$

and for case $\mathbf{k} = \mathbf{K}' + \mathbf{q}$

$$\begin{aligned} f_{\mathbf{K}'}(\mathbf{q}) &\equiv f(\mathbf{K}' + \mathbf{q}) = 4\cos\left(\frac{\pi}{3} + \frac{\sqrt{3}}{2}q_x a\right)\cos\left(\pi + \frac{3}{2}q_y a\right) \\ &\quad +2\cos\left(\frac{2\pi}{3} + \sqrt{3}q_x a\right) \\ &= \left[2\sqrt{3}\sin\left(\frac{\sqrt{3}}{2}q_x a\right) - 2\cos\left(\frac{\sqrt{3}}{2}q_x a\right)\right]\cos\left(\frac{3}{2}q_y a\right) \\ &\quad -\cos(\sqrt{3}q_x a) - \sqrt{3}\sin(\sqrt{3}q_x a). \end{aligned} \tag{2.27}$$

We note that

$$\begin{aligned} f_{\mathbf{K}/\mathbf{K}'}(q_x,\, q_y) &= f_{\mathbf{K}/\mathbf{K}'}(q_x,\, -q_y), \\ f_{\mathbf{K}}(q_x,\, q_y) &= f_{\mathbf{K}'}(-q_x,\, \pm q_y). \end{aligned} \tag{2.28}$$

Expanding $f_{\mathbf{K}}(\mathbf{q})$ up to $O(|\mathbf{q}|^3)$, we find

$$\begin{aligned} f_{\mathbf{K}}(\mathbf{q}) &\simeq -3 + \frac{9a^2}{4}\left(q_x^2 + q_y^2\right) - \frac{9a^3}{8}q_x\left(q_x^2 - 3q_y^2\right) \\ &\quad -\frac{27a^4}{64}\left(q_x^4 + q_y^4\right) - \frac{27a^4}{32}q_x^2 q_y^2, \end{aligned} \tag{2.29}$$

or

$$\begin{aligned} f_{\mathbf{K}}(\mathbf{q}) &\simeq -3 + \frac{9a^2}{4}|\mathbf{q}|^2 - \frac{9a^3}{2}q_x^3 + \frac{27a^3}{8}q_x|\mathbf{q}|^2 - \frac{27a^4}{64}|\mathbf{q}|^4 \\ &\simeq -3 + \frac{9a^2}{4}|\mathbf{q}|^2\left(1 - 2q_x^3/|\mathbf{q}|^2 + \frac{3}{2}q_x - \frac{3}{16}|\mathbf{q}|^2\right). \end{aligned} \tag{2.30}$$

Substituting $f_{\mathbf{K}}(\mathbf{q})$ into Eq. (2.24), up to the second order in $|\mathbf{q}|/|\mathbf{K}|$, we find

$$\begin{aligned}\varepsilon_{\pm}^{\mathbf{K}}(\mathbf{q}) &\simeq \pm\frac{3ta}{2}|\mathbf{q}|\left(1-2q_x^3/|\mathbf{q}|^2+\frac{3}{2}q_x-\frac{3}{16}|\mathbf{q}|^2\right)^{\frac{1}{2}}+3t'-\frac{9t'a^2}{4}|\mathbf{q}|^2 \\ &\simeq \pm\frac{3ta}{2}|\mathbf{q}|\pm\frac{3ta^2}{8}\left(-4q_x^3/|\mathbf{q}|^3+3q_x/|\mathbf{q}|\right)+3t'-\frac{9t'a^2}{4}|\mathbf{q}|^2. \qquad (2.31)\end{aligned}$$

By defining $\theta_{\mathrm{q}} = \arcsin(q_x/|\mathbf{q}|)$, the spectrum equation may be rewritten in the form:

$$\varepsilon_{\pm}^{\mathbf{K}}(\mathbf{q}) \simeq 3t' \pm \hbar v_F|\mathbf{q}| + \left(\pm\frac{3ta^2}{8}\sin(3\theta_{\mathrm{q}})-\frac{9t'a^2}{4}\right)|\mathbf{q}|^2, \qquad (2.32)$$

where $v_F = 3ta/2\hbar$ is the Fermi speed. For $\mathbf{K}'$ we have

$$\varepsilon_{\pm}^{\mathbf{K}'}(\mathbf{q}) \simeq 3t' \pm \hbar v_F|\mathbf{q}| + \left(\mp\frac{3ta^2}{8}\sin(3\theta_{\mathrm{q}})-\frac{9t'a^2}{4}\right)|\mathbf{q}|^2. \qquad (2.33)$$

The band structure is shown in Fig. 2.3 for two different sets of values of t and t'. Note that if $t' = 0$, then the energy spectrum in the first order is

$$\varepsilon_{\pm}(\mathbf{q}) \approx \pm\hbar v_F|\mathbf{q}| + O[(|\mathbf{q}|/|\mathbf{K}|)^2]. \qquad (2.34)$$

It is clear that the spectrum is symmetric around Dirac points. The electron-hole symmetry is broken for non-zero values of t'. The linear relation between energy and momentum indicates that, close to the Dirac points, the speed of an electron (hole) does not depend on the energy or momentum,e.g., the speed is constant and equal to v_F as a massless particle. In other words, the electron (hole) energy may be seen as the limit of the Einstein equation $E = \sqrt{m^2c^4 + p^2c^2}$, with $m = 0$ and $c = v_F$, similarly to the case of light. Eq. (2.33) shows the presence of t' shifts the position of the Dirac points in energy.

To find the form of the wave function, we consider the region of low energies where the wave vector $\mathbf{k}$ lies around the Dirac points. The wave function has the form of Eq. (2.8). We assume $t' = 0$, when the non-zero elements of the hamiltonian

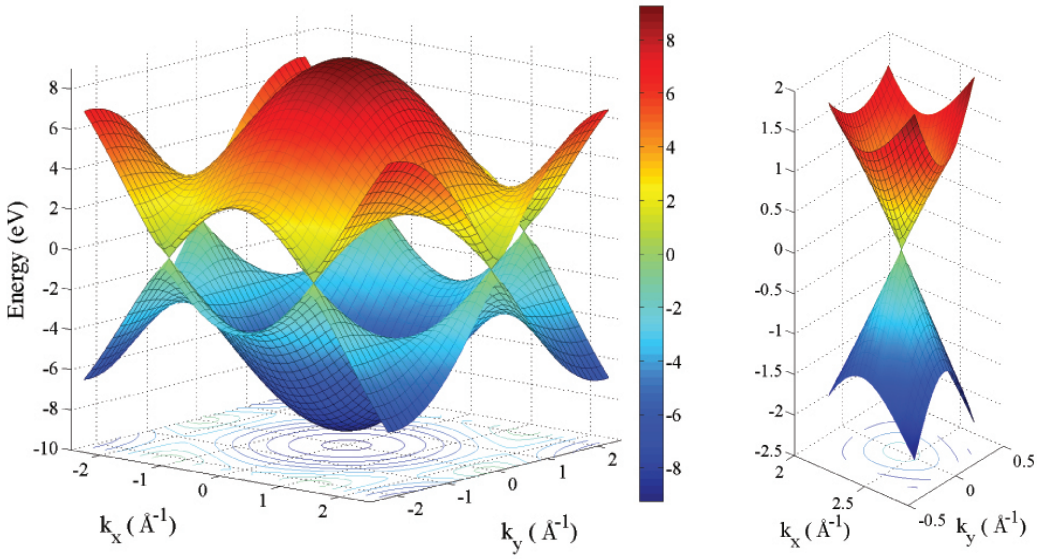

(a) Energy spectrum for $t = 3.08$ eV and $t' = 0$

(b) Zoom in

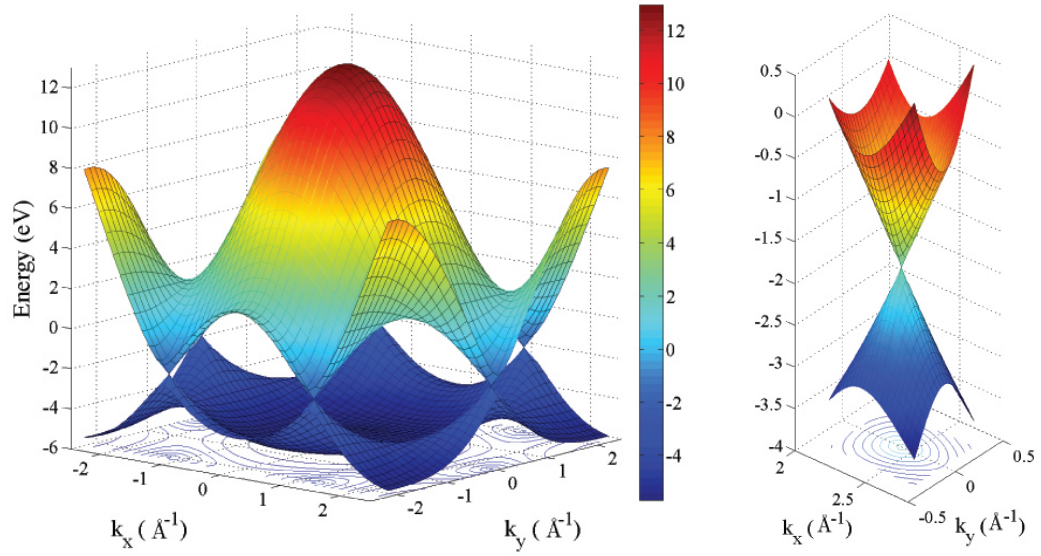

(c) Energy spectrum for $t = 3.08$ eV and $t' = -0.2t$

(d) Zoom in

Figure 2.3: Energy spectrum of graphene, Eq. (2.24), (a) for $t = 3.08$ eV and $t' = 0$; (b) zoom in of the energy spectrum close to the Dirac point **K**; (c) for $t = 3.08$ eV and $t' = -0.2t$; (d) zoom in of the energy spectrum close to the Dirac point **K**.

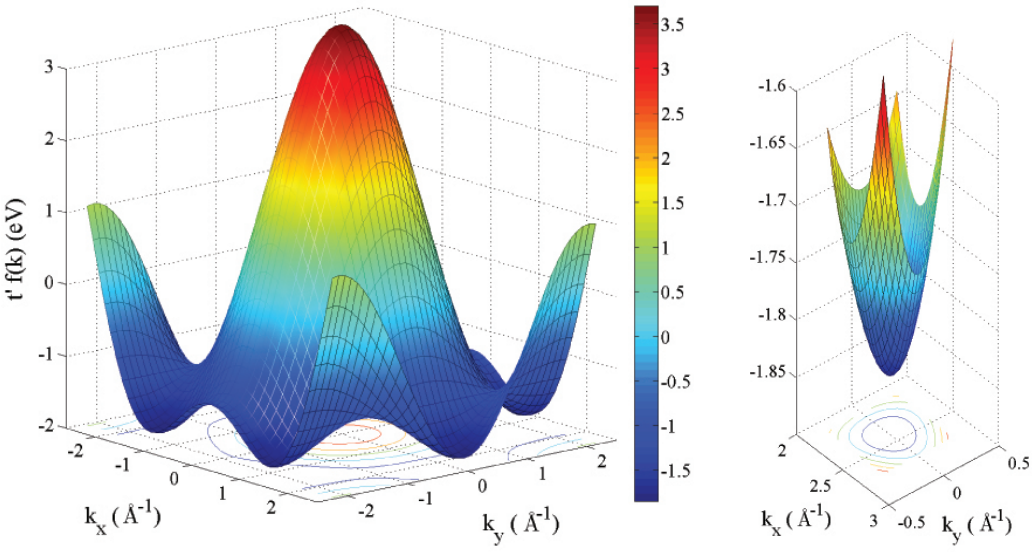

(a) The contribution of second nearest neighbor hopping (b) Zoom in

Figure 2.4: The contribution of second nearest neighbor hopping to the energy spectrum of graphene, for $t = 3.08$ eV and $t' = -0.2t$; (b) zoom in of the energy spectrum close to Dirac point **K**.

determinant, Eq. (2.16), are $H_{AB}(\mathbf{k}) = -t\alpha(\mathbf{k})$ and $H_{BA}(\mathbf{k}) = -t\alpha^{\star}(\mathbf{k})$. One can expand the $\alpha(\mathbf{k})$ around $\mathbf{K}$ ($|\mathbf{q}| \ll |\mathbf{K}|$) as

$$\begin{aligned} \alpha_{\mathbf{K}}(\mathbf{k}) &\equiv \alpha(\mathbf{K}+\mathbf{q}) = 1 + \mathrm{e}^{-i(\mathbf{K}+\mathbf{q})\cdot\mathbf{a}_1} + \mathrm{e}^{-i(\mathbf{K}+\mathbf{q})\cdot\mathbf{a}_2} \\ &\simeq 1 + \mathrm{e}^{-i\mathbf{K}\cdot\mathbf{a}_1}(1 - i\mathbf{q}\cdot\mathbf{a}_1) + \mathrm{e}^{-i\mathbf{K}\cdot\mathbf{a}_2}(1 - i\mathbf{q}\cdot\mathbf{a}_2) \\ &\simeq -\frac{3a}{2}q_x + i\frac{3a}{2}q_y, \end{aligned} \tag{2.35}$$

or

$$H_{AB}^{\mathbf{K}} \approx \frac{3ta}{2}q_x - i\frac{3ta}{2}q_y = \hbar v_F q_x - i\hbar v_F q_y = -i\hbar v_F |\mathbf{q}| \mathrm{e}^{i\theta_q}. \tag{2.36}$$

In the same way we find

$$H_{BA}^{\mathbf{K}} \approx \hbar v_F q_x + i\hbar v_F q_y = i\hbar v_F |\mathbf{q}| \mathrm{e}^{-i\theta_q}. \tag{2.37}$$

Therefore the coefficients $c_A(\mathbf{k})$ and $c_B(\mathbf{k})$ in the wave function Eq. (2.8) are given by the solution of

$$\begin{pmatrix} 0 & -i\hbar v_F|\mathbf{q}|\mathrm{e}^{i\theta_q} \\ i\hbar v_F|\mathbf{q}|\mathrm{e}^{-i\theta_q} & 0 \end{pmatrix} \begin{pmatrix} c_A \\ c_B \end{pmatrix} = \pm\hbar v_F|\mathbf{q}| \begin{pmatrix} c_A \\ c_B \end{pmatrix}. \tag{2.38}$$

that is,

$$\begin{aligned} c_A &= \frac{1}{\sqrt{2}}\,\mathrm{e}^{i\theta_q/2}, \\ c_B &= \pm\frac{i}{\sqrt{2}}\,\mathrm{e}^{-i\theta_q/2}, \end{aligned} \tag{2.39}$$

and the wave function is

$$\Psi_{\pm,\mathbf{K}}(\mathbf{k},\mathbf{r}) = \frac{1}{\sqrt{2}} \begin{pmatrix} \mathrm{e}^{i\theta_q/2} & \pm i\mathrm{e}^{-i\theta_q/2} \end{pmatrix} \begin{pmatrix} P_z^A(\mathbf{k},\mathbf{r}) \\ P_z^B(\mathbf{k},\mathbf{r}) \end{pmatrix}, \tag{2.40}$$

where $P_z^A(\mathbf{k},\mathbf{r})$ and $P_z^B(\mathbf{k},\mathbf{r})$ are given by Eq. (2.9). In the same way, if we expand $\alpha(\mathbf{k})$ around $\mathbf{K}'$, we find

$$\alpha_{\mathbf{K}'}(\mathbf{k}) \equiv \alpha(\mathbf{K}'+\mathbf{q}) \simeq \frac{3a}{2}q_x + i\frac{3a}{2}q_y. \tag{2.41}$$

Then

$$H_{AB}^{\mathbf{K}'} \approx -\hbar v_F q_x - i\hbar v_F q_y = -i\hbar v_F|\mathbf{q}|\mathrm{e}^{-i\theta_q}, \tag{2.42}$$

and

$$H_{BA}^{\mathbf{K}'} \approx -\hbar v_F q_x + i\hbar v_F q_y = i\hbar v_F|\mathbf{q}|\mathrm{e}^{i\theta_q}. \tag{2.43}$$

Solving the corresponding matrix equation, we find

$$\begin{aligned} c_A &= \frac{1}{\sqrt{2}}\,\mathrm{e}^{-i\theta_q/2}, \\ c_B &= \pm\frac{i}{\sqrt{2}}\,\mathrm{e}^{i\theta_q/2}, \end{aligned} \tag{2.44}$$

and the wave function is

$$\Psi_{\pm,\mathbf{K}'}(\mathbf{k},\mathbf{r}) = \frac{1}{\sqrt{2}} \begin{pmatrix} \mathrm{e}^{-i\theta_q/2} & \pm i\mathrm{e}^{i\theta_q/2} \end{pmatrix} \begin{pmatrix} P_z^A(\mathbf{k},\mathbf{r}) \\ P_z^B(\mathbf{k},\mathbf{r}) \end{pmatrix}. \tag{2.45}$$

Note that Eq. (2.38) may be rewritten as

$$\hbar v_F \sigma \cdot \mathbf{q} \begin{pmatrix} c_A \\ c_B \end{pmatrix} = \pm \hbar v_F \begin{pmatrix} c_A \\ c_B \end{pmatrix}, \tag{2.46}$$

where σ is a matrix made of Pauli matrices

$$\begin{aligned} \sigma_x &= \begin{pmatrix} 0 & 1 \\ 1 & 0 \end{pmatrix} \\ \sigma_y &= \begin{pmatrix} 0 & -i \\ i & 0 \end{pmatrix} \\ \sigma &= (\sigma_x\, \sigma_y), \end{aligned} \tag{2.47}$$

and, for the states around $\mathbf{K}'$, this equation becomes

$$\hbar v_F \sigma^\star \cdot \mathbf{q} \begin{pmatrix} c_A \\ c_B \end{pmatrix} = \pm \hbar v_F \begin{pmatrix} c_A \\ c_B \end{pmatrix}, \tag{2.48}$$

where $\sigma' = (\sigma_x - \sigma_y)$. Note that the minus sign is absorbed in the sign of the energy's eigenvalue. This is the starting point of finding an effective mass approximation equation for graphene.

2.3 Dirac Fermions

In this section we derive an effective mass approximation equation for graphene. We use the second quantization notation. The hamiltonian of the system has the

form of Eq. (2.23). Here, we assume $t' = 0$. The definition of the bases for the wave function, Eq. (2.9), is equivalent to defining the Fourier transform of the creation and annihilation operators

$$\begin{aligned} a_i &= \frac{1}{\sqrt{N}} \sum_{\mathbf{k}} \mathrm{e}^{-i\mathbf{k}\cdot\mathbf{r}_i} a(\mathbf{k}) \\ b_i &= \frac{1}{\sqrt{N}} \sum_{\mathbf{k}} \mathrm{e}^{-i\mathbf{k}\cdot\mathbf{r}_i} b(\mathbf{k}), \end{aligned} \tag{2.49}$$

where, for simplicity in notation, we have dropped the spin index, but we keep in mind that there is a summation on spin which leads to the degeneracy of two spin states. Inserting the Fourier transforms in the hamiltonian Eq. (2.23), we find

$$\begin{aligned} H &= -t \sum_{\langle i,j \rangle} \left(\frac{1}{N} \sum_{\mathbf{k}} \mathrm{e}^{i\mathbf{k}\cdot\mathbf{r}_i} a^\dagger(\mathbf{k}) \sum_{\mathbf{k}'} \mathrm{e}^{-i\mathbf{k}'\cdot\mathbf{r}_j} b(\mathbf{k}) + H.C. \right) \\ &= -t \sum_{\mathbf{k},\mathbf{k}'} \left(\frac{1}{N} \sum_{\langle i,j \rangle} \mathrm{e}^{i\mathbf{k}\cdot\mathbf{r}_i - i\mathbf{k}'\cdot\mathbf{r}_j} a^\dagger(\mathbf{k}) b(\mathbf{k}') + H.C. \right) \\ &= -t \sum_{\mathbf{k}} \left(\alpha(\mathbf{k}) a^\dagger(\mathbf{k}) b(\mathbf{k}) + H.C. \right) \end{aligned} \tag{2.50}$$

Thus, the hamiltonian is

$$H = \sum_{\mathbf{k}} \begin{pmatrix} a^\dagger(\mathbf{k}) & b^\dagger(\mathbf{k}) \end{pmatrix} \begin{pmatrix} 0 & -t\alpha(\mathbf{k}) \\ -t\alpha^\star(\mathbf{k}) & 0 \end{pmatrix} \begin{pmatrix} a(\mathbf{k}) \\ b(\mathbf{k}) \end{pmatrix} \tag{2.51}$$

We are interested in physical properties of the system in the region of low energies where the wave vector $\mathbf{k}$ lies around the Dirac points. The fact that, at low energies, mostly the states around Dirac points are occupied, leads to another way of expanding the wave function, and an effective-mass approximation for the coefficient of expansion. As we found before, up to first order in $|\mathbf{q}|$, the hamiltonian Eq. (2.51), in the region of low energy may be seen as a summation of two states, state with momentum vector $\mathbf{k}$ around $\mathbf{K}$ and the other state with momentum

vector $\mathbf{k}$ around $\mathbf{K}'$:

$$\begin{aligned} H &= \sum_{\mathbf{k}=\mathbf{K}+\mathbf{q}} \left(a^\dagger(\mathbf{k})\ b^\dagger(\mathbf{k})\right) \begin{pmatrix} 0 & \hbar v_F q_x - i\hbar v_F q_y \\ \hbar v_F q_x + i\hbar v_F q_y & 0 \end{pmatrix} \begin{pmatrix} a(\mathbf{k}) \\ b(\mathbf{k}) \end{pmatrix} \\ &+ \sum_{\mathbf{k}=\mathbf{K}'+\mathbf{q}} \left(a^\dagger(\mathbf{k})\ b^\dagger(\mathbf{k})\right) \begin{pmatrix} 0 & -\hbar v_F q_x - i\hbar v_F q_y \\ -\hbar v_F q_x + i\hbar v_F q_y & 0 \end{pmatrix} \begin{pmatrix} a(\mathbf{k}) \\ b(\mathbf{k}) \end{pmatrix}, \end{aligned} \tag{2.52}$$

or

$$\begin{aligned} H &= \hbar v_F \sum_{\mathbf{k}=\mathbf{K}+\mathbf{q}} \begin{pmatrix} a^\dagger(\mathbf{k}) & b^\dagger(\mathbf{k}) \end{pmatrix} \sigma \cdot \mathbf{q} \begin{pmatrix} a(\mathbf{k}) \\ b(\mathbf{k}) \end{pmatrix} \\ &+ \hbar v_F \sum_{\mathbf{k}=\mathbf{K}+\mathbf{q}} \begin{pmatrix} a^\dagger(\mathbf{k}) & b^\dagger(\mathbf{k}) \end{pmatrix} \sigma^\star \cdot \mathbf{q} \begin{pmatrix} a(\mathbf{k}) \\ b(\mathbf{k}) \end{pmatrix}, \end{aligned} \tag{2.53}$$

where, again we absorb the sign of the second summation into its eigenvalue. We define the new set of operators

$$\begin{aligned} a_i &= \mathrm{e}^{-i\mathbf{K}\cdot\mathbf{r}_i} a_{1\,i} + \mathrm{e}^{-i\mathbf{K}'\cdot\mathbf{r}_i} a_{2\,j} \\ b_i &= \mathrm{e}^{-i\mathbf{K}\cdot\mathbf{r}_i} b_{1\,i} + \mathrm{e}^{-i\mathbf{K}'\cdot\mathbf{r}_i} b_{2\,j} \end{aligned} \tag{2.54}$$

In fact, we assume that each operator may be expanded as a summation of two new operators near the Dirac points, and then

$$\begin{aligned} a(\mathbf{k}) &= \frac{1}{\sqrt{N}} \sum_i \left(\mathrm{e}^{i(\mathbf{k}-\mathbf{K})\cdot\mathbf{r}_i} a_{1\,i} + \mathrm{e}^{i(\mathbf{k}-\mathbf{K}')\cdot\mathbf{r}_i} a_{2\,i}\right) \\ b(\mathbf{k}) &= \frac{1}{\sqrt{N}} \sum_i \left(\mathrm{e}^{i(\mathbf{k}-\mathbf{K})\cdot\mathbf{r}_i} b_{1\,i} + \mathrm{e}^{i(\mathbf{k}-\mathbf{K}')\cdot\mathbf{r}_i} b_{2\,i}\right) \end{aligned} \tag{2.55}$$

Inserting operators Eq. (2.55) in the Eq. (2.53), we find

$$\begin{aligned} H &= \hbar v_F \sum_{\mathbf{q}} \frac{1}{N} \sum_{i,\,j} \left[\begin{pmatrix} \mathrm{e}^{-i\mathbf{q}\cdot\mathbf{r}_j} a_{1\,j}^\dagger & \mathrm{e}^{-i\mathbf{q}\cdot\mathbf{r}_j} b_{1\,j}^\dagger \end{pmatrix} \sigma \cdot \mathbf{q} \begin{pmatrix} \mathrm{e}^{i\mathbf{q}\cdot\mathbf{r}_i} a_{1\,i} \\ \mathrm{e}^{i\mathbf{q}\cdot\mathbf{r}_i} b_{1\,i} \end{pmatrix} \right] \\ &+ \hbar v_F \sum_{\mathbf{q}'} \frac{1}{N} \sum_{i,\,j} \left[\begin{pmatrix} \mathrm{e}^{-i\mathbf{q}'\cdot\mathbf{r}_j} a_{2\,j}^\dagger & \mathrm{e}^{-i\mathbf{q}'\cdot\mathbf{r}_j} b_{2\,j}^\dagger \end{pmatrix} \sigma^\star \cdot \mathbf{q}' \begin{pmatrix} \mathrm{e}^{i\mathbf{q}'\cdot\mathbf{r}_i} a_{2\,i} \\ \mathrm{e}^{i\mathbf{q}'\cdot\mathbf{r}_i} b_{2\,i} \end{pmatrix} \right], \end{aligned} \tag{2.56}$$

where $\mathbf{q} = \mathbf{k} - \mathbf{K}$ and $\mathbf{q}' = \mathbf{k} - \mathbf{K}'$. Note that

$$\sigma \cdot \mathbf{q} = -i\sigma \cdot \nabla \tag{2.57}$$

where ∇ applies on $\mathbf{r}_i$. Thus the hamiltonian reduces to

$$\begin{aligned} H &= -i\hbar v_F \sum_i \left[\begin{pmatrix} \sum_{\mathbf{q}} \mathrm{e}^{-i\mathbf{q}\cdot\mathbf{r}_i} a_{1\,i}^\dagger & \sum_{\mathbf{q}} \mathrm{e}^{-i\mathbf{q}\cdot\mathbf{r}_i} b_{1\,j}^\dagger \end{pmatrix} \sigma \cdot \nabla \begin{pmatrix} \sum_{\mathbf{q}} \mathrm{e}^{i\mathbf{q}\cdot\mathbf{r}_i} a_{1\,i} \\ \sum_{\mathbf{q}} \mathrm{e}^{i\mathbf{q}\cdot\mathbf{r}_i} b_{1\,j} \end{pmatrix} \right. \\ &\left. + \begin{pmatrix} \sum_{\mathbf{q}'} \mathrm{e}^{-i\mathbf{q}'\cdot\mathbf{r}_i} a_{2\,i}^\dagger & \sum_{\mathbf{q}'} \mathrm{e}^{-i\mathbf{q}'\cdot\mathbf{r}_i} b_{2\,j}^\dagger \end{pmatrix} \sigma^\star \cdot \nabla \begin{pmatrix} \sum_{\mathbf{q}'} \mathrm{e}^{i\mathbf{q}'\cdot\mathbf{r}_i} a_{2\,i} \\ \sum_{\mathbf{q}'} \mathrm{e}^{i\mathbf{q}'\cdot\mathbf{r}_i} b_{2\,j} \end{pmatrix} \right]. \end{aligned} \tag{2.58}$$

One can see that Eq. (2.58), in first quantized language, indicates that the total wave function may be viewed as a superposition of two basis wave functions, expanded around the Dirac points, so that the 2-component coefficient of expansion, $\psi(\mathbf{r})$, close to Dirac points, obeys the 2-dimensional Dirac equation

$$-i\hbar v_F \sigma \cdot \nabla \psi(\mathbf{r}) = E\psi(\mathbf{r}), \tag{2.59}$$

and

$$-i\hbar v_F \sigma^\star \cdot \nabla \psi(\mathbf{r}) = E\psi(\mathbf{r}). \tag{2.60}$$

In momentum space, as we found before, the wave function, around $\mathbf{K}$ has the form

$$\psi_{\pm,\mathbf{K}}(\mathbf{k}) = \frac{1}{\sqrt{2}} \begin{pmatrix} \mathrm{e}^{i\theta_q/2} \\ \pm i\mathrm{e}^{-i\theta_q/2} \end{pmatrix} \tag{2.61}$$

and, around $\mathbf{K}'$,

$$\psi_{\pm,\mathbf{K}'}(\mathbf{k}) = \frac{1}{\sqrt{2}} \begin{pmatrix} \mathrm{e}^{-i\theta_q/2} \\ \pm i\mathrm{e}^{i\theta_q/2} \end{pmatrix} \tag{2.62}$$

We note that if we rotate the phase θ by 2π, the wave function changes sign indicating a phase of π. This is called Berry's phase, and shows that the wave function acts like a 2-component spinor.

2.4 Density of States

The density of states may be found using the energy spectrum

$$\rho_{\pm}(\varepsilon) = \frac{g_d}{(2\pi)^2} \int d\mathbf{k}\, \delta(\varepsilon - \varepsilon_{\pm}(\mathbf{k})) \tag{2.63}$$

where $g_d = 4$ is the band degeneracy factor (2 for spin and 2 for the two Dirac points). At the first order we find

$$\rho_{\pm}(\varepsilon) = \frac{g_d}{2\pi} \int k\, dk\, \delta(\varepsilon \mp \hbar v_F\, k) = \pm \frac{g_d \varepsilon}{2\pi(\hbar v_F)^2} H(\pm\varepsilon) \tag{2.64}$$

or

$$\rho(\varepsilon) = \frac{g_d |\varepsilon|}{2\pi(\hbar v_F)^2} \tag{2.65}$$

which is valid as long as the approximation $\varepsilon \approx \pm\hbar v_F k$ is good.

Considering the full tight-binding spectrum, Hobson and Nierenberg [50], have derived an analytical expression for the density of states, for the case $t' = 0$:

$$\begin{aligned}
&\rho_+(\varepsilon) = \rho_-(\varepsilon) = \rho(|\varepsilon|) = \frac{g_d\sqrt{3}}{2\pi^2} \frac{|\varepsilon|}{(\hbar v_F)^2} \frac{1}{\sqrt{\Lambda_0}}\, \mathrm{K}\left(\sqrt{\frac{\Lambda_1}{\Lambda_0}}\right), \\
&\Lambda_0 = \begin{cases} \left(1 + |\frac{\varepsilon}{t}|\right)^2 - \frac{\left[(\varepsilon/t)^2 - 1\right]^2}{4}, & -t \le \varepsilon \le t \\ 4|\frac{\varepsilon}{t}|, & -3t \le \varepsilon \le -t \quad \text{or} \quad t \le \varepsilon \le 3t, \end{cases} \\
&\Lambda_1 = \begin{cases} 4|\frac{\varepsilon}{t}|, & -t \le \varepsilon \le t \\ \left(1 + |\frac{\varepsilon}{t}|\right)^2 - \frac{\left[(\varepsilon/t)^2 - 1\right]^2}{4}, & -3t \le \varepsilon \le -t \quad \text{or} \quad t \le \varepsilon \le 3t, \end{cases}
\end{aligned} \tag{2.66}$$

where $\mathrm{K}(x)$ is the complete elliptic integral of the first kind [51].

A series expansion of the density of states, Eq. (2.66), at low energies may be found as follows. We define

$$\varphi\left(\frac{|\varepsilon|}{t}\right) = \frac{\sqrt{3}}{\pi} \frac{1}{\sqrt{\Lambda_0}}\, \mathbf{K}\left(\sqrt{\frac{\Lambda_1}{\Lambda_0}}\right) \tag{2.67}$$

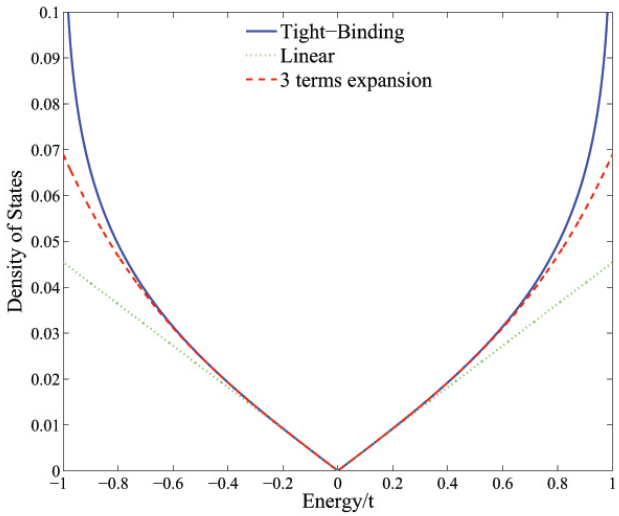

(a) The density of states

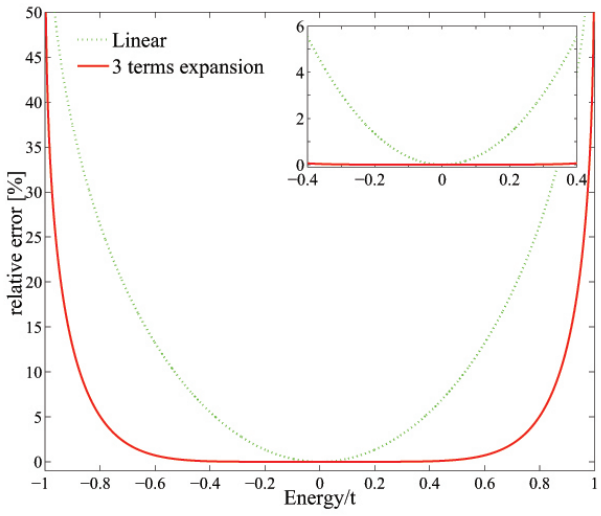

(b) The relative error

Figure 2.5: (a) The density of states of graphene, derived from tight-binding approach for $\hbar v_F = 6.576\,\text{eV.Å}$ and $t' = 0$ (solid line), the linear approximation (dotted line), and the higher approximation to it (up to c_2 in Eq. (2.69) (dashed line). (b) The relative error of the two approximations. Note that, for $|\varepsilon| < 0.5\,t$, the error is less than 10 %.

then

$$\rho(\varepsilon) = \frac{g_d}{2\pi} \frac{|\varepsilon|}{(\hbar v_F)^2} \varphi\left(\frac{|\varepsilon|}{t}\right). \tag{2.68}$$

For $x \equiv \frac{|\varepsilon|}{t} \lesssim \frac{1}{2}$, the function $\varphi(x)$ may be expanded as

$$\varphi(x) \cong \sum_{j=0} c_j \, x^{2j} \tag{2.69}$$

where

$$\begin{aligned} c_0 &= 1, \\ c_1 &= 1/3, \\ c_2 &= 5/27, \\ c_3 &= 31/243, \\ c_4 &= 71/729, \\ c_5 &= 517/6561, \\ &... \end{aligned}$$

Fig. 2.5 shows the density of states and the approximation to it up to the third term. As we see, the linear approximation may be considered as an acceptable approximation for $|\varepsilon| \lesssim 0.5\,t$, although the approximation with two more terms in the expansion shows a better approach even for the energies around $0.8\,t$.

2.5 Density of Electrons

We treat graphene as a uniform 2-dimensional background of positive ions. We assume that the ground state of such a system, under the gating conditions at

temperature T, is characterized by a uniform density per unit area of charge carriers in the graphene, given by

$$n(\mu) = \int_0^\infty d\varepsilon\, \rho_+(\varepsilon) f(\varepsilon,\mu) \; - \int_{-\infty}^0 d\varepsilon\, \rho_-(\varepsilon)\left[1 - f(\varepsilon,\mu)\right], \tag{2.70}$$

where $f(\varepsilon,\mu)$ is the Fermi-Dirac distribution,

$$f(\varepsilon,\mu) = \frac{1}{1+\exp\left[\beta\left(\varepsilon-\mu\right)\right]}, \tag{2.71}$$

where $\beta \equiv (k_B T)^{-1}$, and μ is the chemical potential. $\rho_\pm(\varepsilon)$ is the density of states in graphene's π electron (hole) bands given by Eq. (2.66). Note that for electron (hole) doping, one has $n > 0$ ($n < 0$) and consequently $\mu > 0$ ($\mu < 0$), whereas intrinsic graphene is characterized by $n = 0$ and $\mu = 0$. Since $\rho_+(\varepsilon) = \rho_-(\varepsilon) = \rho(|\varepsilon|)$ (Eq. (2.66)), the density of charge carriers becomes

$$n(\mu) = \int_0^\infty d\varepsilon\, \rho(\varepsilon) \left[\frac{1}{1+\mathrm{e}^{\beta(\varepsilon-\mu)}} - \frac{1}{1+\mathrm{e}^{\beta(\varepsilon+\mu)}}\right]. \tag{2.72}$$

For sufficiently low doping levels, such that, e.g., $|\mu| \sim k_B T \ll t$ (close to the Dirac points), one may use the linearized band density of states [11], $\rho(\varepsilon) \approx \frac{g_d|\varepsilon|}{2\pi(\hbar v_F)^2}$, giving

$$n(\mu) \approx \frac{g_d}{2\pi} \frac{1}{\left(\hbar v_F \beta\right)^2} \left[\mathrm{dilog}\left(1+\mathrm{e}^{-\beta\mu}\right) - \mathrm{dilog}\left(1+\mathrm{e}^{\beta\mu}\right)\right], \tag{2.73}$$

where dilog is the dilogarithm function defined, for $x > 0$, by [51]

$$\mathrm{dilog}(x) = \int_1^x \frac{\ln t}{1-t}\, dt. \tag{2.74}$$

We note that, at room temperature, e.g., $T = 300$ K, $k_B T \approx 0.026$ eV; therefore Eq. (2.73) is valid for room temperature, but nevertheless, the chemical potential

should be less than 1 eV. An approximation to Eq. (2.73) is

$$n(\mu) \approx \frac{g_d}{4\pi}\left(\frac{\mu}{\hbar v_F}\right)^2 \mathrm{sign}(\mu)\left[\alpha\left(\sqrt{1+\gamma^2\left(\frac{k_BT}{\mu}\right)^2}-1\right)+1\right], \tag{2.75}$$

where $\alpha = \frac{24(\ln 2)^2}{\pi^2}$ and $\gamma = \frac{\pi^2}{6\ln 2}$.

At $T = 0$, Eq. (2.72) reduces to

$$n_0(\mu) = \mathrm{sign}(\mu)\int_0^{|\mu|} d\varepsilon\, \rho(\varepsilon). \tag{2.76}$$

Inserting the series expansion of the density of states, Eq. (2.69), into the integral we find

$$n_0(\mu) \simeq \mathrm{sign}(\mu)\frac{g_d}{4\pi}\left(\frac{\mu}{\hbar v_F}\right)^2 \sum_{j=0}\frac{c_j}{j+1}\left(\frac{\mu}{t}\right)^{2j}. \tag{2.77}$$

Figure 2.6 shows the difference and percentage error. Considering only the linear term in the density of states, the density of electrons becomes

$$n_0(\mu) \approx \frac{g_d}{4\pi}\left(\frac{\mu}{\hbar v_F}\right)^2 \mathrm{sign}(\mu). \tag{2.78}$$

We see that the temperature effects manifest themselves mostly when $\mu \sim k_BT$, while the effect of nonlinear terms in the density of states appears for large μ. Expanding Eq. (2.75), up to the second order of k_BT/μ ($\mu \gg k_BT$), we find

$$n(\mu) \approx \frac{g_d}{4\pi}\left(\frac{\mu}{\hbar v_F}\right)^2 \mathrm{sign}(\mu)\left[1+\frac{\pi^2}{3}\left(\frac{k_BT}{\mu}\right)^2\right], \tag{2.79}$$

and Eq. (2.77) up to the second term is

$$n_0(\mu) \approx \frac{g_d}{4\pi}\left(\frac{\mu}{\hbar v_F}\right)^2 \mathrm{sign}(\mu)\left[1+\frac{1}{6}\frac{\mu^2}{t^2}\right]. \tag{2.80}$$

Comparison of the second terms in the two approximations shows that, at room temperature, the higher terms of the nonlinear density of states are comparable to

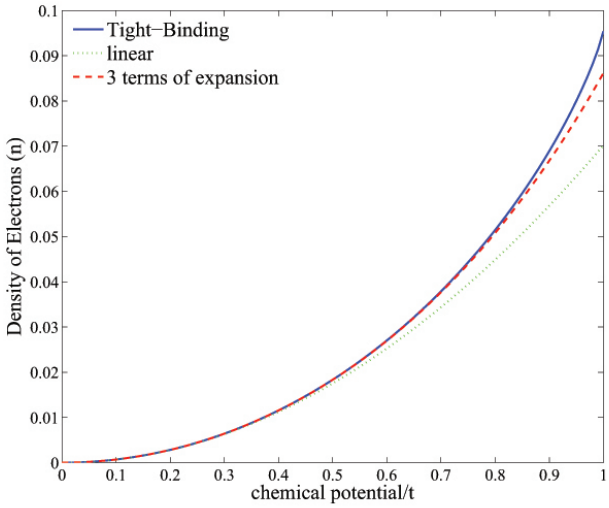

(a) The density of electrons

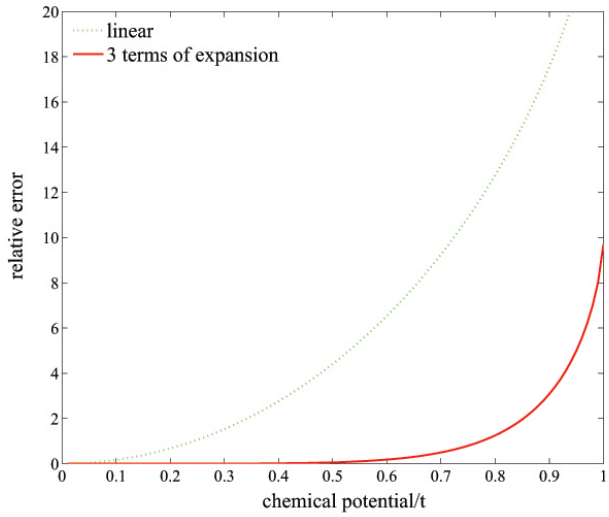

(b) The relative error

Figure 2.6: (a) The density of electrons of graphene, derived from the tight-binding approach for $\hbar v_F = 6.576\,\text{eV.Å}$ and $t' = 0$ (solid line), the linear density of states approximation (only c_0 in Eq. (2.77)) (dotted line), and the higher approximation of it (up to c_2 in Eq. (2.77) (dashed line). (b) The relative error of the two approximations. We note that using the expansion in the density of states shows a good approximation.

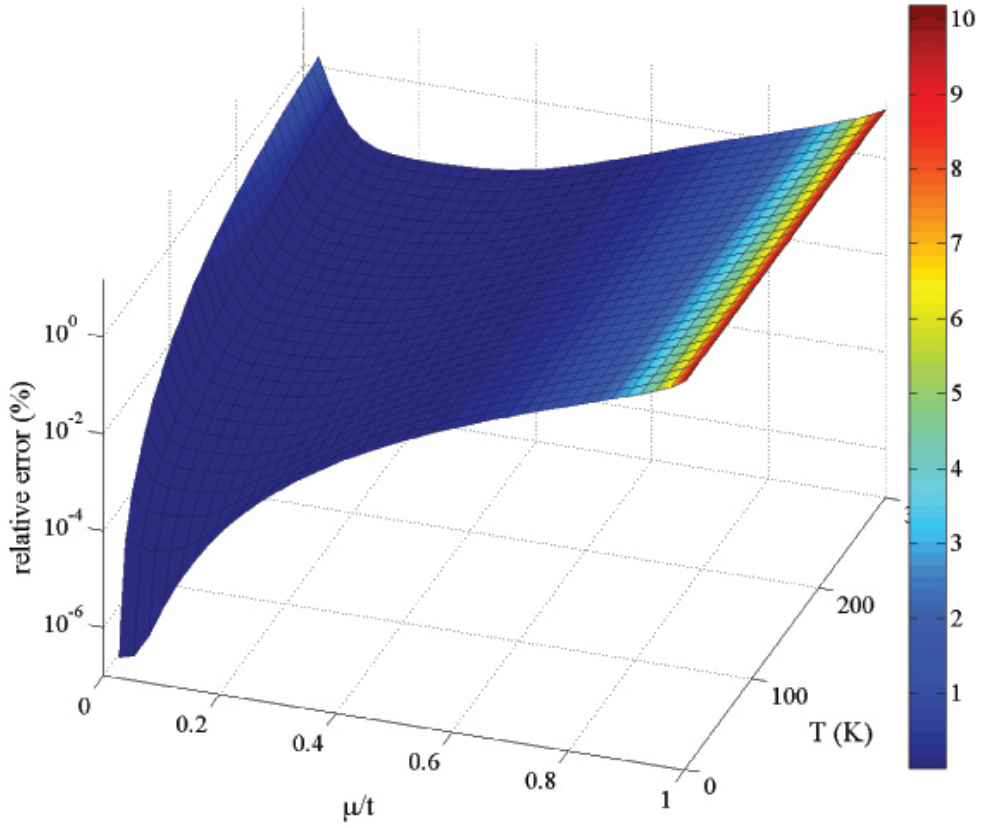

Figure 2.7: The relative error in the density of electrons calculated from Eq. (2.81) with respect to the one calculated from Eq. (2.72). For the range of parameters we use, the approximation method is good.

the effect of the temperature when $\mu_c \simeq \sqrt{\sqrt{2}\pi\, t\, k_B T} \approx 0.59$ eV for $T = 300$ K. Since the region of the effect of the temperature and that of the nonlinear density of states are different, one may take the summation of the two approximations as a valid approximation for both the effects of the temperature and the nonlinear terms,

$$\begin{aligned} n_0(\mu) \;\simeq\; & \operatorname{sign}(\mu)\frac{g_d}{4\pi}\left(\frac{\mu}{\hbar v_F}\right)^2 \left\{\sum_{j=1}\frac{c_j}{j+1}\left(\frac{\mu}{t}\right)^{2j}\right. \\ & \left. + \left[\alpha\left(\sqrt{1+\gamma^2\left(\frac{k_B T}{\mu}\right)^2}-1\right)+1\right]\right\}. \end{aligned} \tag{2.81}$$

Fig. 2.7 shows the relative error in the approximated formula with respect to the full density of carriers. As we see the approximated formula is accurate for sufficiently small chemical potentials ($\mu \ll t$).

2.6 Local Density of Electrons: Effect of Electric Potential

In order to analyze the response of graphene to an external charge, we need to find the effect of the electric potential on the local density of charge carriers. We use the approach of Ryzhii *et al.* [52] based on the Vlasov-type equations. If $f_e(\mathbf{p},\mathbf{r},t)$ and $f_e(\mathbf{p},\mathbf{r},t)$ stand for the graphene's π electron and hole distribution functions, respectively, then they should obey the following kinetic equations:

$$\begin{aligned} \frac{\partial f_e}{\partial t} + \mathbf{v_p}\cdot\frac{\partial f_e}{\partial \mathbf{r}} + \mathbf{F}_e(\mathbf{r},t)\cdot\frac{\partial f_e}{\partial \mathbf{p}} &= I_e, \\ \frac{\partial f_h}{\partial t} + \mathbf{v_p}\cdot\frac{\partial f_h}{\partial \mathbf{r}} + \mathbf{F}_h(\mathbf{r},t)\cdot\frac{\partial f_h}{\partial \mathbf{p}} &= I_h, \end{aligned} \tag{2.82}$$

where $\mathbf{p} \equiv \hbar\mathbf{k} = (p_x, p_y)$ is the electron (or hole) in-plane momentum, $\mathbf{v_p} = \partial\varepsilon_\mathbf{p}/\partial\mathbf{p}$ is the velocity of an electron (hole) with momentum $\mathbf{p}$, and $\mathbf{F}_{e(h)}$ is the force on an electron (hole) in the graphene plane, which in our problem is simply the in-plane force, due to the total electric potential $\Phi(\mathbf{r}, t)$; I_e and I_h denote the processes of electron and hole scattering and recombination, respectively. Eqs. (2.82) are simply the continuity equations for the electron and hole distributions. The second term in each equation governs the incoming and outgoing electrons and holes to the spatial elements of the phase space, and the third term governs the changes in the momentum elements of the phase space. We restrict discussion to the static case, when the Vlasov equations (2.82) reduce to:

$$\begin{aligned} \frac{\partial\varepsilon_\mathbf{p}}{\partial\mathbf{p}} \cdot \frac{\partial f_e}{\partial\mathbf{r}} + e\,\frac{\partial\Phi}{\partial\mathbf{r}} \cdot \frac{\partial f_e}{\partial\mathbf{p}} = 0, \\ \frac{\partial\varepsilon_\mathbf{p}}{\partial\mathbf{p}} \cdot \frac{\partial f_h}{\partial\mathbf{r}} - e\,\frac{\partial\Phi}{\partial\mathbf{r}} \cdot \frac{\partial f_h}{\partial\mathbf{p}} = 0. \end{aligned} \tag{2.83}$$

The static form of the Vlasov equations implies that the electron and hole distribution functions should have the forms $f_e = f_e(\varepsilon_\mathbf{p} + e\phi(\mathbf{r}))$ and $f_h = f_h(\varepsilon_\mathbf{p} - e\phi(\mathbf{r}))$, respectively. In equilibrium and absence of external charges, the electron and hole distribution functions are given from the Fermi-Dirac distribution, Eq. (2.71), $f_e = f(\varepsilon)$ and $f_h = 1 - f(\varepsilon)$. Therefore the local density of charge carriers (per unit area) in the graphene, is given by replacing μ by $\mu + e\phi(\mathbf{r})$ in Eq. (2.70), e.g.,

$$n(\mathbf{r}, \mu) = n(\mu + e\phi(\mathbf{r})). \tag{2.84}$$

2.7 Gated Graphene

A direct result of Eq. (2.84) is that the chemical potential of graphene may be imposed easily, by applying a gate voltage. We consider an infinite layer of graphene

on top of a substrate with the width $W_{\rm g}$. We choose the plane $z = 0$ to be at the graphene surface and the denote the gap between graphene and substrate by h. Under the substrate the gate potential is applied. We assume that the graphene is grounded, so that the electric potential on the graphene surface is zero; consequently, the electric field above the graphene is zero. Applying a fixed gate potential induces charges on the surfaces of both the substrate and graphene. One may easily determine the induced charge density on the graphene, $\sigma^0_{\rm gr}$, as a funtion of the gate potential, $V_{\rm gate}$. Symmetry of the system indicates that the electric field is perpendicular to the surfaces, and for the different regions, the electric field is

$$E_\perp(z) \equiv -\frac{\partial\phi(z)}{\partial z} = \begin{cases} 0, & z \geq 0 \\ -\frac{0-V_{\rm sub}}{h}, & -h < z < 0 \\ -\frac{V_{\rm sub}-V_{\rm gate}}{W_{\rm g}}, & z < -h, \end{cases} \tag{2.85}$$

where $V_{\rm sub}$ is the potential in the surface of substrate. The boundary conditions are

$$D_\perp(z = 0^+) - D_\perp(z = 0^-) = 0 - \varepsilon_1 \left(\frac{V_{\rm sub}}{h}\right) = 4\pi\,\sigma^0_{\rm gr}$$

$$\Rightarrow \sigma^0_{\rm gr} = \frac{-1}{4\pi}\frac{\varepsilon_1}{h}V_{\rm sub}, \tag{2.86}$$

$$E_\perp(z = -h + 0^+) - E_\perp(z = -h - 0^-) = \frac{V_{\rm sub}}{h} - \frac{V_{\rm sub} - V_{\rm gate}}{W_{\rm g}} = 4\pi\,\sigma^0_{\rm sub}$$

$$\Rightarrow \sigma^0_{\rm sub} = \frac{-1}{4\pi}\left[V_{\rm sub}\left(\frac{1}{h} + \frac{1}{W_{\rm g}}\right) - \frac{V_{\rm gate}}{W_{\rm g}}\right], \tag{2.87}$$

and

$$D_\perp(z = -h + 0^+) - D_\perp(z = -h - 0^-) = \varepsilon_1\left(\frac{V_{\rm sub}}{h}\right) - \varepsilon_2\left(-\frac{V_{\rm sub} - V_{\rm gate}}{W_{\rm g}}\right) = 0$$

$$\Rightarrow V_{\rm sub} = V_{\rm gate}\frac{\varepsilon_2/W_{\rm g}}{\varepsilon_1/h + \varepsilon_2/W_{\rm g}}, \tag{2.88}$$

where, ϵ_1 is the dielectric constant of the environment of the graphene and ϵ_2 is the dielectric constant of the substrate. Solving the set of equations for $\sigma^0_{\rm gr}$ respect to $V_{\rm gate}$, we find

$$\sigma^0_{\rm gr} = -\frac{\varepsilon_2}{4\pi}\frac{V_{\rm gate}}{W_{\rm g}}\frac{1}{1+\frac{\varepsilon_2}{\varepsilon_1}\frac{h}{W_{\rm g}}}. \tag{2.89}$$

In the limit $h \ll W_{\rm g}$

$$\sigma^0_{\rm gr} \approx -\frac{\varepsilon_2}{4\pi}\frac{V_{\rm gate}}{W_{\rm g}}. \tag{2.90}$$

Therefore the excess electron number density n_0 is

$$n_0 = -\frac{\sigma^0_{\rm gr}}{e} \simeq -\frac{\varepsilon_2}{4\pi e}\frac{V_{\rm gate}}{W_{\rm g}}. \tag{2.91}$$

$n_0 \gtrless 0$ defines the ground state density of charges on the gated graphene. However, the local density of charges changes in the presence of an external potential. The corresponding ground chemical potential of the gated graphene is given by the solution of Eq. (2.72) for μ as a function of n_0. The ground state chemical potential should be inserted in Eq. (2.84), in order to find the local density charge induced by the external potential due to the presence of the charge impurities in the environment. In other words, if $\phi_{\rm tot}(\mathbf{R})$ is the total electric potential at the surface of graphene, then the total induced charge on the graphene is

$$\sigma^{\rm ind}_{\rm gr} = -e\left(n\left(\mu + e\,\phi_{\rm tot}(\mathbf{R})\right) - n_0\right). \tag{2.92}$$

This is the starting point to attack the problem, which we define in detail in the next chapter.

Chapter 3

Basic Theory

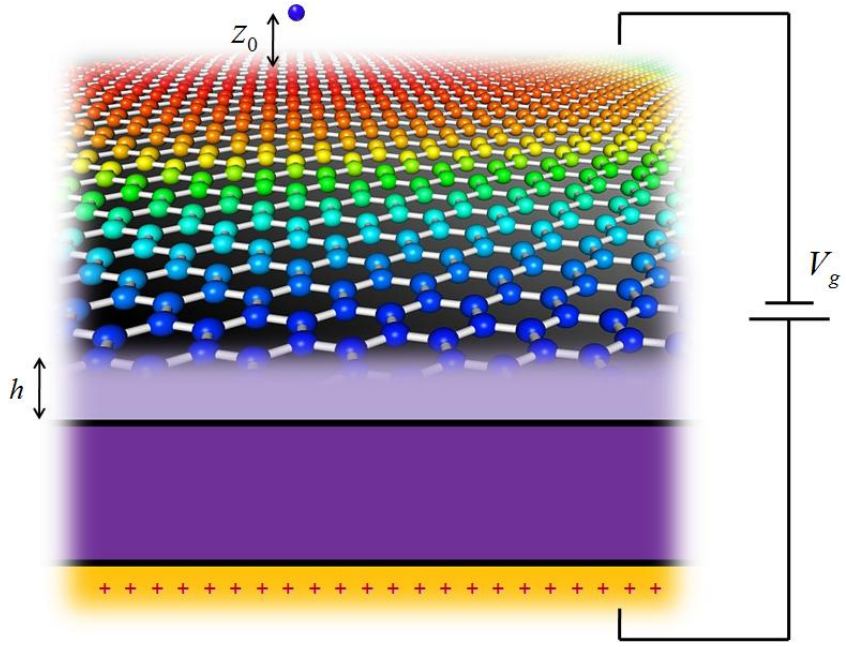

Figure 3.1: Schematic view of the problem.

3.1 Definition of Problem

We wish to evaluate the total electrostatic potential in the system, $\Phi(\mathbf{r}, z)$, due to an external point charge Ze placed at a fixed position $\{\mathbf{0}, z_0\}$, where $e(>0)$ is the charge of a proton. A schematic view of the problem is presented in Fig. 3.1. This perturbation induces surface charges on the surface of the substrate and on the graphene with the densities (per unit area) $\sigma_{\text{sub}}(\mathbf{r})$ and $\sigma_{\text{gr}}(\mathbf{r})$, respectively [27]. We treat the effects of both substrate and graphene as though they are structureless, allowing us to take both $\sigma_{\text{sub}}(\mathbf{r})$ and $\sigma_{\text{gr}}(\mathbf{r})$ as slowly varying functions of $\mathbf{r}$. The total (screened) electric potential in the system, Φ, should satisfy the corresponding Poisson equation for the system. If the external charge is above graphene surface, or between graphene and substrate, $z_0 > -h$, the Poisson equation is (assuming

the dielectric constant is 1)

$$\begin{cases} \nabla^2\Phi(\mathbf{r},z) = -4\pi\left[Ze\,\delta_2(\mathbf{r})\,\delta(z-z_0) + \sigma_{\rm gr}(\mathbf{r})\,\delta(z)\right] & z > -h, \\ \nabla^2\Phi(\mathbf{r},z) = 0 & z < -h, \end{cases} \tag{3.1}$$

The boundary conditions are

$$\Phi(-h^{+0}) = \Phi(-h^{-0}), \tag{3.2}$$

and

$$\left.\frac{\partial\Phi}{\partial z}\right|_{z=-h^{+0}} = \epsilon_{\rm s}\left.\frac{\partial\Phi}{\partial z}\right|_{z=-h^{-0}}. \tag{3.3}$$

where $\epsilon_{\rm s}$ is the dielectric constant of the substrate. We use the Fourier transform with respect to coordinates in the graphene plane, $\mathbf{r} \to \mathbf{k}$, to convert the Poisson Eq. (3.1) to a simpler equation

$$\Phi(\mathbf{r},z) = \int \frac{d^2\mathbf{k}}{(2\pi)^2} \mathrm{e}^{i\mathbf{k}.\mathbf{r}} \widetilde{\Phi}(\mathbf{k},z). \tag{3.4}$$

The Poisson equation becomes

$$\begin{cases} \frac{\partial^2}{\partial z^2}\widetilde{\Phi} - k^2\widetilde{\Phi} = -4\pi\left[Ze\,\delta(z-z_0) + \widetilde{\sigma}_{\rm gr}(\mathbf{k})\,\delta(z)\right] & z > -h, \\ \frac{\partial^2}{\partial z^2}\widetilde{\Phi} - k^2\widetilde{\Phi} = 0 & z < -h. \end{cases} \tag{3.5}$$

The solution of the equation is

$$\begin{cases} \widetilde{\Phi}_{>}(z) = \frac{2\pi Ze}{k}\,\mathrm{e}^{-k|z-z_0|} + \frac{2\pi}{k}\,\widetilde{\sigma}_{\rm gr}\,\mathrm{e}^{-k|z|} + A\,\mathrm{e}^{kz} + B\,\mathrm{e}^{-kz} & z > -h, \\ \widetilde{\Phi}_{<}(z) = C\,\mathrm{e}^{kz} + D\,\mathrm{e}^{-kz} & z < -h, \end{cases} \tag{3.6}$$

where A, B, C and D are coefficient (which depend on $\mathbf{k}$, in general) to be determined by applying the boundary conditions. Because the potential must not diverge when $|z| \to \infty$, we set $A = D = 0$. By applying the continuity condition, Eq. (3.2), we get

$$\frac{2\pi Ze}{k}\,\mathrm{e}^{-k(h+z_0)} + \frac{2\pi}{k}\,\widetilde{\sigma}_{\rm gr}\,\mathrm{e}^{-kh} + B\,\mathrm{e}^{kh} = C\,\mathrm{e}^{-kh}, \tag{3.7}$$

and by applying the condition Eq. (3.3) we find

$$2\pi Ze\,\mathrm{e}^{-k(h+z_0)} + 2\pi\widetilde{\sigma}_{\mathrm{gr}}\,\mathrm{e}^{-kh} - Bk\,\mathrm{e}^{kh} = \epsilon_{\mathrm{s}}Ck\,\mathrm{e}^{-kh}. \tag{3.8}$$

By solving these two equations we find

$$B = \frac{1-\epsilon_{\mathrm{s}}}{1+\epsilon_{\mathrm{s}}}\left[\frac{2\pi Ze}{k}\,\mathrm{e}^{-k(2h+z_0)} + \frac{2\pi}{k}\,\widetilde{\sigma}_{\mathrm{gr}}\,\mathrm{e}^{-2kh}\right], \tag{3.9}$$

and

$$C = \frac{2}{1+\epsilon_{\mathrm{s}}}\left[\frac{2\pi Ze}{k}\,\mathrm{e}^{-kz_0} + \frac{2\pi}{k}\,\widetilde{\sigma}_{\mathrm{gr}}\right]. \tag{3.10}$$

By substituting B and C into Eq. (3.6), we find the potential

$$\begin{cases} \widetilde{\Phi}_{>}(z) = \frac{2\pi}{k}\left\{Ze\,\mathrm{e}^{-k|z-z_0|} + \widetilde{\sigma}_{\mathrm{gr}}\,\mathrm{e}^{-k|z|} + \frac{1-\epsilon_{\mathrm{s}}}{1+\epsilon_{\mathrm{s}}}\left[Ze\,\mathrm{e}^{-k(z+2h+z_0)} + \widetilde{\sigma}_{\mathrm{gr}}\,\mathrm{e}^{-k(z+2h)}\right]\right\} \\ \widetilde{\Phi}_{<}(z) = \frac{2\pi}{k}\frac{2}{1+\epsilon_{\mathrm{s}}}\left[Ze\,\mathrm{e}^{k(z-z_0)} + \widetilde{\sigma}_{\mathrm{gr}}\,\mathrm{e}^{kz}\right]. \end{cases} \tag{3.11}$$

We note that the piecewise form of the total potential, Eq. (3.11) may be rewritten in a single formula which is valid for all values of z

$$\begin{aligned} \widetilde{\Phi}(\mathbf{k},z) &= \frac{2\pi Ze}{k}\left(\mathrm{e}^{-k|z-z_0|} + \frac{1-\epsilon_{\mathrm{s}}}{1+\epsilon_{\mathrm{s}}}\,\mathrm{e}^{-k|z+h|-k(z_0+h)}\right) \\ &\quad + \frac{2\pi}{k}\,\widetilde{\sigma}_{\mathrm{gr}}(\mathbf{k})\left(\mathrm{e}^{-k|z|} + \frac{1-\epsilon_{\mathrm{s}}}{1+\epsilon_{\mathrm{s}}}\,\mathrm{e}^{-k|z+h|-kh}\right). \end{aligned} \tag{3.12}$$

If the external charge is buried inside the substrate ($z_0 < -h$), the Poisson equation is

$$\begin{cases} \nabla^2\Phi(\mathbf{r},z) = -4\pi\,\sigma_{\mathrm{gr}}(\mathbf{r})\,\delta(z) & z > -h, \\ \nabla^2\Phi(\mathbf{r},z) = -\frac{4\pi}{\epsilon_{\mathrm{s}}}Ze\,\delta_2(\mathbf{r})\,\delta(z-z_0) & z < -h, \end{cases} \tag{3.13}$$

and the boundary conditions are the same as before, Eqs. (3.2, 3.3). The total potential in this case is

$$\begin{aligned} \widetilde{\Phi}(\mathbf{k},z) &= \frac{2\pi}{k}\frac{Ze}{\epsilon_{\mathrm{s}}}\left(\mathrm{e}^{-k|z-z_0|} - \frac{1-\epsilon_{\mathrm{s}}}{1+\epsilon_{\mathrm{s}}}\,\mathrm{e}^{-k|z+h|+k(z_0+h)}\right) \\ &\quad + \frac{2\pi}{k}\,\widetilde{\sigma}_{\mathrm{gr}}(\mathbf{k})\left(\mathrm{e}^{-k|z|} + \frac{1-\epsilon_{\mathrm{s}}}{1+\epsilon_{\mathrm{s}}}\,\mathrm{e}^{-k|z+h|-kh}\right). \end{aligned} \tag{3.14}$$

The total potential for both cases may be rewritten as

$$\begin{aligned}\widetilde{\Phi}(\mathbf{k},z) &= \frac{2\pi}{k}\frac{Ze}{\epsilon_{\rm h}}\left(\mathrm{e}^{-k|z-z_0|}+\frac{1-\epsilon_{\rm s}}{1+\epsilon_{\rm s}}\,\mathrm{e}^{-k|z+h|-k|z_0+h|}\mathrm{sign}(z_0+h)\right)\\ &+\frac{2\pi}{k}\,\widetilde{\sigma}_{\rm gr}(\mathbf{k})\left(\mathrm{e}^{-k|z|}+\frac{1-\epsilon_{\rm s}}{1+\epsilon_{\rm s}}\,\mathrm{e}^{-k|z+h|-kh}\right),\end{aligned} \tag{3.15}$$

where sign is the signum function and $\epsilon_{\rm h}$ is the dielectric constant of the "host" environment in which that charge resides ($\epsilon_{\rm h}=1$ for $z_0>-h$ and $\epsilon_{\rm h}=\epsilon_{\rm s}$ for $z_0<-h$).

From the physical point of view, the total potential may be written as the superposition of potential of external and induced charges

$$\widetilde{\Phi}=\widetilde{\Phi}_{\rm ext}+\widetilde{\Phi}_{\rm ind}, \tag{3.16}$$

where

$$\widetilde{\Phi}_{\rm ext}(\mathbf{k},z)=\frac{2\pi}{k}\frac{Ze}{\epsilon_{\rm h}}\,\mathrm{e}^{-k|z-z_0|} \tag{3.17}$$

is the potential of the external charge screened by the dielectric constant, $\epsilon_{\rm h}$, and

$$\widetilde{\Phi}_{\rm ind}(\mathbf{k},z)=\widetilde{\Phi}_{\rm gr}(\mathbf{k},z)+\widetilde{\Phi}_{\rm sub}(\mathbf{k},z)=\frac{2\pi}{k}\left[\widetilde{\sigma}_{\rm gr}(\mathbf{k})\,\mathrm{e}^{-k|z|}+\widetilde{\sigma}_{\rm sub}(\mathbf{k})\,\mathrm{e}^{-k|z+h|}\right] \tag{3.18}$$

is the total induced potential in the system. $\widetilde{\sigma}_{\rm sub}(\mathbf{k})$ denotes the charge density induced on the substrate. One may use the boundary condition

$$-\left.\frac{\partial\widetilde{\Phi}}{\partial z}\right|_{z=-h^{+0}}+\left.\frac{\partial\widetilde{\Phi}}{\partial z}\right|_{z=-h^{-0}}=2\pi\,\widetilde{\sigma}_{\rm sub} \tag{3.19}$$

to find the $\widetilde{\sigma}_{\rm sub}(\mathbf{k})$:

$$\widetilde{\sigma}_{\rm sub}(\mathbf{k})=\frac{1-\epsilon_{\rm s}}{1+\epsilon_{\rm s}}\left[\frac{Ze}{\epsilon_{\rm h}}\,\mathrm{sign}(h+z_0)\mathrm{e}^{-k|h+z_0|}+\widetilde{\sigma}_{\rm gr}(\mathbf{k})\mathrm{e}^{-kh}\right]. \tag{3.20}$$

Substituting $\widetilde{\sigma}_{\rm sub}(\mathbf{k})$ into Eq. (3.18), we find the total induced potential

$$\begin{aligned}\widetilde{\Phi}_{\rm ind}(\mathbf{k},z) &= \frac{2\pi}{k}\widetilde{\sigma}_{\rm gr}(\mathbf{k})\left(\mathrm{e}^{-k|z|}-\frac{\epsilon_{\rm s}-1}{\epsilon_{\rm s}+1}\,\mathrm{e}^{-k|z+h|-kh}\right)\\ &-\frac{2\pi}{k}\frac{Ze}{\epsilon_{\rm h}}\frac{\epsilon_{\rm s}-1}{\epsilon_{\rm s}+1}\,\mathrm{e}^{-k|z+h|-k|z_0+h|}\,\mathrm{sign}(z_0+h).\end{aligned} \tag{3.21}$$

We note that the last term is the classical image of the point charge Ze, in the substrate with dielectric constant $\epsilon_{\rm s}$, whereas the second term (in the brackets) is the image of the induced charge density on the surface of graphene.

By using the inverse Fourier transform, we find

$$\begin{aligned}\Phi_{\rm ind}\left(\mathbf{r},z\right) &= -\frac{Ze}{\epsilon_{\rm h}}\frac{\epsilon_{\rm s}-1}{\epsilon_{\rm s}+1}\frac{\mathrm{sgn}(z_0+h)}{\sqrt{r^2+\left(|z_0+h|+|z+h|\right)^2}} \\ &\quad+\int d^2\mathbf{r}'\,\sigma_{\rm gr}(\mathbf{r}')\left[\frac{1}{\sqrt{(\mathbf{r}-\mathbf{r}')^2+z^2}}\right. \\ &\quad\left.-\frac{\epsilon_{\rm s}-1}{\epsilon_{\rm s}+1}\frac{1}{\sqrt{(\mathbf{r}-\mathbf{r}')^2+\left(|z+h|+h\right)^2}}\right]. \end{aligned} \tag{3.22}$$

The Fourier transform of Eq. (3.15) gives the total potential as a function of $\mathbf{r}$:

$$\begin{aligned}\Phi\left(\mathbf{r},z\right) &= \frac{Ze}{\epsilon_{\rm h}}\left[\frac{1}{\sqrt{r^2+(z-z_0)^2}}-\frac{\epsilon_{\rm s}-1}{\epsilon_{\rm s}+1}\frac{\mathrm{sign}(z_0+h)}{\sqrt{r^2+\left(|z_0+h|+|z+h|\right)^2}}\right] \\ &\quad+\int d^2\mathbf{r}'\,\sigma_{\rm gr}(\mathbf{r}')\left[\frac{1}{\sqrt{(\mathbf{r}-\mathbf{r}')^2+z^2}}\right. \\ &\quad\left.-\frac{\epsilon_{\rm s}-1}{\epsilon_{\rm s}+1}\frac{1}{\sqrt{(\mathbf{r}-\mathbf{r}')^2+\left(|z+h|+h\right)^2}}\right]. \end{aligned} \tag{3.23}$$

Further, in the spirit of a temperature-dependent TF model, we express the induced charge density in graphene as [27, 56, 57]

$$\sigma_{\rm gr}(\mathbf{r}) = -e\left[n\left(\mu+e\phi(\mathbf{r})\right)-n\left(\mu\right)\right], \tag{3.24}$$

where $n\left(\mu\right)$ is given by Eq. (2.70). We note that we have denoted the total electrostatic potential in the graphene plane by

$$\phi(\mathbf{r}) \equiv \Phi(\mathbf{r},z)|_{z=0}\,. \tag{3.25}$$

Inserting Eq. (3.24) in Eq. (3.23) and setting $z = 0$, one obtains the following non-linear integral equation for $\phi(\mathbf{r})$, [27]

$$\begin{aligned}\phi(\mathbf{r}) &= \phi_0(\mathbf{r}) - e\int d^2\mathbf{r}'\ \left[n\left(\mu + e\phi(\mathbf{r}')\right) - n\left(\mu\right)\right] \\ &\times \left[\frac{1}{\|\mathbf{r}-\mathbf{r}'\|} - \frac{\epsilon_\mathrm{s}-1}{\epsilon_\mathrm{s}+1}\frac{1}{\sqrt{(\mathbf{r}-\mathbf{r}')^2+4h^2}}\right],\end{aligned} \tag{3.26}$$

where

$$\phi_0(\mathbf{r}) = \frac{Ze}{\epsilon_\mathrm{h}}\left[\frac{1}{\sqrt{r^2+z_0^2}} - \frac{\epsilon_\mathrm{s}-1}{\epsilon_\mathrm{s}+1}\frac{\mathrm{sign}(z_0+h)}{\sqrt{r^2+\left(|z_0+h|+h\right)^2}}\right] \tag{3.27}$$

is the value of the potential due to the external charge in the presence of the substrate alone, evaluated at $z = 0$. Once the integral equation, Eq. (3.26), is solved for the total potential in the plane of graphene, one may use Eq. (3.24) to evaluate the induced charge density in graphene, whose Fourier transform may be used in Eq. (3.21) to yield the total induced potential for any value of z.

3.2 Linearized Thomas-Fermi Model

One should solve Eq. (3.26) in a self-consistent way. Because the density of charge carriers, inside the integral, is such a complicated function of potential, there is no analytical solution for the equation. As the simplest approximation, people usually use the linearized TF model. When $|n|$ is large so that $e|\phi(0)| \ll |\mu|$, one may approximate the density of charge carriers as a linear expansion at ground chemical potential, for small perturbation of potential,

$$n_\mathrm{ind}(\mathbf{r}) \approx e\phi(\mathbf{r})\frac{\partial n}{\partial \mu}, \tag{3.28}$$

where n as a function of μ is given by Eq. (2.72). By substituting the Fourier transform of Eq. (3.28) into Eq. (3.15) and setting $z = 0$, we find

$$\begin{aligned}\widetilde{\phi}_{\rm lin}(\mathbf{k}) &= \frac{2\pi}{k}\frac{Ze}{\epsilon_h}\left[\mathrm{e}^{-k|z_0|} - \frac{\epsilon_s - 1}{\epsilon_s + 1}\mathrm{e}^{-kh-k|z_0+h|}\mathrm{sign}(z_0+h)\right] \\ &\quad -\frac{2\pi e^2}{k}\frac{\partial n}{\partial \mu}\widetilde{\phi}_{\rm lin}(\mathbf{k})\left(1 - \frac{\epsilon_s - 1}{\epsilon_s + 1}\mathrm{e}^{-2kh}\right). \end{aligned} \tag{3.29}$$

Using the definition of the background dielectric constant due to substrate,

$$\epsilon_{\rm bg}(k) = \left(1 - \frac{\epsilon_{\rm s} - 1}{\epsilon_{\rm s} + 1}\,\mathrm{e}^{-2kh}\right)^{-1}, \tag{3.30}$$

defining $v_C(k) = 2\pi e^2/k$, and recalling the definition of the polarization function of free graphene, $\Pi(k)$, which is constant in the LTF model, given by $\Pi_{\rm TF} \equiv \partial n(\mu)/\partial\mu$, one may write the solution of the linear Eq. (3.29) as

$$\widetilde{\phi}_{\rm lin}(\mathbf{k}) = \frac{\epsilon_{\rm bg}(k)}{\epsilon_{\rm bg}(k) + v_C(k)\Pi(k)}\,\widetilde{\phi}_0(\mathbf{k}), \tag{3.31}$$

where $\widetilde{\phi}_0(\mathbf{k})$ is the Fourier transform of the potential in Eq. (3.27), which is given by

$$\widetilde{\phi}_0(\mathbf{k}) = \frac{2\pi Ze}{k}\begin{cases} \frac{\mathrm{e}^{-kz_0}}{\epsilon_{\rm bg}(k)} & \text{if } z_0 > 0 \\ \mathrm{e}^{kz_0} + \left[\frac{1}{\epsilon_{\rm bg}(k)} - 1\right]\mathrm{e}^{-kz_0} & \text{if } -h < z_0 < 0 \\ \frac{\mathrm{e}^{kz_0}}{\epsilon^0_{\rm bg}} & \text{if } z_0 < -h, \end{cases} \tag{3.32}$$

where $\epsilon^0_{\rm bg} \equiv \epsilon_{\rm bg}(0) = (\epsilon_{\rm s} + 1)/2$. By taking the Fourier transform of Eq. (3.31), we find the linearized solution of the TF model. Similar to the nonlinear case, one may write a self-consistent integral equation for the linearized TF model (see Eq. (3.26))

$$\phi_{\rm lin}(\mathbf{r}) = \phi_0(\mathbf{r}) - \frac{q_{\rm s}}{2\pi\epsilon^0_{\rm bg}}\int d^2\mathbf{r}'\,\phi_{\rm lin}(\mathbf{r}')\left[\frac{\epsilon^0_{\rm bg}}{\|\mathbf{r}-\mathbf{r}'\|} - \frac{\epsilon^0_{\rm bg} - 1}{\sqrt{(\mathbf{r}-\mathbf{r}')^2 + 4h^2}}\right], \tag{3.33}$$

where $\phi_0(\mathbf{r})$ is given by Eq. (3.27), and $q_{\rm s} = 2\pi e^2\Pi_{\rm TF}$ is the Thomas-Fermi inverse screening length of free graphene.

We note that at zero temperature intrinsic graphene ($\mu = 0$), linearized TF predicts no screening for the external charges because

$$\left.\frac{\partial n}{\partial \mu}\right|_{\mu=0,\,T=0} = \frac{\partial}{\partial \mu}\left(\mathrm{sign}(\mu)\int_0^{|\mu|} d\varepsilon\,\rho(\varepsilon)\right)\Bigg|_{\mu=0} = \rho(0) = 0, \tag{3.34}$$

and therefore $q_{\mathrm{s}} = 0$ so that $\phi_{\mathrm{lin}}(\mathbf{r}) = \phi_0(\mathbf{r})$. One may realize that zero external charge screening leads to zero conduction according to Boltzmann conductivity theory.

In the zero gap limit, one obtains from Eq. (3.31) a more compact expression for the total potential in the LTF model,

$$\widetilde{\phi}(\mathbf{k}) = \frac{2\pi Ze}{k\epsilon^0_{\mathrm{bg}} + q_s}\,\mathrm{e}^{-k|z_0|}, \tag{3.35}$$

where the inverse screening length of free graphene, q_s, is obtained from Eq. (2.73) within the linearized DOS as [17]

$$q_s \approx \frac{2g_d e^2}{\beta\left(\hbar v_F\right)^2}\,\ln\left[2\cosh\left(\beta\mu/2\right)\right]. \tag{3.36}$$

It is clear then that, at zero temperature, intrinsic graphene cannot screen external charges in the LTF model because $q_s \to 0$ [17]. On the other hand, when either $n \neq 0$ or $T > 0$ or both, the inverse Fourier transform of Eq. (3.35) gives a total potential with the asymptotic form [25] $\phi(r) \sim \left(Ze\epsilon^0_{\mathrm{bg}}\right)/\left(q_s^2 r^3\right)$ for $r \gg q_s^{-1} \gg |z_0|$, and with the limiting value at the origin $\phi(0) = \left[Ze/\left(\epsilon^0_{\mathrm{bg}} z_0\right)\right]\left[1 - \zeta\,\mathrm{e}^{\zeta}\,\mathrm{E}_1\left(\zeta\right)\right]$, where $\zeta \equiv q_s z_0/\epsilon^0_{\mathrm{bg}}$ and E_1 is the exponential integral function [51].

3.3 Density Functional Theory

We found the energy spectrum of graphene, using the tight-binding approach, in the previous chapter. Here we should emphasize that, in a real physical situation

we need to include electron-electron interaction. Including that interaction in the hamiltonian of the system, the ground state energy, ε, of the corresponding electronic system could be found either by solving the Schrödinger equation or from the Rayleigh-Ritz minimal principle,

$$\varepsilon = \min_{\Psi}\langle\Psi|H|\Psi\rangle, \tag{3.37}$$

where Ψ is a trial function for the system. Hohenberg and Kohn [53], formulated another minimal principle in terms of trial densities $n(\mathbf{r})$, rather than the trial wave functions. Following their method one may first fix a trial density $n(\mathbf{r})$ and name the class of trial function which gives $n(\mathbf{r})$ by Ψ_n^α. we define

$$\begin{aligned} E[n(\mathbf{r})] &\equiv \min_\alpha\langle\Psi_n^\alpha|H|\Psi_n^\alpha\rangle \\ &= \int V_{\text{ext}}(\mathbf{r})n(\mathbf{r})d\mathbf{r} + \min_\alpha\langle\Psi_n^\alpha|T+U|\Psi_n^\alpha\rangle, \end{aligned} \tag{3.38}$$

where T is the kinetic part of hamiltonian, U is the electron-electron interaction, and V_{ext} is the external potential. Then the ground state energy is given by minimizing $E[n(\mathbf{r})]$ with respect to $n(\mathbf{r})$

$$\varepsilon = \min_{n(\mathbf{r})}E[n(\mathbf{r})]. \tag{3.39}$$

We note that density dependent expressions for both the exchange and correlation energy per electron in graphene, are available in the local density approximation (LDA) only for density variations with respect to the equilibrium case of intrinsic, or undoped, graphene having $\mu = 0$, in the limits of zero temperature, zero gap, and linearized band DOS [28, 29]. At low energies where the electrons in graphene are described by massless Dirac-fermions, the Thomas-Fermi kinetic energy functional is [45]

$$T[n(\mathbf{r})] = \hbar v_F \frac{2\sqrt{\pi}}{3}\text{sign}[n(\mathbf{r})]|n(\mathbf{r})|^{3/2}. \tag{3.40}$$

The full energy functional is

$$E[n(\mathbf{r})] = \hbar v_F \left[\frac{2\sqrt{\pi}}{3} \int d\mathbf{r}\, \mathrm{sign}(n)|n|^{3/2} + \frac{r_s}{2} \int d\mathbf{r}' \int d\mathbf{r} \frac{n(\mathbf{r})n(\mathbf{r}')}{|\mathbf{r}-\mathbf{r}'|} + \frac{E_{\mathrm{xc}}[n]}{\hbar v_F} + \frac{1}{\hbar v_F} \int d\mathbf{r}\, V_{\mathrm{ext}} n(\mathbf{r}) - \frac{\mu}{\hbar v_F} \int d\mathbf{r}\, n(\mathbf{r}) \right], \tag{3.41}$$

where $r_s = e^2/(\hbar v_F \epsilon_{\mathrm{bg}})$. The second term in Eq. (3.41) is the Hartree part of the Coulomb interaction, E_{xc} is the energy contribution due to exchange-correlation, and the fourth term is the potential of external charge. In order to find the energy, one may set the derivative of $E[n]$, with respect to n, equal to zero:

$$\frac{\delta E}{\delta n} = \hbar v_F \mathrm{sign}(n)\sqrt{\pi|n|} + \frac{\mathrm{e}^2}{\epsilon_{\mathrm{bg}}} \int d\mathbf{r}' \frac{n(\mathbf{r}')}{|\mathbf{r}-\mathbf{r}'|} + V_{\mathrm{xc}} + V_{\mathrm{ext}} - \frac{\mu}{\hbar v_F} = 0. \tag{3.42}$$

We note that, except for the exchange-correlation term, the other terms are the same as in the TF Eq. (3.26), when $h = 0$, $T = 0$, and $\mu = 0$; therefore, the density of charge carriers n, as a function of potential energy U, is obtained from Eq. (2.73) in the limit of zero temperature as follows:

$$n(U) = \frac{U^2 \mathrm{sign}(U)}{\pi(\hbar v_F)^2}. \tag{3.43}$$

3.3.1 Exchange-Correlation Potential for Intrinsic Graphene

The exchange-correlation potential, $V_{xc}(\mathbf{r})$, is a functional of the ground state density of charge carriers, although the exact expression for V_{xc} is unknown. However, it may be found approximately by applying the local-density approximation to get [29]

$$V_{xc}(\mathbf{r}) = V_{xc}^{\mathrm{hom}}(n)|_{n \to n_c(\mathbf{r})}, \tag{3.44}$$

where $V_{xc}^{\mathrm{hom}}(n)$ is the reference exchange-correlation potential of a uniform 2D liquid of massless Dirac fermions with carrier density n. The relation between $V_{xc}^{\mathrm{hom}}(n)$

and the ground-state energy per excess carrier, $\delta\varepsilon_{xc}(n)$ is

$$V_{xc}^{\mathrm{hom}}(n) = \frac{\partial\left[n\delta\varepsilon_{xc}(n)\right]}{\partial n}. \tag{3.45}$$

The expression used for $\varepsilon_{xc}(n)$ depends on the zero of energy. Usually it is chosen such that $V_{xc}^{\mathrm{hom}}(n=0) = 0$. In the next section we provide a convenient expression for the excess exchange-correlation energy, calculated at the random-phase approximation (RPA) level.

A. Exchange Potential

The first order exchange contribution to $\delta\varepsilon_{xc}(n)$ is [29]

$$\delta\varepsilon_x(n) = \varepsilon_F \alpha_{\mathrm{gr}} F(\Lambda), \tag{3.46}$$

where ε_F is the Fermi energy, which is given by

$$\varepsilon_F = \mathrm{sign}(n)\hbar v_F k_F. \tag{3.47}$$

Here $k_F = (4\pi|n|/g_d)$ is the Fermi wave vector. The quantity α_{gr} is defined as $\alpha_{\mathrm{gr}} = g_d e^2/(\varepsilon_{\mathrm{bg}}\hbar v_F) \equiv g_d \alpha_{\mathrm{ee}}$, where α_{ee} is the graphene's fine structure constant. The ultraviolet cut-off Λ is defined as $\Lambda = k_{\mathrm{max}}/k_F$. k_{max} is chosen from [29]

$$\pi k_{\mathrm{max}}^2 = \eta\frac{(2\pi)^2}{A_0}, \tag{3.48}$$

where A_0 is the area of the unit cell of graphene lattice, $A_0 = 3\sqrt{3}a^2/2 \sim 5.2\,\text{Å}^2$ and η is a dimensionless number with $\eta \in (0, 1]$. The optimal value of η should be determined by comparing the model's predictions with experiment, although this has not yet been done. The Λ may be rewritten as

$$\Lambda(n) = \sqrt{g_d\eta}\frac{1}{\sqrt{|n|A_0}} = \sqrt{\frac{n_0}{|n|}}. \tag{3.49}$$

By substituting Eq. (3.46 in Eq. (3.45), we find

$$\begin{aligned} V_x^{\rm hom}(n) &\equiv \frac{\partial\left[n\delta\varepsilon_x(n)\right]}{\partial n} = \delta\varepsilon_x(n) + n\frac{\partial}{\partial n}\left(\delta\varepsilon_x(n)\right) \\ &= \varepsilon_F\alpha_{\rm gr}F(\Lambda) + \alpha_{\rm gr}n\frac{\partial\varepsilon_F}{\partial n}F(\Lambda) + \varepsilon_F\alpha_{\rm gr}n\frac{\partial F}{\partial\Lambda}\frac{\partial\Lambda}{\partial n}. \end{aligned} \tag{3.50}$$

It is easy to check that

$$n\frac{\partial\varepsilon_F}{\partial n} = \frac{1}{2}\varepsilon_F, \tag{3.51}$$

and

$$n\frac{\partial\Lambda}{\partial n} = -\frac{1}{2}\Lambda. \tag{3.52}$$

Polini *et al.* chose the following formula for $F(\Lambda)$ to parameterize their data:

$$F(\Lambda) = \frac{1}{6g_d}\ln(\Lambda) + \frac{a_e}{1+b_e\Lambda^{c_e}}, \tag{3.53}$$

where the first term is calculated analytically, and the numerical constants are given by

$$\begin{aligned} a_e &= 0.0173671, \\ b_e &= 3.6642\times10^{-7}, \\ c_e &= 1.6784. \end{aligned} \tag{3.54}$$

From Eq. (3.53) we find

$$\frac{\partial F}{\partial\Lambda} = \frac{1}{6g_d}\frac{1}{\Lambda} - \frac{a_eb_ec_e}{\left(1+b_e\Lambda^{c_e}\right)^2}\frac{\Lambda^{c_e}}{\Lambda}. \tag{3.55}$$

Therefore the exchange potential is

$$V_x = \frac{3}{2}\varepsilon_F\alpha_{\rm gr}F(\Lambda) - \frac{1}{2}\varepsilon_F\alpha_{\rm gr}\Lambda\left[\frac{1}{6g_d}\frac{1}{\Lambda} - \frac{a_eb_ec_e}{\left(1+b_e\Lambda^{c_e}\right)^2}\frac{\Lambda^{c_e}}{\Lambda}\right], \tag{3.56}$$

or

$$V_x = \frac{3}{2}\varepsilon_F \alpha_{\rm gr} \frac{1}{6g_d}\left[-\frac{1}{3} + \ln(\Lambda) + 6g_d \frac{a_e}{1+b_e\Lambda^{c_e}} - \frac{1}{3} + 2g_d \frac{a_e b_e c_e}{\left(1+b_e\Lambda^{c_e}\right)^2}\Lambda^{c_e}\right]. \quad (3.57)$$

In terms of n we get

$$V_x = \frac{\sqrt{\pi}}{12}\frac{e^2}{\epsilon_{\rm bg}}{\rm sign}(n)\sqrt{|n|}\left[-1 + \frac{3}{2}\ln\left(\frac{n_0}{|n|}\right) + \frac{72\,a_e}{1+b_e\Lambda^{c_e}} + \frac{24\,a_e b_e c_e}{\left(1+b_e\Lambda^{c_e}\right)^2}\Lambda^{c_e}\right], \quad (3.58)$$

where $n_0 = \eta g_d/A_0 \approx \eta \times 7635 \times 10^{12}\,{\rm cm}^{-2}$. By substituting

$$n(U) = \frac{U^2}{\pi\left(\hbar v_F\right)^2}{\rm sign}(U), \quad (3.59)$$

we find

$$\begin{aligned} V_x \;=\; & \frac{1}{12}\frac{e^2}{\epsilon_{\rm bg}}\frac{U}{\hbar v_F}\left[-1 + 3\ln\left(\frac{U_0}{|U|}\right) + \frac{72\,a_e}{1+b_e\left(U_0/|U|\right)^{c_e}}\right. \\ & \left. + \frac{24\,a_e b_e c_e}{\left(1+b_e\left(U_0/|U|\right)^{c_e}\right)^2}\left(\frac{U_0}{|U|}\right)^{c_e}\right]. \end{aligned} \quad (3.60)$$

For $n \to 0$ the exchange potential goes to zero as follows:

$$V_x^{\rm hom}(n \to 0) \propto -{\rm sign}(n)\alpha_{\rm gr}\sqrt{|n|}\ln|n|. \quad (3.61)$$

B. RPA Correlation Potential

The RPA correlation energy is given by [29]

$$\delta\varepsilon_c^{\rm RPA}(n) = -\frac{1}{6g_d}\varepsilon_F\,\alpha_{\rm gr}^2\,\xi(\alpha_{\rm gr})\ln(\Lambda) + \varepsilon_F\,\alpha_{\rm gr}^2\frac{a_c(\alpha_{\rm gr})}{1+b_c(\alpha_{\rm gr})\Lambda^{c_c(\alpha_{\rm gr})}}, \quad (3.62)$$

where

$$\begin{aligned} a_c(\alpha_{\rm gr}) &= -1/(63.0963 + 57.351226\alpha_{\rm gr}), \\ b_c(\alpha_{\rm gr}) &= (7.75095 - 0.08371\alpha_{\rm gr}^{1.61167}) \times 10^{-7}, \\ c_c(\alpha_{\rm gr}) &= 1.527 + 0.0239\alpha_{\rm gr} - 0.001201\alpha_{\rm gr}^2, \end{aligned} \quad (3.63)$$

and

$$\xi(\alpha_{\rm gr}) = \frac{1}{2}\int_0^\infty \frac{dx}{(1+x^2)^2\left(\sqrt{1+x^2}+\pi\alpha_{\rm gr}/8\right)}. \tag{3.64}$$

Then the RPA correlation potential is given by

$$\begin{aligned} V_c^{\rm hom}(n) &\equiv \frac{\partial\left[n\delta\varepsilon_c^{\rm RPA}(n)\right]}{\partial n} = \delta\varepsilon_c^{\rm RPA}(n) + n\frac{\partial}{\partial n}\delta\varepsilon_c^{\rm RPA}(n) \\ &= \frac{1}{12g_d}\varepsilon_F\,\alpha_{\rm gr}^2\,\xi(\alpha_{\rm gr})\left[-3\ln(\Lambda)+1\right] \\ &\quad +\frac{1}{2}\varepsilon_F\,\alpha_{\rm gr}^2\left[\frac{3\,a_c}{1+b_c\Lambda^{c_c}} + \frac{a_c b_c c_c}{\left(1+b_c\Lambda^{c_c}\right)^2}\Lambda^{c_c}\right]. \end{aligned} \tag{3.65}$$

In terms of n we find

$$\begin{aligned} V_c^{\rm hom}(n) &= \frac{1}{2}{\rm sign}(n)\hbar v_F\sqrt{\pi|n|}\left(\frac{4e^2}{\epsilon_{\rm bg}\hbar v_F}\right)^2 \\ &\quad\times\left[-\frac{1}{16}\xi(\alpha_{\rm gr})\ln\left(\frac{n_0}{|n|}\right) + \frac{1}{24}\xi(\alpha_{\rm gr})\frac{3\,a_c}{1+b_c\Lambda^{c_c}}\right]. \end{aligned} \tag{3.66}$$

In the limit $n \to 0$ we have

$$V_c^{\rm hom}(n\to 0) \propto {\rm sign}(n)\alpha_{\rm gr}^2\xi(\alpha_{\rm gr})\sqrt{|n|}\ln|n|. \tag{3.67}$$

3.4 Random Phase Approximation (RPA)

Using the polarization function of graphene, we found the linear Thomas-Fermi approximation for the total potential, Eq. (3.31). This expression may be used to include the electron-electron interaction based on the RPA by renormalizing the polarization function. As mentioned before, near a **K** point, electronic states are described by the **k.p** equation (see Eq. (2.58)). The wave function is

$$\overrightarrow{\psi}_{s\mathbf{k}}(\mathbf{r}) = \frac{1}{L}\mathbf{F}_{s\mathbf{k}}\exp(i\mathbf{k}.\mathbf{r}), \tag{3.68}$$

with

$$\mathbf{F}_{s\mathbf{k}} = \frac{1}{\sqrt{2}} \begin{pmatrix} \mathrm{e}^{i\theta_k/2} \\ si\mathrm{e}^{-i\theta_k/2} \end{pmatrix}, \tag{3.69}$$

where L^2 is the area of the system, $s = 1$ and -1 denote the conduction and valance bands, respectively, and $\theta_k = \arcsin(k_x/|\mathbf{k}|)$.

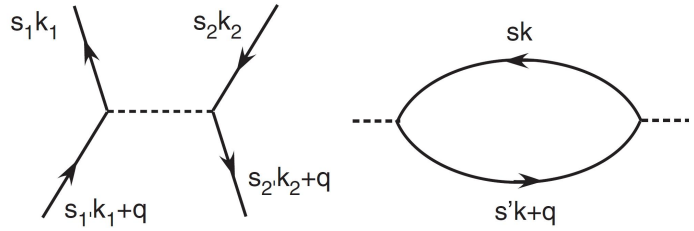

(a) (b)

Figure 3.2: (a) Feynman diagram of the matrix elements of the Coulomb interaction. (b) Diagram of the polarization function.

Fig. 3.2 shows the Feynman diagram for the matrix elements of the Coulomb interaction, which are given by [17]

$$V_{(s_1'\mathbf{k}_1+\mathbf{q},s_1\mathbf{k}_1)(s_2\mathbf{k}_2,s_2'\mathbf{k}_2+\mathbf{q})} = \frac{2\pi e^2}{\epsilon_{\mathrm{bg}}^0 q} \langle \mathbf{F}^\dagger_{s_1'\mathbf{k}_1+\mathbf{q}} | \mathbf{F}_{s_1\mathbf{k}_1} \rangle \langle \mathbf{F}^\dagger_{s_2\mathbf{k}_2} | \mathbf{F}_{s_2'\mathbf{k}_2+\mathbf{q}} \rangle, \tag{3.70}$$

where

$$\begin{aligned} \langle \mathbf{F}^\dagger_{s\mathbf{k}} | \mathbf{F}_{s'\mathbf{k}'} \rangle &= \frac{1}{2} \begin{pmatrix} \mathrm{e}^{-i\theta_k/2} & -si\mathrm{e}^{i\theta_k/2} \end{pmatrix} \begin{pmatrix} \mathrm{e}^{i\theta_{k'}/2} \\ s'i\mathrm{e}^{-i\theta_{k'}/2} \end{pmatrix} \\ &= \frac{1}{2}\mathrm{e}^{i(\theta_k-\theta_{k'})/2} \left[\mathrm{e}^{i(\theta_{k'}-\theta_k)} + ss' \right]. \end{aligned} \tag{3.71}$$

The static polarization function is given by [17]

$$\Pi(\mathbf{q}) = -\frac{g_d}{L^2} \sum_{s,s',\mathbf{k}} (f_{s\mathbf{k}} - f_{s'\mathbf{k}+\mathbf{q}}) \frac{|\langle \mathbf{F}^\dagger_{s\mathbf{k}} | \mathbf{F}_{s'\mathbf{k}+\mathbf{q}} \rangle|^2}{\varepsilon_{s\mathbf{k}} - \varepsilon_{s'\mathbf{k}+\mathbf{q}}}, \tag{3.72}$$

where $f_{s\mathbf{k}}$ is the Fermi-Dirac distribution. Because the system is isotropic, the polarization function is independent of the direction of the $\mathbf{q}$ vector. We find

$$\begin{aligned} |\langle \mathbf{F}^{\dagger}_{s\mathbf{k}} | \mathbf{F}_{s'\mathbf{k}+\mathbf{q}} \rangle|^2 &= \frac{1}{4}\left[1 + (ss')^2 + ss'\left(\mathrm{e}^{i(\theta_{k'}-\theta_k)} + \mathrm{e}^{-i(\theta_{k'}-\theta_k)}\right)\right] \\ &= \left(1 + ss'\cos\theta_{\mathbf{k}\mathbf{k}'}\right)/2, \end{aligned} \tag{3.73}$$

where $\cos\theta_{kk'} \equiv \cos(\theta_{k'} - \theta_k)$.

In Eq. (3.72), the effects of polarization of electrons in the valence band due to virtual interband transitions into the conduction band, $\Pi^0(\mathbf{q})$, is included. However, for a correct description of the static polarization function, we need to deduce it from the Eq. (3.72) [17]. $\Pi^0(\mathbf{q})$ is defined by

$$\Pi^0(\mathbf{q}) \equiv -\frac{g_d}{L^2}\sum_{s,s',\mathbf{k}} \left(f^0_{s\mathbf{k}} - f^0_{s'\mathbf{k}+\mathbf{q}}\right) \frac{|\langle \mathbf{F}^{\dagger}_{s\mathbf{k}} | \mathbf{F}_{s'\mathbf{k}+\mathbf{q}} \rangle|^2}{\varepsilon_{s\mathbf{k}} - \varepsilon_{s'\mathbf{k}+\mathbf{q}}}, \tag{3.74}$$

where

$$f^0_{s\mathbf{k}} = \begin{cases} 1 & \text{if } s = -1 \\ 0 & \text{if } s = +1 \end{cases}. \tag{3.75}$$

We define

$$\widetilde{f}_{s\mathbf{k}} = f_{s\mathbf{k}} - f^0_{s\mathbf{k}}. \tag{3.76}$$

Then the polarization function is

$$\Pi(\mathbf{q}) = -\frac{g_d}{L^2}\sum_{s,s',\mathbf{k}} \left(\widetilde{f}_{s\mathbf{k}} - \widetilde{f}_{s'\mathbf{k}+\mathbf{q}}\right) \frac{|\langle \mathbf{F}^{\dagger}_{s\mathbf{k}} | \mathbf{F}_{s'\mathbf{k}+\mathbf{q}} \rangle|^2}{\varepsilon_{s\mathbf{k}} - \varepsilon_{s'\mathbf{k}+\mathbf{q}}}. \tag{3.77}$$

Doing the summation over ss', the polarization function stet

$$\begin{aligned} \Pi(q) &= -\frac{g_d}{2L^2}\sum_{\mathbf{k}} \left[\frac{\left[\widetilde{f}_{\mathbf{k}+} - \widetilde{f}_{\mathbf{k}'+}\right](1 + \cos\theta_{kk'})}{\varepsilon_{\mathbf{k}} - \varepsilon_{\mathbf{k}'}} + \frac{\left[\widetilde{f}_{\mathbf{k}+} - \widetilde{f}_{\mathbf{k}'-}\right](1 - \cos\theta_{kk'})}{\varepsilon_{\mathbf{k}} + \varepsilon_{\mathbf{k}'}} \right. \\ &\left. - \frac{\left[\widetilde{f}_{\mathbf{k}-} - \widetilde{f}_{\mathbf{k}'+}\right](1 - \cos\theta_{kk'})}{\varepsilon_{\mathbf{k}} + \varepsilon_{\mathbf{k}'}} - \frac{\left[\widetilde{f}_{\mathbf{k}-} - \widetilde{f}_{\mathbf{k}'-}\right](1 + \cos\theta_{kk'})}{\varepsilon_{\mathbf{k}} - \varepsilon_{\mathbf{k}'}} \right]. \end{aligned} \tag{3.78}$$

Rearranging the terms, one may write the polarization function as

$$\Pi(q) = \Pi^{+}(q) + \Pi^{-}(q), \tag{3.79}$$

where

$$\Pi^{+}(q) = -\frac{g_d}{2L^2}\sum_{\mathbf{k}}\left[\frac{\left[\widetilde{f}_{\mathbf{k}+} - \widetilde{f}_{\mathbf{k}'+}\right](1+\cos\theta_{kk'})}{\varepsilon_{\mathbf{k}} - \varepsilon_{\mathbf{k}'}} + \frac{\left[\widetilde{f}_{\mathbf{k}+} + \widetilde{f}_{\mathbf{k}'+}\right](1-\cos\theta_{kk'})}{\varepsilon_{\mathbf{k}} + \varepsilon_{\mathbf{k}'}}\right], \tag{3.80}$$

$$\Pi^{-}(q) = +\frac{g_d}{2L^2}\sum_{\mathbf{k}}\left[\frac{\left[\widetilde{f}_{\mathbf{k}-} - \widetilde{f}_{\mathbf{k}'-}\right](1+\cos\theta_{kk'})}{\varepsilon_{\mathbf{k}} - \varepsilon_{\mathbf{k}'}} + \frac{\left[\widetilde{f}_{\mathbf{k}-} + \widetilde{f}_{\mathbf{k}'-}\right](1-\cos\theta_{kk'})}{\varepsilon_{\mathbf{k}} + \varepsilon_{\mathbf{k}'}}\right], \tag{3.81}$$

where $\mathbf{k}' \equiv \mathbf{k} + \mathbf{q}$ and we have used the linear expression of the energy spectrum, $\varepsilon_{\mathbf{k}\pm} = \pm\hbar v_F|\mathbf{k}|$. In the limit of a large system, that is of closely-spread k-values, we replace the summation with an integral, according to the prescription

$$\frac{1}{L^2}\sum_{\mathbf{k}} \to \frac{1}{(2\pi)^2}\int d\mathbf{k}. \tag{3.82}$$

Because of the symmetry of the integrand, for the integral involving the terms of $\widetilde{f}_{\mathbf{k}'\pm}$ one may just use change the variable $\mathbf{k} \to \mathbf{k} + \mathbf{q}$ to write the polarization function terms as

$$\begin{aligned}\Pi^{+}(q) &= -\frac{g_d}{(2\pi)^2}\int d\mathbf{k}\left[\frac{\widetilde{f}_{\mathbf{k}+}(1+\cos\theta_{kk'})}{\varepsilon_{\mathbf{k}} - \varepsilon_{\mathbf{k}'}} + \frac{\widetilde{f}_{\mathbf{k}+}(1-\cos\theta_{kk'})}{\varepsilon_{\mathbf{k}} + \varepsilon_{\mathbf{k}'}}\right] \\ &= -\frac{2g_d}{(2\pi)^2}\int d\mathbf{k}\left[\frac{\widetilde{f}_{\mathbf{k}+}(\varepsilon_{\mathbf{k}} + \varepsilon_{\mathbf{k}'}\cos\theta_{kk'})}{\varepsilon_{\mathbf{k}}^2 - \varepsilon_{\mathbf{k}'}^2}\right],\end{aligned} \tag{3.83}$$

$$\begin{aligned}\Pi^{-}(q) &= +\frac{g_d}{(2\pi)^2}\int d\mathbf{k}\left[\frac{\widetilde{f}_{\mathbf{k}-}(1+\cos\theta_{kk'})}{\varepsilon_{\mathbf{k}} - \varepsilon_{\mathbf{k}'}} + \frac{\widetilde{f}_{\mathbf{k}-}(1-\cos\theta_{kk'})}{\varepsilon_{\mathbf{k}} + \varepsilon_{\mathbf{k}'}}\right] \\ &= +\frac{2g_d}{(2\pi)^2}\int d\mathbf{k}\left[\frac{\widetilde{f}_{\mathbf{k}-}(\varepsilon_{\mathbf{k}} + \varepsilon_{\mathbf{k}'}\cos\theta_{kk'})}{\varepsilon_{\mathbf{k}}^2 - \varepsilon_{\mathbf{k}'}^2}\right].\end{aligned} \tag{3.84}$$

Since $\theta_{kk'}$ is the angle between the $\mathbf{k}$ and $\mathbf{k}+\mathbf{q}$, it is related to angle between $\mathbf{k}$ and $\mathbf{q}$, ϕ,

$$\mathbf{k}\cdot(\mathbf{k}+\mathbf{q}) = k|\mathbf{k}+\mathbf{q}|\cos\theta_{kk'} = k^2+\mathbf{k}\cdot\mathbf{q} = k^2+kq\cos\phi, \tag{3.85}$$

and

$$\cos\theta_{kk'} = (k+q\cos\phi)/|\mathbf{k}+\mathbf{q}|. \tag{3.86}$$

Substituting the $\cos\theta_{kk'}$ in the integrals, we find

$$\Pi^+(q) = \frac{2g_d}{(2\pi)^2}\frac{1}{\hbar v_F q}\int dk\, d\phi\, k\frac{\widetilde{f}_{\mathbf{k}+}(2k+q\cos\phi)}{q+2k\cos\phi}, \tag{3.87}$$

and

$$\Pi^-(q) = -\frac{2g_d}{(2\pi)^2}\frac{1}{\hbar v_F q}\int dk\, d\phi\, k\frac{\widetilde{f}_{\mathbf{k}-}(2k+q\cos\phi)}{q+2k\cos\phi}. \tag{3.88}$$

The angular integral is

$$\begin{aligned}
\int_0^{2\pi}\frac{2k+q\cos\phi}{q+2k\cos\phi}d\phi &= 2\int_0^{\pi}d\phi\frac{q}{2k}+2\left(\frac{\chi^2}{2k}\right)\int_0^{\pi}d\phi\frac{1}{q+2k\cos\phi} \\
&= 2\frac{\pi q}{2k}+\frac{\chi}{k}\begin{cases} -2\tan^{-1}\left(\frac{\chi\tan(\phi/2)}{q+2k}\right)\Big|_0^{\pi} & q>2k \\ \ln\left(\frac{\chi\tan(\phi/2)+q+2k}{\chi\tan(\phi/2)-q-2k}\right)\Big|_0^{\pi} & q<2k \end{cases} \\
&= \frac{2\pi q}{2k}+\frac{\chi}{k}\begin{cases} -\pi & q>2k \\ \text{non-physical answer} & q<2k, \end{cases}
\end{aligned} \tag{3.89}$$

where $\chi=\sqrt{|4k^2-q^2|}$. Therefore, doing the angular integral, we find

$$\Pi^+(q) = \frac{2g_d}{(2\pi)^2}\frac{\pi}{\hbar v_F}\left\{\int_0^{\infty}dk\widetilde{f}_{\mathbf{k}+}-\int_0^{q/2}dk\widetilde{f}_{\mathbf{k}+}\sqrt{1-(2k/q)^2}\right\}, \tag{3.90}$$

and

$$\Pi^-(q) = \frac{2g_d}{(2\pi)^2}\frac{\pi}{\hbar v_F}\left\{\int_0^{\infty}dk\widetilde{f}_{\mathbf{k}-}-\int_0^{q/2}dk\widetilde{f}_{\mathbf{k}-}\sqrt{1-(2k/q)^2}\right\}. \tag{3.91}$$

Taking the first integral in each expression, we have

$$\Pi^{+}(k) = \frac{g_d}{\pi\beta\left(\hbar v_F\right)^2}\left[\frac{1}{2}\ln\left[2\cosh\left(\beta\mu/2\right)\right] - \frac{k}{2q_t}\int_0^1 du\,\frac{\sqrt{1-u^2}}{1+\mathrm{e}^{uk/q_t-\beta\mu}}\right], \quad (3.92)$$

and

$$\Pi^{-}(k) = \frac{g_d}{\pi\beta\left(\hbar v_F\right)^2}\left[\frac{1}{2}\ln\left[2\cosh\left(\beta\mu/2\right)\right] + \frac{\pi k}{8q_t} - \frac{k}{2q_t}\int_0^1 du\,\frac{\sqrt{1-u^2}}{1+\mathrm{e}^{uk/q_t+\beta\mu}}\right], \quad (3.93)$$

where we have defined a thermal inverse screening length by $q_t = 2/(\beta\hbar v_F)$. The total polarization function is

$$\begin{aligned}\Pi(k) &= \frac{g_d}{\pi\beta\left(\hbar v_F\right)^2}\left\{\ln\left[2\cosh\left(\beta\mu/2\right)\right] + \frac{\pi k}{8q_t}\right. \\ &\left. - \frac{k}{2q_t}\int_0^1 du\,\sqrt{1-u^2}\left(\frac{1}{1+\mathrm{e}^{uk/q_t-\beta\mu}} + \frac{1}{1+\mathrm{e}^{uk/q_t+\beta\mu}}\right)\right\}. \quad (3.94)\end{aligned}$$

Note that μ, which is used in Eq. (3.94), may be obtained from Eq. (2.73) for any given temperature and equilibrium charge carrier density n. In the zero temperature limit, $\mu \to \varepsilon_F$, where $\varepsilon_F = \hbar v_F k_F\,\mathrm{sign}(n)$ is the Fermi energy with $k_F = \sqrt{\pi|n|}$ being the Fermi momentum in graphene with the equilibrium charge carrier density n, so that one obtains

$$\Pi^{+}(k) = \frac{g_d k_F}{2\pi\hbar v_F}\begin{cases} 1 - \frac{k}{8k_F} & k \le 2k_F \\ 1 - \frac{1}{2}\sqrt{1-\frac{4k_F^2}{k^2}} - \frac{k}{4k_F}\sin^{-1}\frac{2k_F}{k} & k > 2k_F, \end{cases} \quad (3.95)$$

and

$$\Pi^{-}(k) = \frac{g_d k}{16\hbar v_F}. \quad (3.96)$$

Hence

$$\Pi(k) = \frac{g_d k_F}{2\pi\hbar v_F}\left\{1 + \left[\frac{k}{4k_F}\arccos\left(2\frac{k_F}{k}\right) - \frac{1}{2}\sqrt{1-\left(2\frac{k_F}{k}\right)^2}\right]H(k-2k_F)\right\}, \quad (3.97)$$

where H is the Heaviside step function. Unlike the LTF case, we see that $\Pi_{\rm RPA}(k) = k/(4\hbar v_F)$ in intrinsic graphene at zero temperature. Since this is also the short wavelength limit of $\Pi_{\rm RPA}(k)$ when $n \neq 0$, one may assert that the RPA result will yield a value for the total potential that is reduced by an approximate factor of $\left[1 + \pi r_s/\left(2\epsilon^0_{\rm bg}\right)\right]^{-1}$, where $r_s \equiv e^2/(\hbar v_F) \approx 2.2$, when compared to the corresponding value from the LTF approach for $k_F\sqrt{r^2+z_0^2} \ll 1$ at zero temperature and zero gap. On the other hand, one may expect that the total potential will exhibit Friedel oscillations for $k_F r \gg 1$ due to non-analyticity of the RPA polarization function (3.97) at $k = 2k_F$, which will be gradually dampened as the temperature increases [43].

3.5 Image Force and Image Potential

Once the integral equation, Eq. (3.26), is solved for the total potential in the plane of graphene, one can use Eq. (3.24) to evaluate the induced charge density in graphene, whose Fourier transform may be used in Eq. (3.21) to yield the total induced potential for any value of z. This may be then used to calculate the nonlinear image force on the external charge from the definition

$$F_{\rm im}(z_0) = -Ze\,\frac{\partial}{\partial z}\Phi_{\rm ind}(\mathbf{r},z)\bigg|_{\mathbf{r}=\mathbf{0},z=z_0}. \tag{3.98}$$

Once the z_0 dependence of the image force is determined, the corresponding image potential may be obtained from the definition $V_{\rm im}(z_0) = \int_{z_0}^{\infty} dz_0'\, F_{\rm im}(z_0')$. While in the nonlinear TF case this integration must be done numerically, in a linear theory one may use instead the usual definition of image potential as a classical self-energy [55], $V_{\rm im}(z_0) = \frac{1}{2}Ze\Phi_{\rm ind}(\mathbf{r}=\mathbf{0}, z=z_0)$, which gives for $z_0 > 0$ [37]

$$V_{\rm im}(z_0) = \frac{1}{2}\,(Ze)^2 \int_0^{\infty} dk\, {\rm e}^{-2kz_0}\left[\frac{1}{\epsilon_{\rm bg}(k) + v_C(k)\Pi(k)} - 1\right]. \tag{3.99}$$

By using the LTF model, where $v_C(k)\Pi_{\rm TF} = q_s/k$, one obtains in the zero-gap case

$$V_{\rm im}(z_0) = \frac{(Ze)^2}{4z_0\epsilon^0_{\rm bg}}\left[1 - \epsilon^0_{\rm bg} - 2\zeta\, {\rm e}^{2\zeta}\, {\rm E}_1\left(2\zeta\right)\right], \tag{3.100}$$

where $\zeta \equiv q_s z_0/\epsilon^0_{\rm bg}$. It is worthwhile mentioning that this expression gives asymptotically $V_{\rm im} \sim -\left(Ze\right)^2\left[1/\left(4z_0\right) - 1/\left(8q_s z_0^2\right)\right]$, for a heavily doped graphene and/or sufficiently large distance, such that $q_s z_0 \gg 1$. On the other hand, in the opposite limit, $q_s z_0 \ll 1$, one finds to the leading order $V_{\rm im} \sim \left(Ze\right)^2\left(1/\epsilon^0_{\rm bg} - 1\right)/\left(4z_0\right)$, as if graphene were totally absent. When the RPA polarization function at zero temperature, Eq. (3.97), is used in Eq. (3.98) in the zero-gap case, one can show that similar limiting forms of the image potential exist, except that the effective background dielectric constant, $\epsilon^0_{\rm bg}$, is to be replaced by $\epsilon^0_{\rm bg} + \pi r_s/2 \approx \epsilon^0_{\rm bg} + 3.44$ when $k_F z_0 \ll 1$ [37].

Chapter 4

Numerical Method

4.1 One-dimensional Nonlinear Integral Equation

As we discussed, the total electric potential in the system at the surface of graphene is given by Eq. (3.26). In this chapter we explain the numerical method we used to solve the nonlinear integral equation. Based on the symmetry of the system it is evident that the potential is a function of magnitude of $\mathbf{r}$ ($|\mathbf{r}| = r$) only:

$$\begin{aligned}\phi(r) = \phi_0(r) \quad - \quad & e\int_0^\infty dr' r' n_{ind}(r') \left[\int_0^{2\pi} \frac{d\vartheta}{\sqrt{r^2 + r'^2 - 2rr'\cos\vartheta}}\right. \\ & \left. -\frac{\epsilon_s - 1}{\epsilon_s + 1}\int_0^{2\pi} \frac{d\vartheta}{\sqrt{r^2 + r'^2 + 4h^2 - 2rr'\cos\vartheta}}\right], \end{aligned} \tag{4.1}$$

where $\phi_0(r)$ is given by Eq. (3.27) and $n_{ind}(r') = n\left(\mu + e\phi(r')\right) - n\left(\mu\right)$. One may perform the angular integral

$$\begin{aligned}\int_0^{2\pi} \frac{d\vartheta}{\sqrt{r^2 + r'^2 - 2rr'\cos\vartheta}} &= 2\int_0^{\pi} \frac{d\vartheta}{\sqrt{r^2 + r'^2 - 2rr'\cos\vartheta}} \\ &= 4\int_0^{\frac{\pi}{2}} \frac{d\varphi}{(r+r')\sqrt{1 - \frac{4rr'}{(r+r')^2}\sin^2\varphi}} \\ &= \frac{4}{(r+r')} K\left(\frac{2\sqrt{rr'}}{r+r'}\right), \end{aligned} \tag{4.2}$$

where $\varphi = \frac{1}{2}\left(\pi - \vartheta\right)$, and $K(x)$ is the complete elliptic integral of the first kind

$$K(x) = \int_0^{\frac{\pi}{2}} \frac{d\varphi}{\sqrt{1 - x^2\sin^2\varphi}}. \tag{4.3}$$

In the same way

$$\int_0^{2\pi} \frac{d\vartheta}{\sqrt{r^2 + r'^2 + 4h^2 - 2rr'\cos\vartheta}} = \frac{4}{\sqrt{(r+r')^2 + 4h^2}} K\left(\frac{2\sqrt{rr'}}{\sqrt{(r+r')^2 + 4h^2}}\right). \tag{4.4}$$

Therefore the nonlinear integral Eq. (4.1) reduces to

$$\begin{aligned}\phi(r) = \phi_0(r) \quad - \quad & e\int_0^\infty dr' r' n_{ind}(r') \left[\frac{4}{(r+r')} K\left(\frac{2\sqrt{rr'}}{r+r'}\right)\right. \\ & \left. -\frac{\epsilon_s - 1}{\epsilon_s + 1}\frac{4}{\sqrt{(r+r')^2 + 4h^2}} K\left(\frac{2\sqrt{rr'}}{\sqrt{(r+r')^2 + 4h^2}}\right)\right]. \end{aligned} \tag{4.5}$$

There are two important issues here, and they are as follows:

- The integrand is singular at the point $r' = r$, i.e., $K\left(\frac{2\sqrt{rr'}}{r+r'}\right)\Big|_{r=r'} = K(1) = \infty$. The singularity is the consequence of the fact that we include the electrical self-energy of the elements of the surface. More explicitly, in the angular integral, when $r = r'$ for the first element of angle ϑ we include the self-energy of it which causes the infinity. (see Fig. 4.1). We explain how to avoid the singularity in the integral in the next section.

- The upper limit of the integral is infinity, but, in numerical calculations we must define a cut-off for the upper limit. Although, when $r \to \infty$ then $\phi(r) \to 0$, but the electrical interaction is a long-range interaction, and the upper limit must be sufficiently large in order to get convergent numerical solutions.

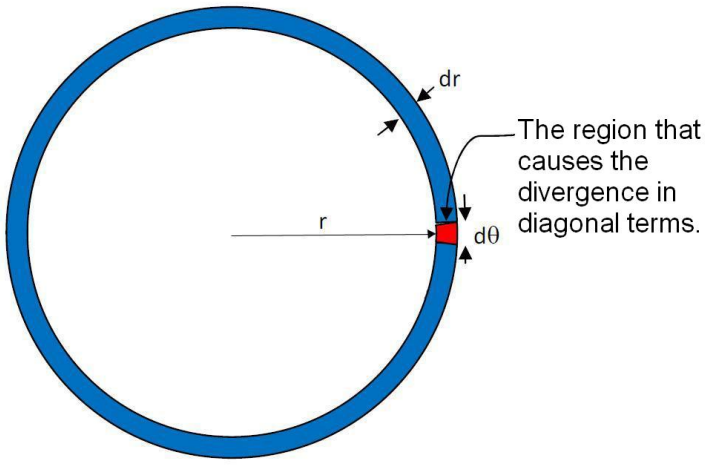

Figure 4.1: Schematic view of the element of elliptic integral and the angular element that causes the singularity.

Before explaining the details of solving these issues, we go through the details of the numerical steps.

4.2 Numerical Steps

The steps in the coding are as follows:

1. Input parameters:

    - Z, the external charge, we usually put $Z = 1$.
    - z_0, the distance of charge away from graphene.
    - h, the gap between graphene and substrate; $h = 0$ is usually used in the literature. Non-zero h represent a physical situation and the limit $h \to \infty$ represents free graphene.
    - ϵ_s, the dielectric constant of the substrate. We usually assume that the substrate is SiO_2 with $\epsilon_s = 3.9$. The other way of representing free graphene is to put $\epsilon_s = 1$.
    - T, the temperature.
    - N, number of points we use in the scheme to solve the discretized integral equation.
    - n_0, the areal density of charge carriers in the unperturbed graphene. As it is discussed in chapter 2, n_0 is determined by a gate potential. The corresponding chemical potential, μ, is determined for the given n_0. We come back to the details of calculating μ from a given n_0 later.

2. Constant parameters:

- $a \approx 1.42\,\text{Å}$, The carbon-carbon distance in graphene lattice.
- $t \approx 3.08$ eV, the nearest neighbor hopping energy and consequently, $\hbar v_F = \frac{3}{2}at \approx 6.56\,\text{eVÅ}$.
- $t' = 0$, the second nearest neighbor hopping energy.

3. Determining the chemical potential, μ, related to given input parameters: the local density of electrons is related to the equilibrium chemical potential and the local electrical potential via Eq. (2.84). One may use Eq. (2.72) in order to find the chemical potential μ, corresponding to given n_0 and T. Once we use one specific equation to find μ from a given n_0, we confine ourselves to use the same expression to find the local density of electrons in the presence of an electric field due to external charge in the entire coding. However, the expression mentioned above is the most accurate expression when we use the density of electrons, $\rho(\varepsilon)$, given by Eq. (2.66), but it takes a long time to solve the equation. Therefore, depending on the case in each calculation, we may use and compare one of the following approximate methods:

   - Case $T = 0$: We saw that at zero temperature the density of electrons reduces to Eq. (2.76). Using the series expansion of the density of states, we found an accurate approximation Eq. (2.77) for the density of electrons. We discuss the accuracy of considering the whole integral, the series expansion, and the result of keeping only the first term of the expansion.
   - Case $T > 0$ and low doping levels: for sufficiently low doping levels such that only low energy states in the energy spectrum may be occupied, one may use the linearized density of states, leading to the dilog function Eq. (2.73) for the density of electrons. However, using the dilog

function in coding makes the computing slow, therefore one may use the approximate expression Eq. (2.75) instead of the dilog function.

- Case $T > 0$ and large doping levels: since the effect of temperature in this case appears at the tail of the screening potential, we consider the summation of the two approximations mentioned above, i.e., Eq. (2.81), as the suitable approximation in computation. We show that this approximation works well.

4. Changing the variable in the integral: we change the variable such that the interval, $[0, \infty)$ changes to [0,1]:

$$\int_0^\infty dr F(r) \Rightarrow \int_0^1 dx \widetilde{F}(x). \tag{4.6}$$

We discuss more details in the next section.

5. Converting the integral into a summation, i.e., converting the nonlinear integral equation into a nonlinear matrix equation: we replace the integral by a summation:

$$\int_0^1 dx \widetilde{F}(x) \Rightarrow \sum_{i=0}^{N} \Delta x_i \widetilde{F}(\overline{x}_i), \tag{4.7}$$

where $\Delta x_i = x_{i+1} - x_i$, $\overline{x}_i = \frac{1}{2}(x_{i+1} + x_i)$, $x_0 = 0$ and $x_{N+1} = 1$. We discuss more details in the next section.

6. Solving the nonlinear matrix equation to find the total electric potential in the surface of graphene: we use the fsolve routine in MATLAB. The result may be used to compute the other quantities, e.g., image potential, density of induced charge and conductivity.

7. Using the solution to determine the induced charge density in the surface of graphene, image force and image potential, conductivity, etc.

4.3 Partitioning the Integral

As we mentioned before, we need to partition the integral equation, i.e., convert it to a matrix equation. Eq. (4.5) involves an infinite upper bound, i.e., $r \in [0, \infty)$; but we must have a cut-off on the upper bound in numerical computations of the integral. Since the electric interaction is long-range, the upper bound cut-off has to be sufficiently large compared to other distance parameters in the system. Because the potential reaches its maximum around the origin, and drops to zero for large r, and because it will be a slowly varying function at large r, one may think of defining a new variable x as:

$$x = \frac{r}{r + |z_0|} \Leftrightarrow r = |z_0| \frac{x}{1 - x}, \tag{4.8}$$

where $x \in [0, 1]$. Then

$$\int_0^\infty dr F(r) \Rightarrow \int_0^1 dx \widetilde{F}(x). \tag{4.9}$$

We apply the trapezoid rule in order to convert the integral to a summation. We partition the interval $[0, 1]$ into N equal spaces. If x_i denotes a middle point of partition i, then

$$\int_0^1 dx \widetilde{F}(x) \approx \sum_{i=1}^{N} \Delta x \widetilde{F}(x_i) \tag{4.10}$$

where $\Delta x = x_{i+1} - x_i = x_2 - x_1$. By substituting the new variable in the integral Eq. (4.5), we end up with a nonlinear matrix equation of the form

$$U_{N\times 1} = U^0_{N\times 1} - \Xi_{N\times N} \times n^{ind}_{N\times 1}\left(U_{N\times 1}\right), \tag{4.11}$$

where $\Xi_{N\times N}$ is the matrix kernel of the integral and $n^{ind}_{N\times 1}$ is the vector of density of charge carriers. We should mention that we also tried the Simpson's rule which

approximate the integrant by a parabola and it is supposed to be more accurate compared to trapezoid rule which approximate the integrant by a straight line. The Simpson's rule led to very small corrections to the trapezoid rule, therefore we confined ourselves to trapezoid rule.

4.4 Diagonal Terms

Because the elliptic integral in Eq. (4.5) is singular at $r = r'$, the kernel matrix Ξ is singular at diagonal terms; i.e.,

$$K\left(\frac{2\sqrt{rr'}}{r+r'}\right)\Bigg|_{r=r'} \Rightarrow K\left(2\frac{\sqrt{xy(1-x)(1-y)}}{x(1-y)+y(1-x)}\right)\Bigg|_{x=y} \rightarrow \infty. \tag{4.12}$$

which is singular when $x = y$. The singularity is a direct consequence of including the electrostatic self-energy of a small element of area, when we calculate the angular integral at the points $r = r'$ $(x = y)$. In order to compute the integral numerically we must find a way to eliminate the singularity of the diagonal terms.

Choosing appropriately normalized diagonal terms leads to faster convergence into the "real" solution. One may expect the following results/benefits from an appropriate method:

1. A zero slope of potential, $U(r)$, at $r = 0$. The radial component of electric field is zero at $r = 0$, by symmetry; therefore, the tangent of the potential curve must be horizontal at $r = 0$.

2. The solution by the best method should converge to final results faster than other methods; in other words, by increasing the number of points in the summation there should be the least change in the result comparing to the other methods.

3. The results of the other methods should converge to the result of the best method as the number of points in the computations is increased.

However, the most important outcome of checking different methods, is the test of the trustworthiness of the computation. From physical and mathematical points of view, one may expect very small changes in the solution due to different normalizing the diagonal points, particularly for large numbers of calculation points. But from the numerical point of view, it is a test that the solution must not change dramatically on changing the diagonal terms in a reasonable way. As we see in the following discussion, our numerical solution satisfies our expectation. We went through several different mathematical and physical methods, and eventually found a method that works very well even for very small numbers of points, such as 400. Since the singularity is due to the terms related to response of graphene to an external potential, and the substrate does not contribute to the singularity, for simplicity in the following comparison, we consider only the problem of free graphene at zero temperature, and compare the results of different methods in only that case.

Some of the methods we considered are as follows:

1. Setting the diagonal terms to zero. This naive approach is to ignore the singularity and set the diagonal terms to zero, i.e., $K(x,y)|_{x=y} = 0$. However, it is clear that by this method we ignore the interaction of the different elements of a ring, and it is not a suitable method. It is expected that by increasing the number of points of partitioning the integral, the solution converges to the "real" solution. This is because the larger the number of points we use, the narrower ring we get and therefore the smaller contribution of the self-energy of rings. Also, because of the scheme we chose, a larger number of points leads to larger cut-off in the upper bound of the integral. Results show large

gaps between neighboring solutions using different numbers of points by this method. The largest number we chose is 2400, which is imposed by the constraint of the size of the matrix that MATLAB can handle in computation. The other point is that the slope at $r = 0$ is not zero, and the curve heads down around the origin. Zero diagonal terms, especially at the first terms, are responsible for the "downturn" in $U(r)$ as $r = 0$ is approached from positive r. That is a consequence of the fact that the contribution of well-normalized self energy to the total interaction is bigger, respectively, for the first few points than for the middle points. This is because the first few rings interact only with next rings, but, in the middle, each ring interacts with rings from both smaller and bigger radiuses.

2. The best method we found is to replace the diagonal term with a guessed self energy of the ring which depends on the radius. Using this idea and several attempts, we end up with a method that shows good accuracy, in the sense that the solution shows very small changes when we increase the number of points in computing. On the other hand, using this method, the fsolve routine needs less iterative steps to find the solution compared to the first method. For example, for 800 points, the first method takes 15 iterative steps, while this method just takes 7 steps. A comparison between these two method is shown in Fig. 4.2.

4.5 Other Tests of the Code

- We substitute the solution into the density of electrons and verified that its spatial integral yields $-Ze$. The numerical solution we perform gives typically

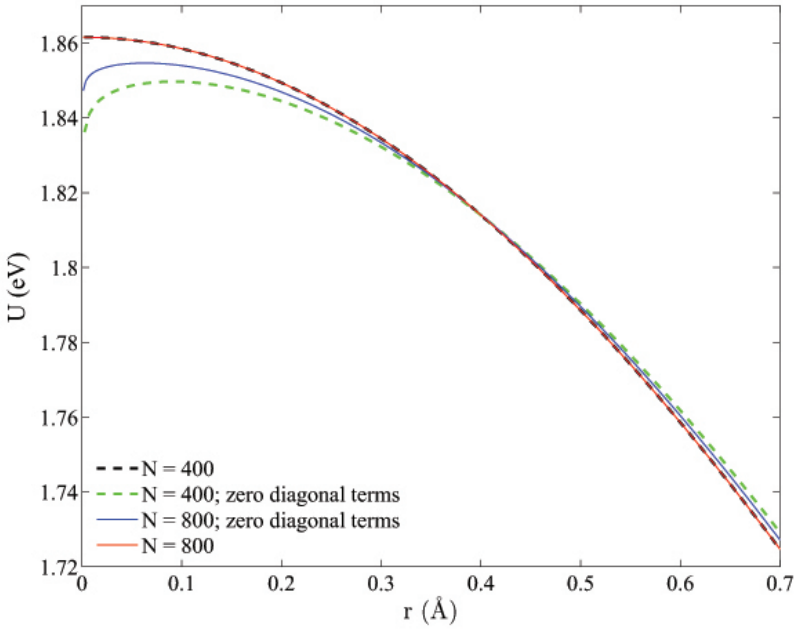

Figure 4.2: Comparison of the two methods of considering diagonal terms. While the guessed diagonal terms we found show good accuracy such that the result of computing with 400 and 800 points (dashed [black] line and solid [red] line, respectively) are eventually on top of each other, the result of eliminating diagonal terms shows less accuracy and a "head-down" near origin.

$\sim -0.99Ze$ for this case, indicating that all is well.

- The result for the case free graphene, $\epsilon_s = 1$ is close to the result for the case with a very large gap.

- The result of solving the integral equation when we substitute the linear approximation of the density of electrons (matrix $n^{ind}_{N\times 1}$) is well matched with the inverse Fourier transform of Eq. (3.31).

Chapter 5

Results

We first analyze in Fig. 5.1 the effects of doping with different gap values for graphene at zero temperature with a charge in close proximity to graphene by comparing the nonlinear TF model with the two linear models. This is followed by a discussion of temperature effects in Figs. 5.2, 5.4, and 5.4 for the nonlinear TF and the RPA models when charge is separated further away from graphene. We discuss in more detail the RPA model in Figs. 5.5, 5.6, and 5.7. The effects of temperature and charge separation on nonlinear screening are summarized and discussed in Fig. 5.8. Errors due to using the linearized DOS and neglecting the exchange and correlation effects are estimated in Fig. 5.9 for intrinsic graphene at zero temperature. Finally, effects of nonlinear screening on both the image force and image potential are discussed in Figs. 5.10 and 5.11, respectively. In Fig. 5.12 we show the image force as a function of position of the charge.

5.1 Comparison of Models for a Charge Close to Graphene

We first consider the case of a positive charge with $Z = 1$ a distance 2 Å above graphene lying on an SiO_2 substrate ($\epsilon_s = 3.9$) with several gap heights h, several equilibrium charge carrier densities n, and zero temperature. This situation may be representative of a Li atom adsorbed on top of supported graphene, where the effective charge transfer is found to be around $Z = 0.9$, whereas the local DOS exhibits a resonant feature at about 0.9 eV above the neutrality point of graphene's π electron band due to hybridization with lithium's $2s$ orbital [32]. Besides undoped graphene with $n = 0$, which was studied previously [24, 25, 26], we also analyze the cases of both electron ($n > 0$) and hole ($n < 0$) doping of graphene by a gate

potential, making sure that the Fermi level stays well below any chemisorption resonances in graphene's DOS ($n \lesssim 10^{13}$ cm^{-2} for Li [32]).

In Fig. 5.1 we show in the left column (1) the results for the potential energy $U(r) = e\phi(r)$, with $\phi(r)$ obtained from the nonlinear TF equation Eq. (3.26) at zero temperature for $n = 0$ (the upper thick solid line), $\pm 10^{12}$ (thin solid and dashed lines, respectively), and $\pm 10^{13}$ cm^{-2} (the lower thick solid and thick dashed lines, respectively), and with $h = 0$ (panels a), 1 Å (panels b), and ∞ (i.e., free graphene, panels c). For the purpose of comparison, we also show in the right column (2) of Fig. 5.1 the corresponding results obtained from both the LTF (dash-dotted lines) and the RPA (dotted lines) models (with the line thicknesses matching those in the left column), with $\phi(r)$ calculated from Eq. (3.31) using the appropriate polarization functions at zero temperature. [As a reference, note that, for free graphene, the LTF result with $n = 0$ actually shows the value of the unscreened potential in the plane of graphene, $U_0(r) = e\phi_0(r)$ with $\phi_0(r)$ given in Eq. (3.27), whereas the corresponding RPA result shows that same potential reduced by the dielectric constant of intrinsic graphene, $1 + \pi r_s/2 \approx 4.44$.] We see in Fig. 5.1 that the main effects on the potential come from increasing the doping density $|n|$. While all models exhibit strong variation with n at large distances r, we notice that both the nonlinear TF and the RPA results are surprisingly concentrated in a relatively narrow range of values for the potential at short distances for all densities n. This seems to corroborate conclusions from a DFT study that the induced density variations in graphene seem to saturate with increasing level of doping [29].

While the LTF model appears to be a rather poor approximation to the nonlinear TF results at short distances r, their agreement improves at large distances with increasing density $|n|$, as expected. Most strikingly, the RPA model gives a

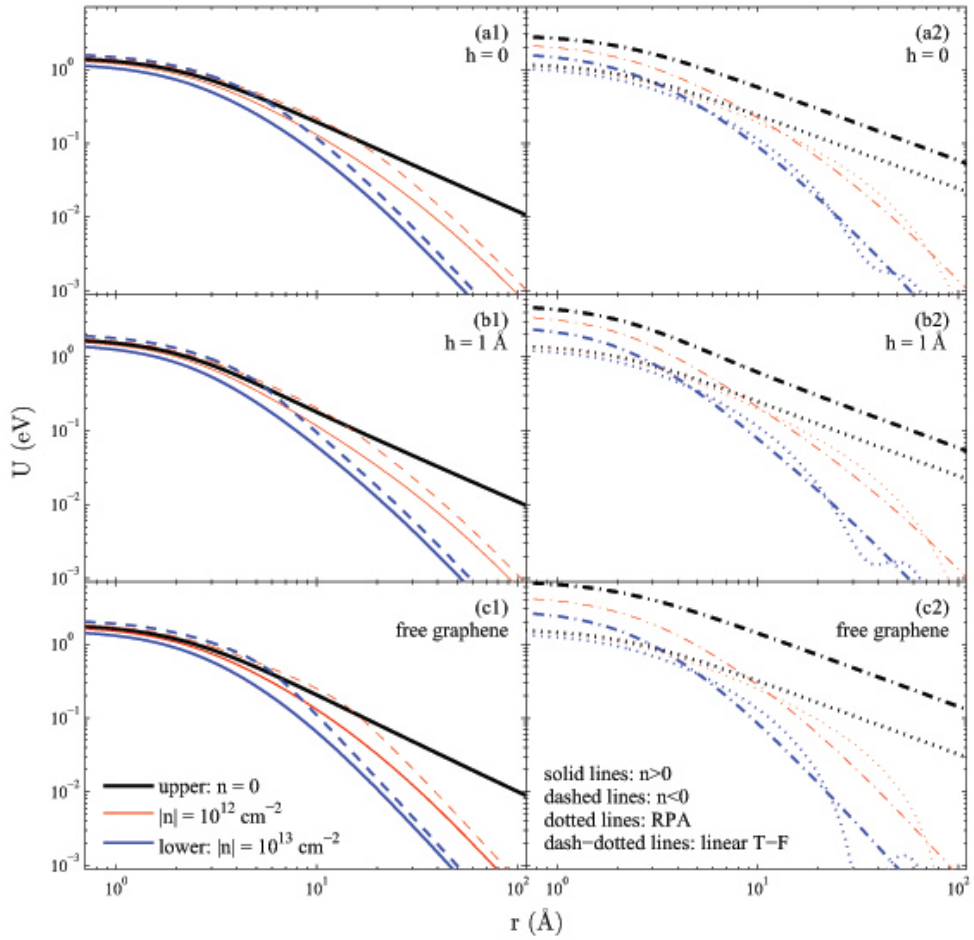

Figure 5.1: The potential energy, $U(r) = e\phi(r)$ (in eV), due to an external proton at distance $z_0 = 2$ Å above graphene at zero temperature, as a function of the radial distance r (in Å) in the plane of graphene lying on an SiO_2 substrate with the gap heights $h = 0$ (panels a), 1 Å (panels b), and ∞ (free graphene, panels c). Results from the nonlinear TF model are shown in column 1 for equilibrium densities $n = 0$ (upper thick [black] solid line), $\pm 10^{12}$ (thin [red] solid and dashed lines, respectively), and $\pm 10^{13}$ cm^{-2} (lower thick [blue] solid and dashed lines, respectively). Results from the linearized TF model and the RPA model are shown, respectively, by dash-dotted and dotted lines in column 2 for densities $|n| = 0$ (upper thick [black] lines), 10^{12} (thin [red] lines), and 10^{13} cm^{-2} (lower thick [blue] lines).

surprisingly good approximation to the nonlinear TF results at short distances for all densities n, while exhibiting Friedel oscillations around the LTF results at large distances for $n \neq 0$, with wavelengths that clearly scale with k_F^{-1} [43]. However, for $n = 0$, one sees an increasing disagreement between the nonlinear TF and the RPA models with increasing distance, which may be attributed to a poor performance of the TF model in intrinsic graphene for induced charge carrier densities below 10^{11} cm^{-2}, as suggested recently by Brey and Fertig [45]. On the other hand, the TF model presumably gives a correct order of magnitude for nonlinear effects, if any, when the doping density $|n|$ increases, which are best seen by analyzing the effect of changing the sign of n (or equivalently, the sign of Z), because linear models are insensitive to this sign. In that respect, one can clearly notice in the left column of Fig. 5.1 differences between the potentials $U_+(r)$ for $n > 0$ and $U_-(r)$ for $n < 0$ in the nonlinear TF model, which are further discussed in Fig. 5.8 below.

Finally, one notices in Fig. 5.1 that, while the presence of a non-zero gap between graphene and substrate does not affect the qualitative behavior of the results, its quantitative effects may not be neglected in the values of the potential for all densities shown. While this is particularly clear at short distances for the nonlinear TF results, it is also interesting to see how Friedel oscillations in the RPA model increase in amplitude with increasing gap. In fact, we have found that the RPA potential may even change its sign at large distances r for free graphene with large enough $|n|$ [see Fig. 5.5]. Given that the size of gap is a poorly defined parameter, with a plausible value of around $h = 1$ Å [32, 58], one should be aware of its role in the total potential in graphene due to external charges.

5.2 Effects of Temperature

We next consider in Fig. 5.2 graphene on an SiO_2 substrate with the gap $h = 1$ Å, both at zero (panels a and b) and room ($T = 300$ K, panels c and d) temperatures, with a charge $Z = 1$ placed at larger distances of $z_0 = \pm 10$ Å away from graphene. With $z_0 = 10$ Å (panels a and c) we can represent a distant charge above graphene, such as a slowly moving ion [37], or an electron in an image-potential state [36], whereas the case $z_0 = -10$ Å (panels b and d) represents a technologically relevant case of a charged impurity trapped deep in the SiO_2 substrate [30, 31]. We compare the nonlinear TF results with those from the RPA model for $|n| = 0$, 10^{12}, and 10^{13} cm^{-2}, shown with the same line styles and thicknesses as in Fig. 5.1. While the RPA results seem to be quite close, apart from the Friedel oscillations, to those of the nonlinear TF model for $n > 0$, the agreement between those two models seems to have worsened at short distances for $n = 0$ when compared to Fig. 5.1, which may have to do with the problematic performance of the nonlinear TF model in intrinsic graphene exposed to weak perturbations, as mentioned previously [45].

On the other hand, one notices in Fig. 5.2 a much greater spread in the relative magnitudes of the potential at short distances than in Fig. 5.1. This is partly due to the effect of doping in the presence of a much weaker external perturbation in Fig. 5.2 than in Fig. 5.1, so that the induced density variations involved in the results in Fig. 5.2 have not reached the effect of saturation mentioned in Ref.[29] Another cause for a larger spread of the potential at short distances in Fig. 5.2 comes from the nonlinear effects, which are further discussed in Fig. 5.8.

As regards the effect of non-zero temperature, one notices that its main role is to dampen the potential in intrinsic graphene at distances $r \gtrsim 10$ Å, both in the nonlinear TF and the RPA cases. This may be explained by assessing the TF

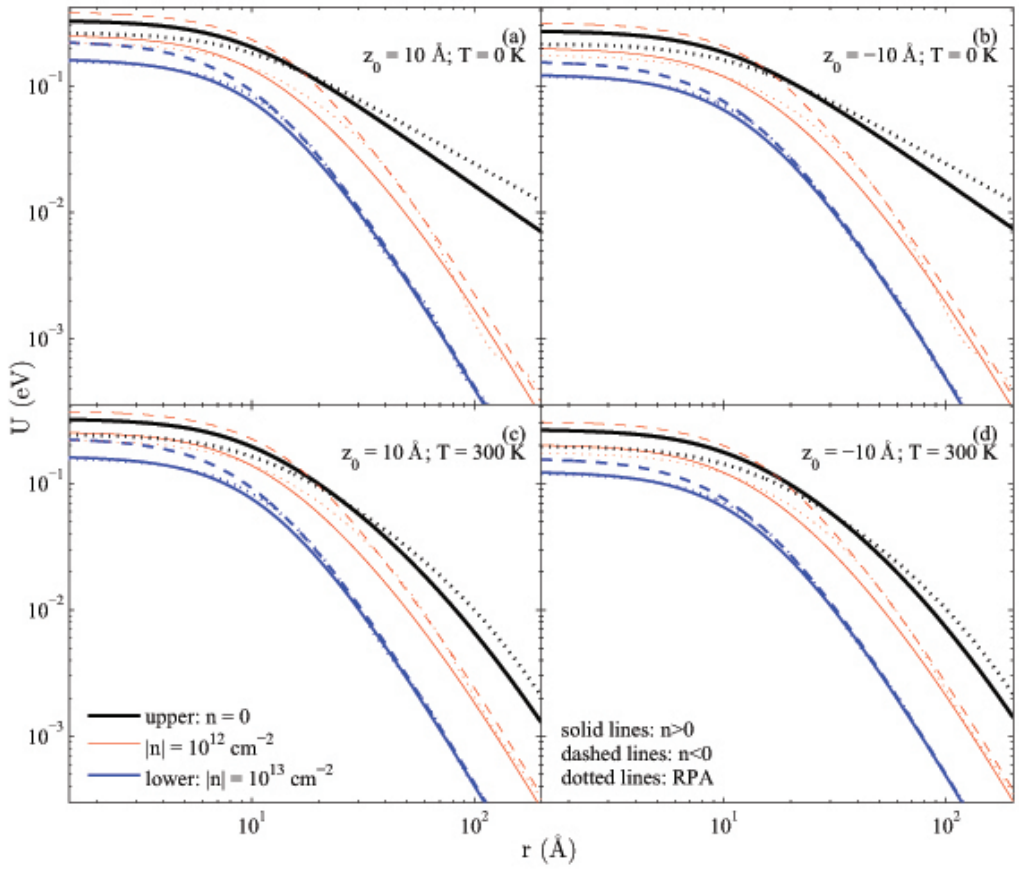

Figure 5.2: The potential energy, $U(r) = e\phi(r)$ (in eV), due to an external proton at distances $z_0 = \pm 10$ Å (left and right columns, respectively) from graphene at $T = 0$ (top row) and $T = 300$ K (bottom row), as a function of the radial distance r (in Å) in the plane of graphene lying on an SiO_2 substrate with the gap height $h = 1$ Å. Results from the nonlinear TF model are shown for equilibrium densities $n = 0$ (upper thick [black] solid line), $\pm 10^{12}$ (thin [red] solid and dashed lines, respectively), and $\pm 10^{13}$ cm^{-2} (lower thick [blue] solid and dashed lines, respectively). Results from the RPA model are shown by dotted lines for densities $|n| = 0$ (upper thick [black] line), 10^{12} (thin [red] line), and 10^{13} cm^{-2} (lower thick [blue] line).

inverse screening length in Eq. (3.36) in the zero density and the zero temperature limits, giving $q_s \to 4r_s q_t \ln 2$ and $q_s \to 4r_s k_F$, respectively. Therefore, one may conclude that screening of the potential at large distances due to a non-zero temperature will prevail only for low enough charge-carrier densities, such that $|n| < \left[2 \ln 2 k_B T / (\hbar v_F)\right]^2 / \pi \approx 10^{11}$ cm^{-2} at room temperatures. We have checked that nonlinear TF results for $|n| = 10^{11}$ cm^{-2} at zero temperature as shown in Fig. 5.3 are quite close to the result for intrinsic graphene at room temperature. The effects of temperature on the nonlinearity of the potential is further discussed in Fig. 5.8. On the other hand, while the Friedel oscillations are still visible in Fig. 5.2 in the RPA results for zero temperature at large distances r for $n \neq 0$, they seem to be reduced in relative amplitude by the increased distance $|z_0|$ when compared to the oscillations seen in Fig. 5.1, and we see that the increased temperature dampens the Friedel oscillations in Fig. 5.2, as expected.

We finally note that, by analyzing the asymmetry in the results with respect to the change in sign of z_0 in Fig. 5.2, we again emphasize the role of a non-zero gap, because all results would be independent of that sign in the zero gap case. It is remarkable that a gap of only $h = 1$ Å affects, not only the values of the potential at short distances, but also the magnitudes of the asymmetry in the nonlinear TF results with respect to the sign of $n \neq 0$ at short distances.

We continue by considering the case of a positive charge with $Z = 1$ a distance 2 Å away from graphene, lying on an SiO_2 substrate with $\epsilon_s = 3.9$ and the gap height of $h = 4$ Å [38]. Again, the case with $z_0 = 2$ Å represents, e.g., an alkali-metal atom adsorbed on graphene [24, 32], whereas the case $z_0 = -2$ Å may represent an alkali-metal atom intercalated in the middle of the gap between the graphene and the substrate [34]. Note that results for an external charge of the opposite sign could be recovered by simply changing the sign of n. In Fig. 5.4 we show the results for the

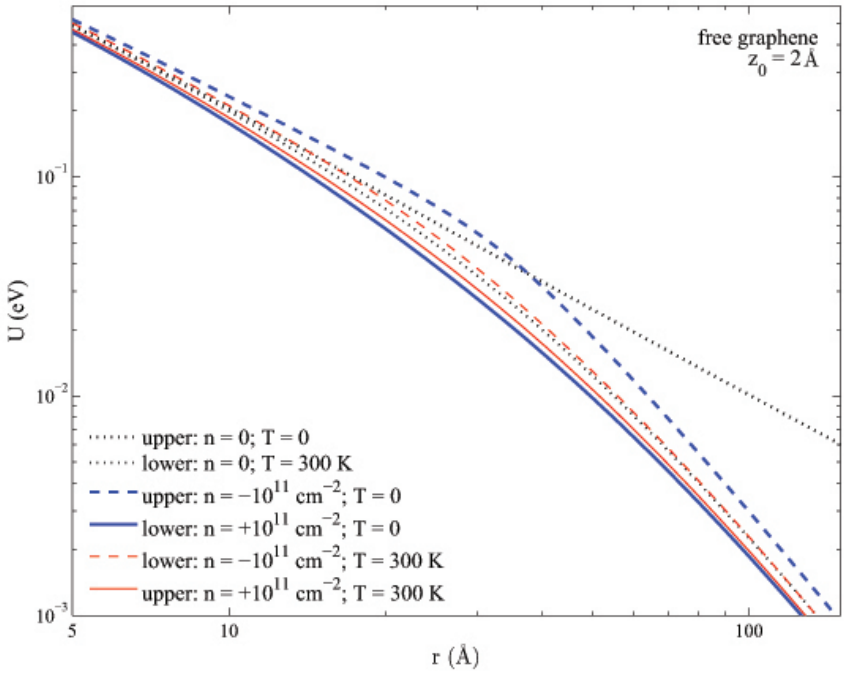

Figure 5.3: The potential energy (in eV), due to an external proton at distance $z_0 = 2$ Å from free graphene at $T = 0$ (thick lines) and $T = 300$ K (thin lines), as a function of radial distance r (in Å) in the plane of graphene. Result from the nonlinear TF model are shown for equilibrium densities $n = 0$ (dotted lines), $+10^{11}$ cm^{-2} (solid lines) and -10^{11} cm^{-2} (dashed lines).

potential energy $U(r) = e\phi(r)$, with $\phi(r)$ obtained from the non-linear TF equation Eq. (3.26) for both at $T = 0$ (panel a and b) and room ($T = 300$ K, panel c and d) temperatures, for $|n| = 0$, 10^{12} and 10^{13} cm^{-2}. We also show the corresponding results obtained from the RPA model , shown in the same line styles and thicknesses as in Fig. 5.1. The asymmetry in the corresponding potential energy in electron ($n > 0$) and hole ($n < 0$) doped graphene, seen in Figs. 5.1 and 5.2, is clear in Fig. 5.4 also; most strikingly, in the case that a proton is intercalated in the middle of

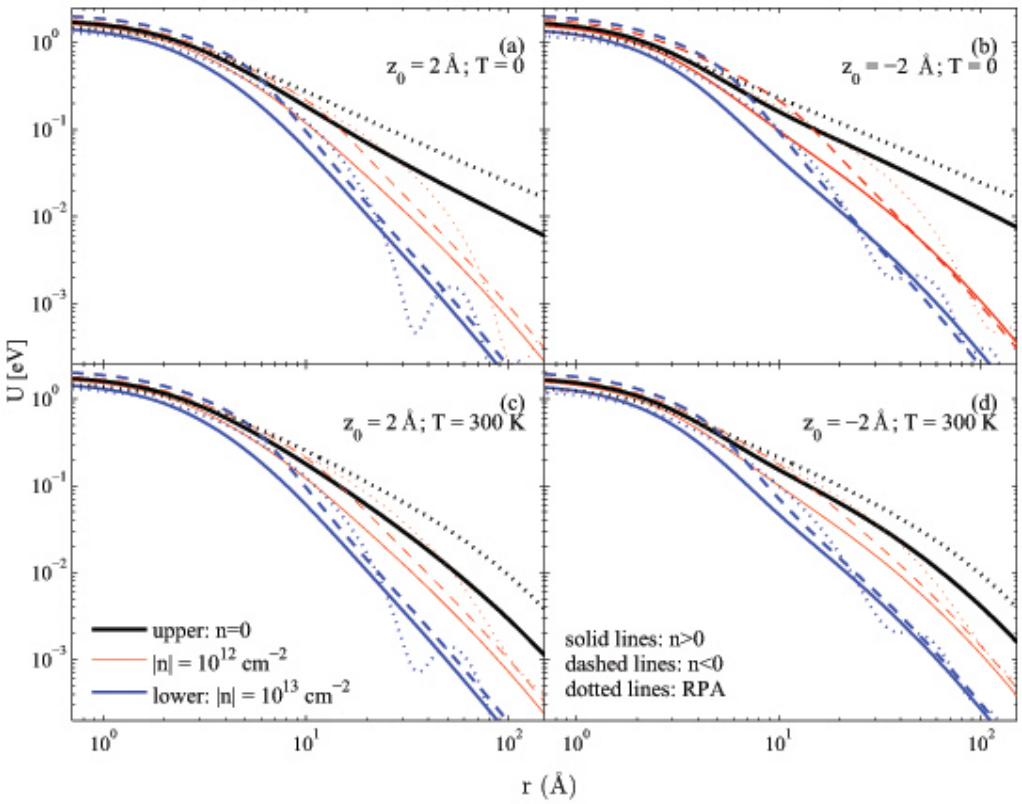

Figure 5.4: The potential energy, $U(r) = e\phi(r)$ (in eV), due to an external proton at distances $z_0 = \pm 2$ Å (left and right columns, respectively) from graphene at $T = 0$ (top row) and $T = 300$ K (bottom row), as a function of the radial distance r (in Å) in the plane of graphene lying on an SiO_2 substrate with the gap height $h = 4$ Å. Results from the nonlinear TF model are shown for equilibrium densities $n = 0$ (upper thick [black] solid line), $\pm 10^{12}$ (thin [red] solid and dashed lines, respectively), and $\pm 10^{13}$ cm^{-2} (lower thick [blue] solid and dashed lines, respectively). Results from the RPA model are shown by dotted lines for densities $|n| = 0$ (upper thick [black] line), 10^{12} (thin [red] line), and 10^{13} cm^{-2} (lower thick [blue] line).

the gap between the graphene and the substrate, the potential energies of $n > 0$ and $n < 0$ cross. As regards the effects of the sign of z_0, there are only small variations in the shapes of curves for nonlinear potential at intermediate distances, indicating that the proximity of the substrate has negligible effect at such a short distance from graphene as $|z_0| = 2$ Å. However, it shows more changes compared to Figs. 5.1 and 5.2. Specially, it seems that the opposite induced charge on the surface of the substrate in the case $z_0 = -2$ Å (which is stronger than the case $z_0 = 2$ Å), causes the "wiggling" in the potential energy around radial distances $r = 10$ Å . The non-zero temperature in Fig. 5.4 mostly affects the results for intrinsic graphene ($n = 0$), as is expected at room temperature.

5.3 Details of the RPA

In order to find a better view of Friedel oscillations, a close-up of the result of RPA and LTF shown in Fig. 5.1, is reploted in Fig. 5.5. In panel (a), the result for equilibrium density $|n| = 10^{12}$ cm^{-2} is shown for the case $h = 0$ (thin [black] lines) and free graphene (thick [colorful] lines). RPA and LTF results are shown by solid lines and dashed lines, respectively. In panel (b), the results for equilibrium density $|n| = 10^{13}$ cm^{-2} are shown, with the same line style as panel (a). Interestingly, Friedel oscillations are strong enough to change the sign of the potential for intermediate distances several times. The positions of peaks of the oscillations are almost independent of the presence of the substrate, but the magnitudes of the oscillations depend strongly on it, such that, in the presence of the substrate, the sign changes do not occur. To illustrate the magnitude and the wavelength of Friedel oscillations, we plot the ratio of the RPA and LTF potentials, in Fig. 5.6 for equilibrium charge carrier densities $|n| = 10^{12}$ and $|n| = 10^{13}$ cm^{-2} (solid [red] line

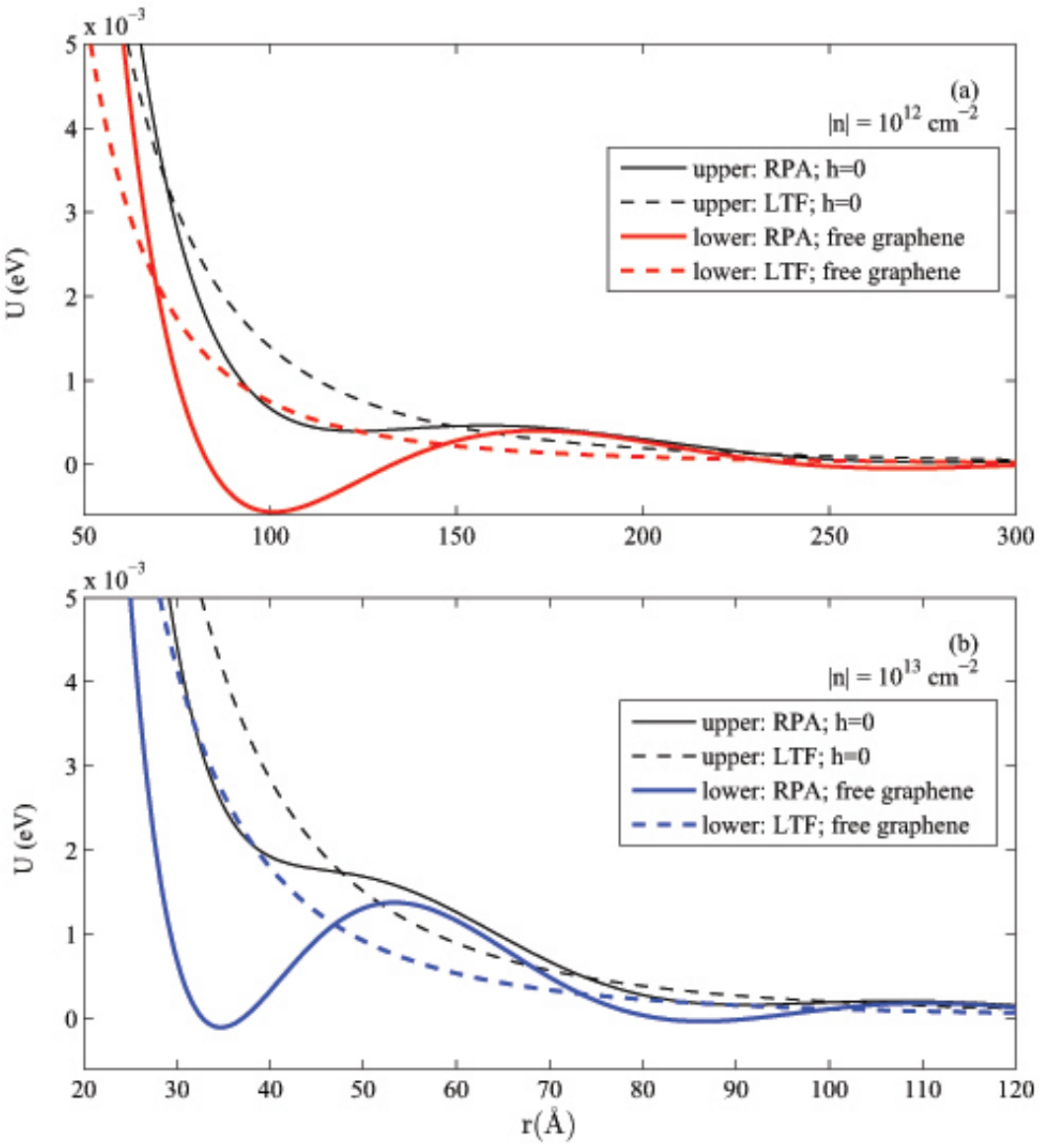

Figure 5.5: Close-up of the potential energy (in eV), from RPA model (solid lines) and PTF model (dashed lines), due to an external proton at distance $z_0 = 2$ Å from graphene at $T = 0$, as a function of radial distance r (in Å) in the plane of graphene lying on an SiO_2 substrate with the gap heights $h = 0$ (upper thin [black] lines) and ∞ (free graphene, lower thick [colorful] lines). Result from the RPA and LTF models are shown for equilibrium densities $|n| = 10^{12}$ (panel a) and 10^{13} cm^{-2} (panel b).

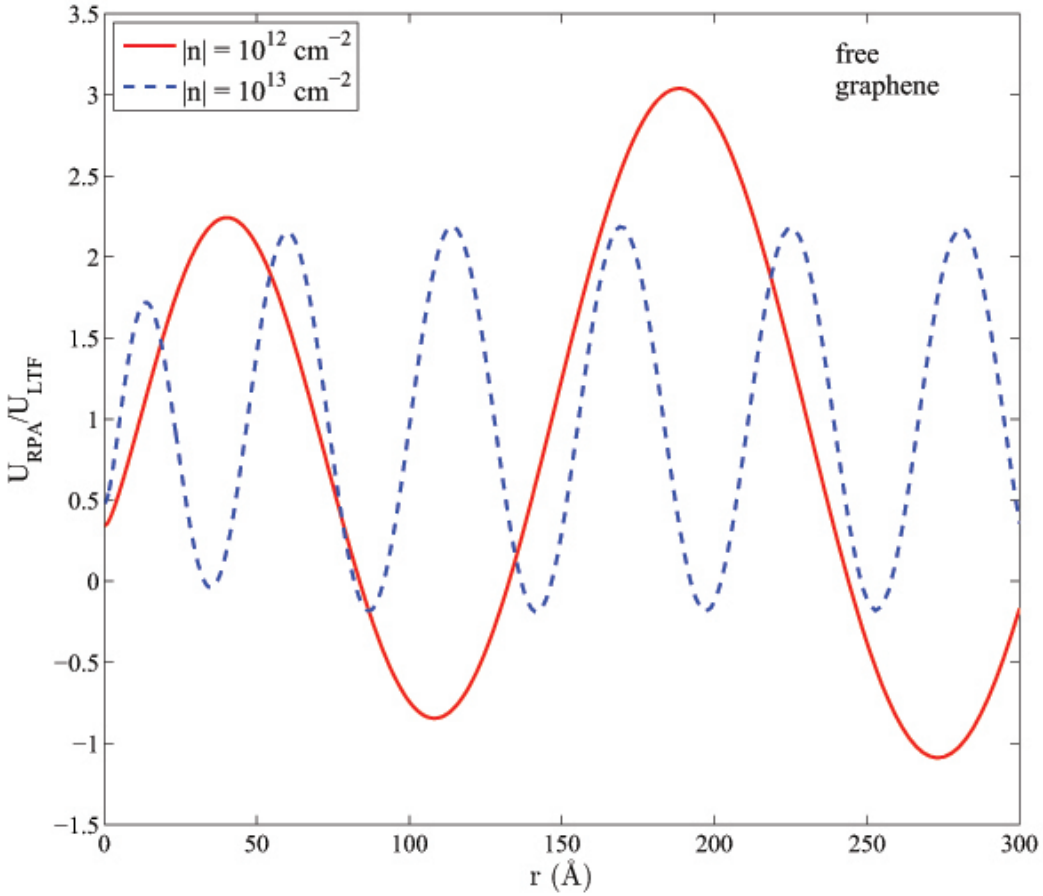

Figure 5.6: The ratio $U_{\mathrm{RPA}}/U_{\mathrm{LTF}}$ of the potential energies U_{RPA} and U_{LTF}, corresponding to, respectively, the RPA and LTF models of the equilibrium charge carrier densities $|n| = 10^{12}$ (solid [red] line), and $|n| = 10^{13}$ cm^{-2} (dashed [blue] line), is shown as a function of the radial distance r (in Å) in the plane of free graphene for a proton at distance $z_0 = 2$ Å above the graphene, with $T = 0$.

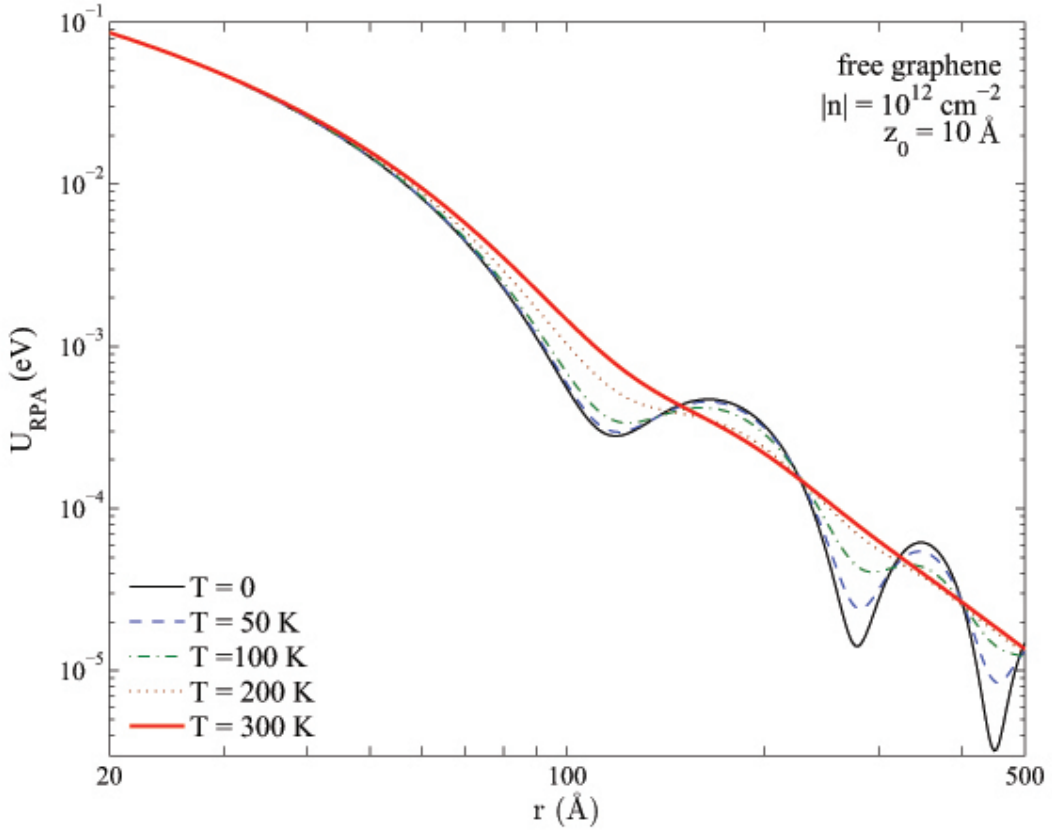

Figure 5.7: The RPA potential energy, (in eV), due to an external proton at distance $z_0 = 10$ Å from free graphene at $T = 0$ (thin [black] solid line), $T = 50$ K ([blue] dashed line), $T = 100$ K ([green] dashed-dotted line), $T = 200$ K ([red] dotted line), and $T = 300$ K (thick [red] solid line), as a function of the radial distance r (in Å) in the plane of free graphene, for equilibrium density of charge carriers $|n| = 10^{12}$ cm^{-2}.

and dashed [blue] line, respectively) for free graphene. Again the change in sign of the RPA potential is clear. Both magnitude and wavelength of oscillations decrease on increasing the density of charge carrier, indicating that wavelengths scale with k_F^{-1}. However, the wavelength of oscillations is independent of r, but, with increasing r, the magnitude of oscillations increases asymptotically to a maximum.

The effect of temperature in the RPA model is shown in Fig. 5.7, in which the RPA result due to an external proton at distance $z_0 = 10$ Å from free graphene, at different temperatures for equilibrium density $|n| = 10^{12}$ cm^{-2} is shown. As expected, non-zero temperature suppresses the Friedel oscillations, particularly at large distances where the total potential is weak. Even low temperature $T = 50$ K shows a strong damping of the oscillations, while room temperature, $T = 300$ K, is high enough to almost eliminate the oscillations.

5.4 Nonlinear Screening

Nonlinear effects in screening of an external charge by doped graphene, seen in Figs. 5.1(b1) and 5.2(a), are summarized in Fig. 5.8, with the inclusion of the results for doping density of $|n| = 10^{11}$ cm^{-2}. We show the ratio $U_-(r)/U_+(r)$ of the potential energies $U_-(r)$ and $U_+(r)$, which are obtained from Eq. (3.26) with, respectively, negative (hole doping) and positive (electron doping) signs of densities $|n| = 10^{11}$ (solid lines), 10^{12} (dashed lines), and 10^{13} cm^{-2} (dash-dotted lines), for a charge $Z = 1$ at two distances with two temperatures: $z_0 = 2$ Å and $T = 0$ (panel a), $z_0 = 10$ Å and $T = 0$ (panel b), and $z_0 = 10$ Å and $T = 300$ K (panel c), for graphene lying on an SiO_2 substrate with the gap $h = 1$ Å. One notices in Fig. 5.8 that the ratio $U_-(r)/U_+(r)$ may reach quite large values (up to 2), indicating that nonlinear effects in screening of external charges may be very strong. In particular,

this ratio reaches maximum values at certain distances r_c that clearly depend on both the doping density $|n|$ and the strength of external perturbation determined by z_0. [We note that the difference $U_-(r) - U_+(r)$ is always found to peak at $r = 0$.]

The maxima in the ratios, seen in Fig. 5.8, may be explained by the fact that, for the hole doping ($n < 0$) of graphene in the presence of a positive external charge, there will be a local re-doping with electrons, or discharging of graphene, giving rise to a local shift of the π electron band DOS, such that the condition $U_-(r_c) \approx \hbar v_F k_F$ may be reached, indicating that the Fermi level is pushed back to cross the neutrality point at some distance $r = r_c$. Since there are fewer states available in the DOS around the neutrality point, the screening ability of graphene is reduced around $r = r_c$ when $n < 0$, resulting in a higher value of the total potential than in the case of electron doping ($n > 0$), so that one may expect that an inequality $U_-(r) > U_+(r) > 0$ will hold for a range of distances r around r_c. For example, in Fig. 5.8(a), the external charge is so close to graphene at zero temperature that it provides a strong enough perturbation, giving rise to the local discharging for all three doping densities, $|n| = 10^{11}$, 10^{12}, and 10^{13} cm^{-2}, so that three maxima in the ratio $U_-(r)/U_+(r)$ occur around distances $r_c \approx 35.6$, 12.7, and 4.8 Å, respectively. The corresponding values of the potential $U_-(r_c)$ at these distances are found to be 0.037, 0.137, and 0.495 eV, respectively, which scale reasonably close to the Fermi level shift at the three doping densities, $|\varepsilon_F| = \hbar v_F k_F \approx 0.037$, 0.117, and 0.368 eV.

On the other hand, when the charge is removed to distance $z_0 = 10$ Å at zero temperature in Fig. 5.8(b), the perturbation is still strong enough to discharge graphene for the two lower doping densities [with the peaks occurring at similar distances, $r_c \approx 47.8$ and 15.0 Å, and with similar potential values, $U_-(r_c) \approx 0.041$ and 0.153 eV, as in Fig. 5.8(a)], but is not sufficient to force the Fermi level to

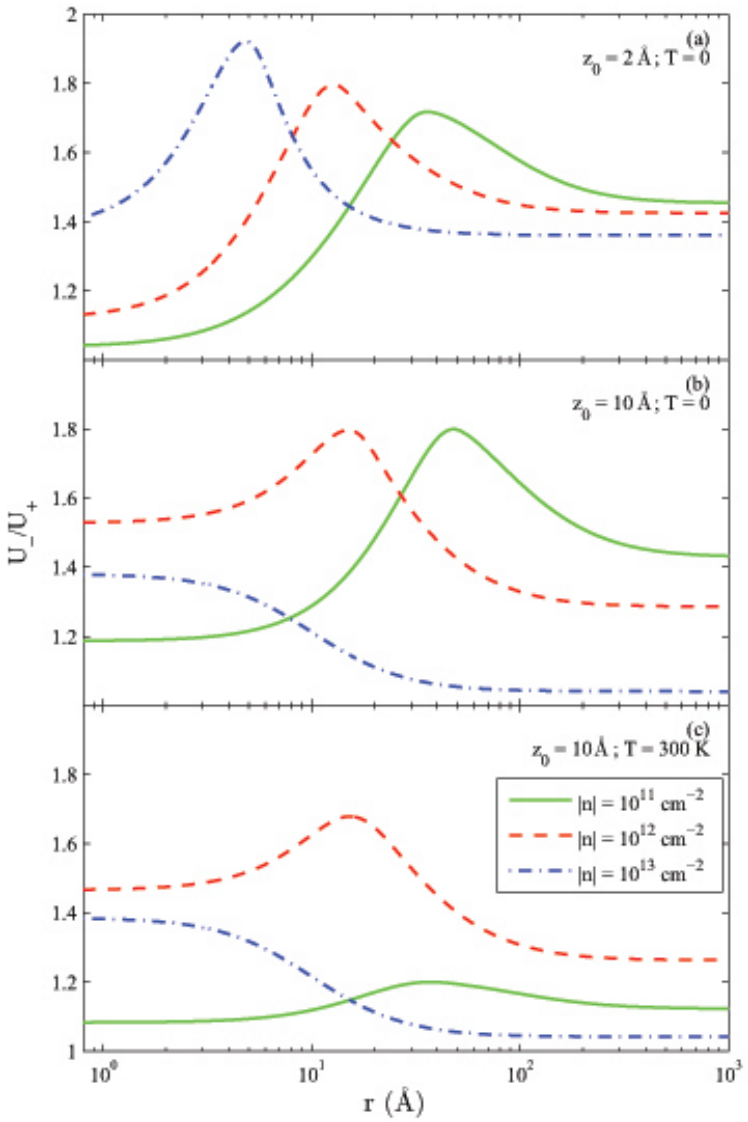

Figure 5.8: The ratio $U_-(r)/U_+(r)$ of the nonlinear potential energies $U_-(r)$ and $U_+(r)$ corresponding to, respectively, negative (hole doping) and positive (electron doping) signs of the equilibrium charge carrier densities $|n| = 10^{11}$ (solid [green] lines), 10^{12} (dashed [red] lines), and 10^{13} cm^{-2} (dash-dotted [blue] lines), is shown as a function of the radial distance r (in Å) in the plane of graphene for a proton at distances $z_0 = 2$ Å with $T = 0$ (panel a), $z_0 = 10$ Å with $T = 0$ (panel b), and $z_0 = 10$ Å with $T = 300$ K (panel c), above graphene lying on an SiO_2 substrate with the gap $h = 1$ Å.

cross the neutrality point for the highest density of $|n| = 10^{13}$ cm^{-2}, for which a maximal local discharging of graphene occurs directly below the external charge. Furthermore, when the temperature is raised to $T = 300$ K for $z_0 = 10$ Å, the ratio $U_-(r)/U_+(r)$ for the two higher doping densities is barely affected, but the ratio for the lowest density $|n| = 10^{11}$ cm^{-2} appears to be largely suppressed in Fig. 5.8(c) as compared to Fig. 5.8(b). One can still see a maximum in this ratio around a distance similar to that in Fig. 5.8(b), i.e., $r_c \approx 37.2$ Å with $U_- \approx 0.045$ eV, but the peak value of the ratio $U_-(r)/U_+(r)$ for $|n| = 10^{11}$ cm^{-2} has dropped from about 1.8 for $T = 0$ to about 1.2 for $T = 300$ K. While the results in Fig. 5.8(c) confirm the conclusion drawn from Fig. 5.2 that, at room temperature, the screening ability of graphene is affected for sufficiently low doping densities, such that $|n| \lesssim 10^{11}$ cm^{-2}, it is now clear that the role of elevated temperature, when it prevails over the effects of doping density, is to the suppress the nonlinear effects.

5.5 Effects of the Nonlinear DOS and Exchange and Correlation Interaction

All results shown in Figs. 1-8 were obtained by taking into account in Eq. (2.70) the effects of nonlinearity in the band DOS of graphene, $\rho(\varepsilon)$, because we suspected that the value of the potential $U(r)$ may exceed locally (that is, directly bellow the external charge) the cutoff value of about 1 eV that validates the linear approximation for $\rho(\varepsilon)$. Our calculations show that the effect of this nonlinearity is relatively weak, giving corrections up to several percent for distances $|z_0| > 1.5$ Å. This is illustrated in Fig. 5.9 for free, intrinsic ($\mu = 0$) graphene at zero temperature with a charge $Z = 1$ placed at $z_0 = 2$ Å, where we show by the dash-dotted line the

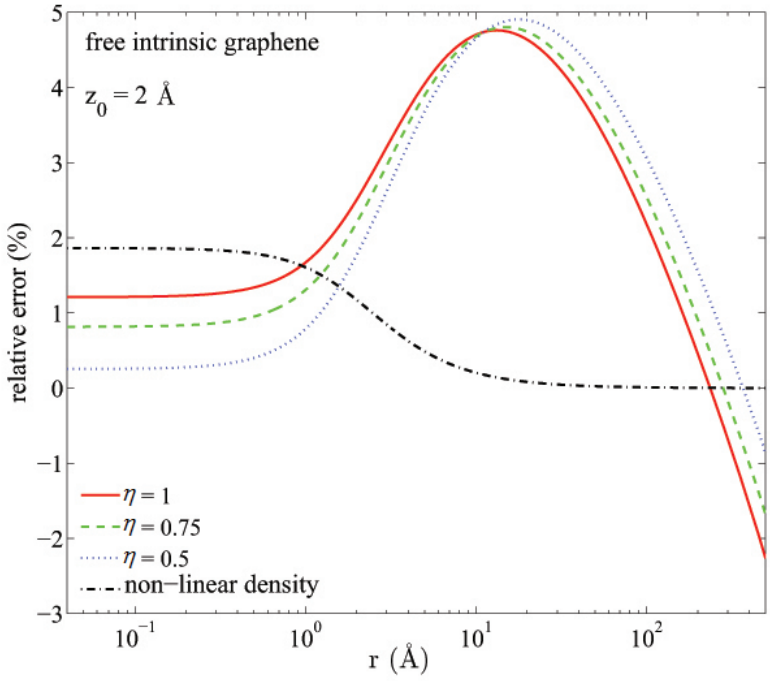

Figure 5.9: The relative error in the potential energy, $U(r) = e\phi(r)$ (in %), from the nonlinear TF model for a proton at distance $z_0 = 2$ Å from free, intrinsic ($n = 0$) graphene at zero temperature, due to the inclusion of the exchange and correlation energies [29], with values of the cutoff parameter $\eta = 1$ (solid [red] line), 0.75 (dashed [green] line), and 0.5 (dotted [blue] line), as well as due to the nonlinear correction to graphene's π electron band density of states (dash-dotted [black] line).

relative error in the total potential when Eq. (3.26) is solved with density n from Eq. (2.73) and from Eq. (2.70) with a nonlinear DOS $\rho(\varepsilon)$ [11]. One can see that the peak error of about 2 % occurs at the origin and diminishes at distances greater than a few Angstroms.

We further estimate the effects of the exchange and correlation interactions, which have been neglected so far in solving the nonlinear TF equation (3.26). We use the expression $V_{\rm xc}(n)$ for the XC potential energy given by Polini *at al.*[29] in the

LDA and, since the formalism providing $V_{\rm xc}(n)$ is restricted to intrinsic graphene at zero temperature within the linear approximation for $\rho(\varepsilon)$ [29], we solve the nonlinear equation, Eq. (3.42) with Eq. (3.43), for free graphene ($\epsilon^0_{\rm bg} = 1$) with the charge $Z = 1$ a distance $z_0 = 2$ Å away. The result is compared to the solution when $V_{\rm xc}$ is set to zero by showing in Fig. 5.9 the relative error of such a comparison for several values of the cutoff parameter η [29]. One can see in Fig. 5.9 that the relative error due to the XC interactions is relatively small at short distances r, and is comparable to the error due to the nonlinear band DOS. However, the error due to the XC interactions increases and reaches a maximum of about 5% at distances on the order of $r = 10$ Å or more, changes its sign at still greater distances of about $r = 100$ Å or more, and presumably continues growing further in magnitude. While this is a relatively small error at radial distances where the total potential has a significant value, we note that the error due to the XC interaction may be larger when external charge is placed further away from graphene, as noted in Ref.[29]. However, because of the limitation of the theory for XC interactions to local perturbations of charge carrier density relative to intrinsic graphene at $T = 0$ [28, 29], we no longer pursue the analysis of the XC effects in our nonlinear TF approach.

5.6 Image Interaction

While the results in Figs. 1-9 clearly local properties of the solution of the nonlinear TF equation, Eq. (3.26), we now turn to analyzing the image force $F_{\rm im}$ on a point charge as a quantity that provides integrated information on the effects of doping and nonlinear screening in graphene. We first consider free graphene at $T = 0$, and represent the nonlinear image force in the form reminiscent of the classical image

force of a point charge Ze in vacuum, a distance z_0 away from a layer of dielectric material with an effective dielectric constant ϵ_*, given by

$$F_{\rm im} = \frac{(Ze)^2}{4z_0^2}\left[\frac{1}{\epsilon_*(z_0)} - 1\right]. \tag{5.1}$$

In this way, the z_0 dependent parameter ϵ_* provides a measure of the polarizability of free graphene. We use the same line styles and thicknesses as in Fig. 5.1 to show in Fig. 5.10 the results of the nonlinear TF calculations of ϵ_* as a function of z_0 for $|n| = 0$, 10^{12}, and 10^{13} cm^{-2}, along with the corresponding LTF and RPA results obtained from Eq. (3.98) with an appropriate polarization function by taking the derivative, $F_{\rm im} = -dV_{\rm im}/dz_0$. One can see in Fig. 5.10 a strong dependence of the nonlinear TF image force on both the magnitude and the sign of charge carrier density n, whereas the linear results seem to work only at large enough distances z_0, with the RPA model showing better agreement with the nonlinear TF results than with the LTF model. We note that the slopes of the LTF lines follow from taking the derivative of the asymptotic limit of the image potential in Eq. (3.100), and are given for $n \neq 0$ by the zero temperature limit of the inverse screening length in Eq. (3.36), $q_s = 4r_s k_F$. On the other hand, the nearly horizontal lines for the nonlinear TF and the RPA models with $n = 0$ show that intrinsic graphene behaves as a layer of material with effective dielectric constants of ≈ 3.57 and $\approx 1 + \pi r_s/2 \approx 4.44$, respectively.

We analyze in Fig. 5.11 the image potential on a point charge $Z = 1$ above free graphene (panel a) and in the presence of a SiO_2 substrate with zero gap (panel b), at zero temperature. We show the results due to the nonlinear TF and the RPA models for $n = 0$ (thick solid and dotted lines, respectively) and $\pm 10^{13}$ cm^{-2} (thin solid and dashed lines for the nonlinear TF, and thin dotted line for the RPA model), as well as the results due to the LTF model for $|n| = 10^{13}$

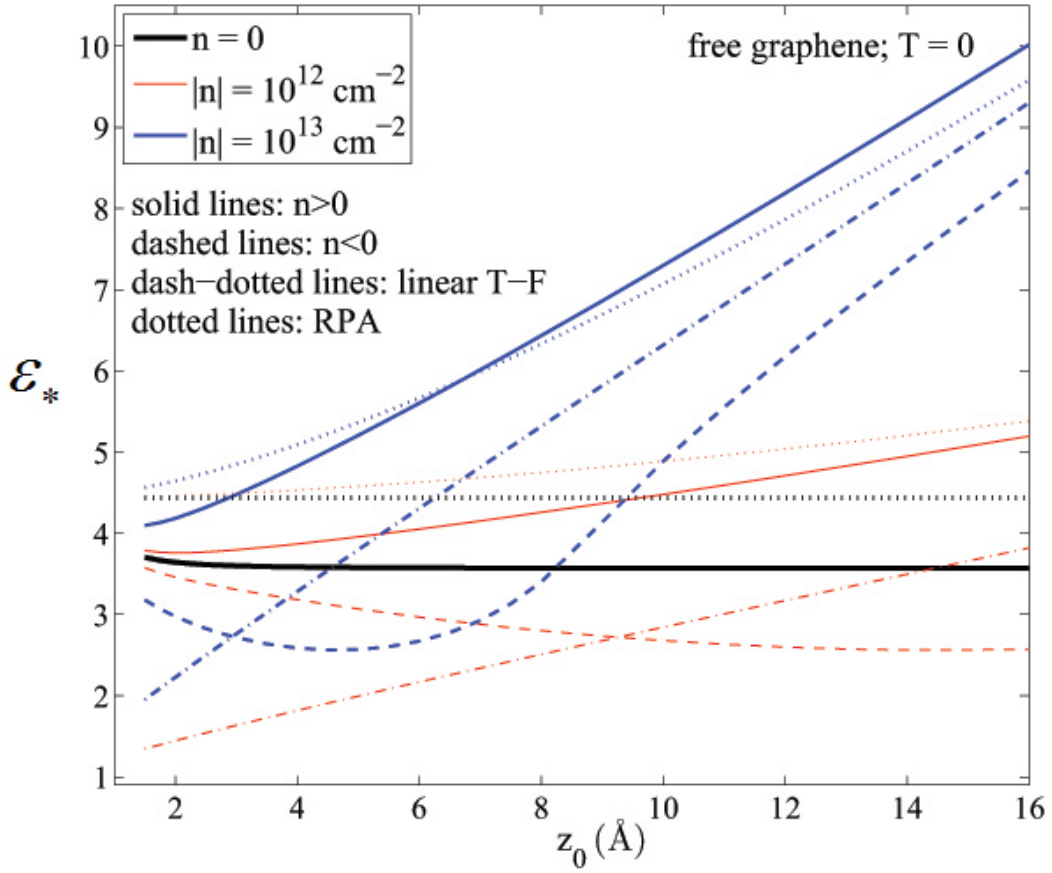

Figure 5.10: The effective dielectric constant ϵ_* in the image force, written as $F_{\rm im} = -(Ze/2z_0)^2(1/\epsilon_* - 1)$, as a function of distance z_0 (in Å) for a proton above free graphene at $T = 0$. Results from the nonlinear TF model are shown for equilibrium densities $n = 0$ (lower thick [black] solid line), $\pm 10^{12}$ (thin [red] solid and dashed lines, respectively), and $\pm 10^{13}$ cm^{-2} (upper thick [blue] solid and dashed lines, respectively). Results from the linearized TF model and the RPA model are shown, respectively, by dash-dotted and dotted lines for densities $|n| = 0$ (lower thick [black] lines), 10^{12} (thin [red] lines), and 10^{13} cm^{-2} (upper thick [blue] lines).

cm^{-2} (thin dash-dotted line). We note that the nonlinear results were obtained by integrating the corresponding image force from z_0 up to typically 400 Å. One notices a relatively close grouping of all results, indicating that the linear models provide good approximations, especially at high density and large distances z_0.

However, the effects of doping of graphene are seen to be still quite strong, giving, e.g., in the nonlinear TF model for free graphene the image potential of $V_{\rm im} \approx -0.33$ eV at $z_0 = 10$ Å when $|n| = 10^{13}$ cm^{-2}, as opposed to $V_{\rm im} \approx -0.26$ eV found at the same distance above intrinsic graphene. This points to possibly strong effects of doping in the asymptotic region of distances of relevance to the image potential states [36]. While the discrepancy between the RPA and the nonlinear TF results, seen in Fig. 5.11 for free graphene at zero doping, stems from the difference seen in Fig. 5.10 between the effective dielectric constants of intrinsic graphene in those two models, one notices very good agreement of the RPA model with the nonlinear TF model in graphene doped by electrons to $n = 10^{13}$ cm^{-2}. However, nonlinear effects are still quite strong, especially at short distances, as illustrated by the observed asymmetry in the nonlinear TF model with respect to the sign of $n \neq 0$. For example, one finds in Fig. 5.11(a) that the image potential takes the value of $V_{\rm im} \approx -2$ eV at $z_0 \approx 1.5$ Å above free graphene with $n = 10^{13}$ cm^{-2}, as opposed to $V_{\rm im} \approx -1.64$ eV at the same distance with $n = -10^{13}$ cm^{-2}. This asymmetry due to doping of graphene by electrons or holes may have interesting and important consequences for, e.g., chemisorption of a Li atom, where the image potential shift of its $2s$ orbital level may be controlled by the applied gate potential and used to move around the resonance in the local DOS, and even possibly break the ionic bond between the Li atom and graphene. We note that we have estimated numerically the effects of non-zero temperature and the XC interactions in the nonlinear image potential for intrinsic graphene, and found that both these effects

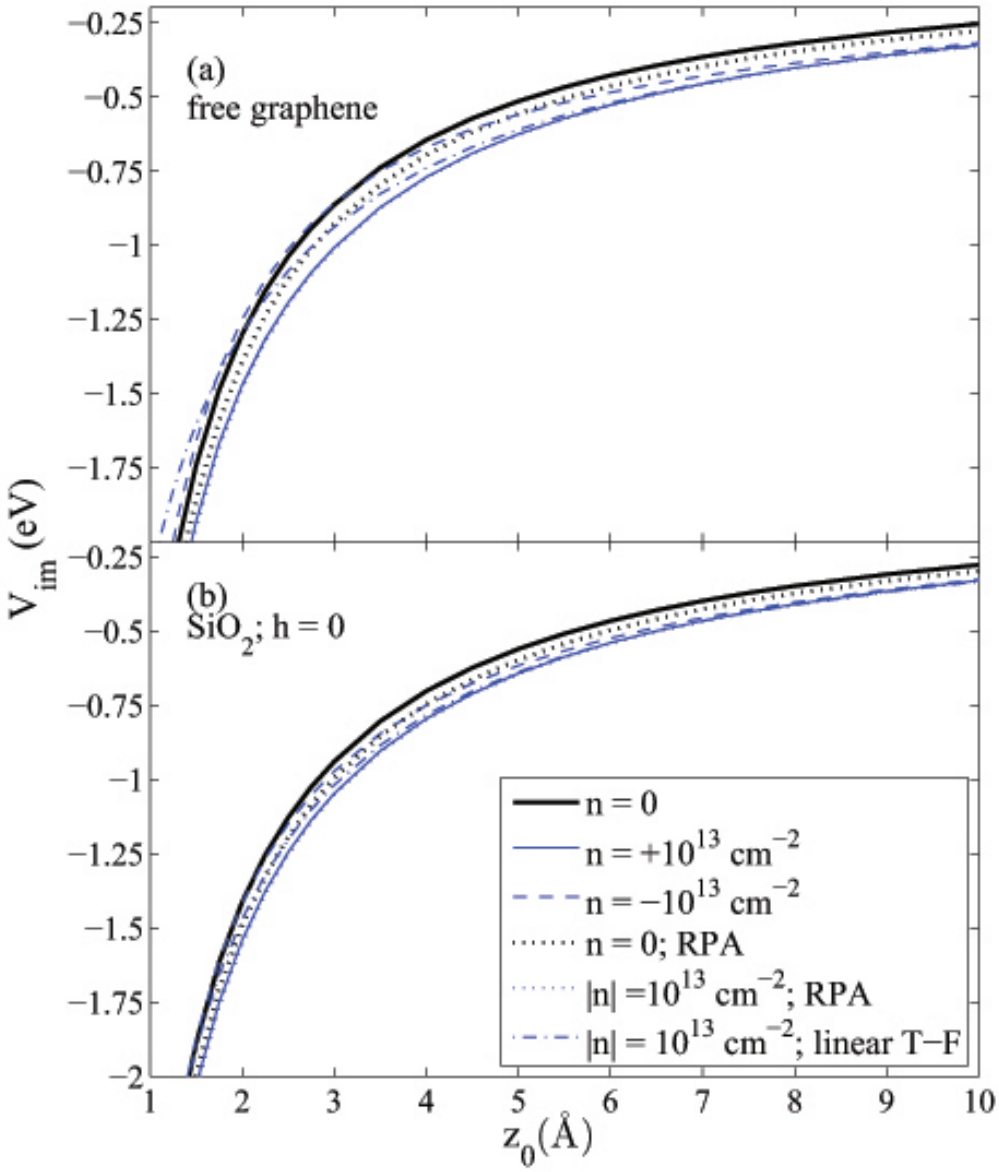

Figure 5.11: Results from the nonlinear TF model are shown for equilibrium densities $n = 0$ (upper thick [black] solid line) and $\pm 10^{13}$ cm^{-2} (lower thin [blue] solid and dashed lines, respectively). Results from the RPA model are shown by dotted lines for densities $|n| = 0$ (upper thick [black] line) and 10^{13} cm^{-2} (lower thin [blue] line), as well as from the linearized TF model for density $|n| = 10^{13}$ cm^{-2} (thin [blue] dash-dotted line).

are negligible compared to the above effects of the doping density and nonlinear screening.

Finally, we analyze the image force on a point charge in the presence of a SiO_2 substrate with the gap $h = 4$ Å at $T = 0$. In Fig. 5.12 we show the image force versus distance in the range $|z_0| \leq 10$ Å, going from a region deep inside the substrate to distances well above the graphene. In this way, we analyze the screening effects of the substrate. In Fig. 5.12, nonlinear results are shown only for intrinsic graphene and for the highest density of $|n| = 10^{14}$ cm^{-2}, whereas the linear results cover a full range of densities. We note that the nonlinear results for intermediate densities are concentrated in a relatively narrow range between the cases $n = 0$ and $|n| = 10^{14}$ cm^{-2}, whereas the linear results are much more spread out. One can see that the nonlinear effects in the image force are strongest close to graphene, whereas they almost completely vanish close to the surface of the substrate and inside its bulk. It is interesting to note that the variation with the sign of n is also strong even at such high density as $|n| = 10^{14}$ cm^{-2}, as noticed in all previous examples. The linear results in Fig. 5.12 are seen to be a rather poor approximation at distances close to graphene and at low densities $|n|$, but they gradually improve inside the substrate and at large densities.

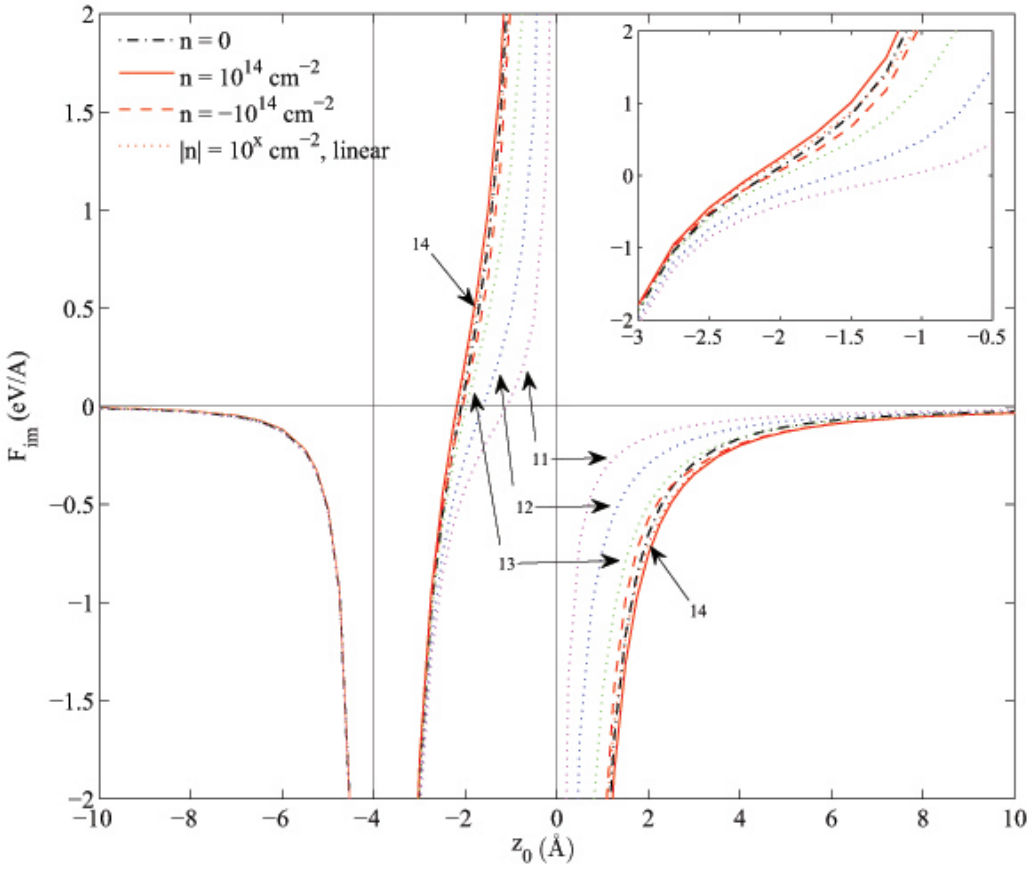

Figure 5.12: The image force $F_{\rm im}$ (in eV/Å) on a proton as a function of position z_0 (in Å), with graphene placed at $z_0 = 0$ and an SiO_2 substrate occupying the region $z_0 \leq -4$ Å, at $T = 0$. Nonlinear results are shown for $n = 10^{14}$ cm^{-2} (solid red curves) and $n =$ -10^{14} cm^{-2} (dashed red curves), as well as for intrinsic graphene ($n = 0$, black dash-dot curves). The linear results are shown by dotted (red, blue, green and pink) curves for $|n| = 10^{11}$, 10^{12}, 10^{13}, and 10^{14} cm^{-2}, displaying an increasing degree of divergence from the nonlinear curves with decreasing values of $|n|$.

Chapter 6

Conclusion

6.1 Concluding Remarks

We have solved a nonlinear TF equation for the radial dependence of electric potential in the plane of single-layer graphene due to an external point charge in the presence of a dielectric substrate with a graphene-substrate gap, h, paying special attention to the effects of equilibrium charge carrier density n, temperature T, and separation $|z_0|$ between the charge and graphene. Large effects were found due to variations in both the magnitude and the sign of n, illustrating the importance of both doping of graphene and the nonlinear screening, respectively. Temperature was found to mostly affect screening at low doping densities, satisfying the inequality $k_F = \sqrt{\pi|n|} \lesssim k_B T/(\hbar v_F)$, in such a way as to suppress the nonlinear effects. In addition, the existence of a non-zero gap, h, between the substrate and graphene was found to exert non-negligible effects on the potential, mostly at short radial distances. We have moreover analyzed the effects in the potential due to nonlinear corrections in the density of states of graphene's π electron bands, as well as due to the exchange and correlation interactions for the case of free, intrinsic graphene at $T = 0$. While the former effect gives corrections of up to a few percent at positions directly bellow the external charge and diminishes at distances further out, the latter effect gives rise to the corrections of up to 5 % at intermediate and large radial distances.

Comparisons were made with the results from a linearized TF (LTF) equation and from the RPA model of dielectric screening in graphene. While the LTF results are generally close to the nonlinear TF results at large radial distances and high densities $|n|$ only, the RPA model also exhibits an improved agreement with the nonlinear TF model at short radial distances, owing to the short wavelength dielectric constant of graphene, which results from the inter-band electron transitions

captured by the RPA model [44, 29]. Unlike the TF models, the RPA results exhibit Friedel oscillations around the potential from the linearized TF model at large radial distances in doped graphene, with amplitudes that increase with increasing gap h, but are dampened by increasing separation $|z_0|$ and increasing temperature.

Our most important conclusion is that nonlinear effects are strong over a broad range of radial distances, even at high doping densities $|n|$ and large separations $|z_0|$, as illustrated by the large ratios of the potentials evaluated from the nonlinear TF model with the same amounts of doping by holes ($n < 0$) and by electrons ($n > 0$). This may be explained by a local shift of graphene's density of states so that the Fermi level is forced to cross the neutrality point in that density of states at a certain radial distance, thereby reducing graphene's polarizability when doping occurs with carriers of the same charge sign as the external particle. This asymmetry in the scattering potential for charge carriers in graphene with respect to the sign of n may be responsible for the observed asymmetry in graphene's conductivity as the sign of the gate potential changes [59]. However, such an effect of nonlinear screening of external charges will be suppressed at low doping densities when the temperature is sufficiently elevated, as described above.

Finally, we have analyzed the image interaction of an external charge due to polarization of graphene, where we compared the results evaluated from the solution of the nonlinear TF equation with those from the LTF and RPA models. After elucidating the strong doping and nonlinear effects in the image force above free graphene at zero temperature, we have presented results for an image potential obtained by numerical integration of the nonlinear image force up to large distances from graphene, and compared them with the results of the linear models. The nonlinear image potential was found to exhibit relative variations due to doping of graphene up to $|n| = 10^{13}$ cm^{-2}, which can reach about 30 % at distances $|z_0| \sim 10$

Å, as well as due to the nonlinear screening, where relative variation with the sign of n may reach some 20 % at short distances, on the order of $|z_0| \sim 1$ Å. These variations in the image potential were found to be somewhat reduced in the presence of an SiO_2 substrate.

Our results for the electric potential in the plane of graphene due to external charge may be relevant for calculations of its conductivity based on the Boltzmann transport model [11, 19], where this potential may be used directly in an expression for the transport relaxation time in the Born approximation, to reveal the effects of doping, nonlinear screening and temperature on conductivity. While this task is left for a future contribution, we comment here that our nonlinear TF results are likely to yield calculable effects due to the asymmetry in charge of the external particles [59], based on the presently observed asymmetry with respect to the sign of n for a positive external charge. Moreover, our results for the nonlinear image potential may be found helpful in studying chemical processes near graphene, e.g., alkali atom chemisorption and intercalation [32], as well as in the recent work on the electron image-potential states near graphene [36].

References

[1] R. F. Curl, Rev. Mod. Phys. **69**, 691 (1997). 2

[2] H. Kroto, Rev. Mod. Phys. **69**, 703 (1997). 2

[3] R. E. Smalley, Rev. Mod. Phys. **69**, 723 (1997). 2

[4] S. Iijima, Nature **354**, 56 (1991). 2

[5] K. S. Novoselov, A. K. Geim, S. V. Morozov, D. Jiang, Y. Zhang, S. V. Dubonos, I. V. Grigorieva, and A. A. Firsov, Science **306**, 666 (2004). 2, 5

[6] D. S. L. Abergel, A. Russell, and V. I. Fal'ko, Appl. Phys. Lett. **91**, 063125 (2007). 3

[7] P. R. Wallace, Phys. Rev. **71**, 622 (1947). 3

[8] E. W. Hill, A. K. Geim, K. Novoselov, F. Schedin, and P. Blake, IEEE Trans. Magn. **42**, 2694 (2007). 4

[9] K. Nakada and M. Fujita, Phys. Rev. B **54**, 17954 (1996). 4

[10] F. Schedin, A. K. Geim, S. V. Morozov, E. W. Hill, P. Blake, M. I. Katsnelson, and K.S. Novoselov, Nature Materials **6**, 652 (2007). 5, 6

[11] A. H. C. Neto, F. Guinea, N. M. R. Peres, K. S. Novoselov, and A. K. Geim, Rev. Mod. Phys. **81**, 109 (2009). 5, 6, 7, 32, 93, 104

[12] Y. W. Tan, Y. Zhang, K. Bolotin, Y. Zhao, S. Adam S, E. H. Hwang, S. Das Sarma, H. L. Stormer, and P. Kim, Phys. Rev. Lett. **99**, 246803 (2007). 5

[13] J. H. Chen, C. Jang, S. Adam, M. S. Fuhrer, E. D. Williams, and M. Ishigami, Nature Physics **4**, 377 (2008). 5

[14] A. Das, S. Pisana, B. Chakraborty, S. Piscanec, S. K. Saha, U. V. Waghmare, K. S. Novoselov, H. R. Krishnamurthy, A. K. Geim, A. C. Ferrari, and A. K. Sood, Nature Nanotechnology **3**, 210 (2008). 5

[15] X. Du, I. Skachko, A. Barker, and E. Y. Andrei, Nature Nanotechnology **3**, 491 (2008). 5

[16] K. I. Bolotin, K. J. Sikes, J. Hone, H. L. Stormer, and P. Kim, Phys. Rev. Lett. **101**, 096802 (2008). 5

[17] T. Ando, J. Phys. Soc. Japan **75**, 074716 (2006). 5, 6, 8, 49, 56, 57

[18] S. Adam, E. H. Hwang, V. M. Galitski, and S. Das Sarma, PNAS **104**, 18392 (2007). 5

[19] S. Adam, E. H. Hwang, E. Rossi, and S. Das Sarma, Solid State Communications **149**, 1072 (2009). 5, 104

[20] A. V. Shytov, M. I. Katsnelson, and L. S. Levitov, Phys. Rev. Lett. **99**, 236801 (2007). 5

[21] D.S. Novikov, Phys. Rev. B **76**, 245435 (2007). 5

[22] V. M. Pereira, V. N. Kotov, and A. H. C. Neto, Phys. Rev. B **78**, 085101 (2008). 5

[23] I. S. Terekhov, A. I. Milstein, V. N. Kotov, and O. P. Sushkov, Phys. Rev. Lett. **100**, 076803 (2008). 5

[24] D. P. DiVicenzo and E. J. Mele, Phys. Rev. **29**, 1685 (1984). 5, 6, 7, 76, 82

[25] M. I. Katsnelson, Phys. Rev. B **74**, 201401(R) (2006). 5, 6, 7, 49, 76

[26] M. M. Fogler, D. S. Novikov, and B. I. Shklovskii, Phys. Rev. B **76**, 233402 (2007). 5, 6, 7, 76

[27] I. Radovic, L. J. Hadzievski, and Z. L. Miskovic, Phys. Rev. B **77**, 075428 (2008). 5, 6, 7, 42, 46, 47

[28] E. Rossi and S. Das Sarma, Phys. Rev. Lett. **101**, 166803 (2008). 5, 7, 50, 94

[29] M. Polini, A. Tomadin, R. Asgari, and A. H. MacDonald, Phys. Rev. B **78**, 115426 (2008). xx, 5, 7, 8, 50, 51, 52, 54, 77, 80, 93, 94, 103

[30] Y. Wu and M. A. Shannon, J. Micromech. Microeng. **14**, 989 (2004). 5, 80

[31] C.A. Rezende, R.F. Gouveia, M.A. da Silva, and F. Galembeck, J. Phys. - Cond. Matt. **21**, 263002 (2009). 5, 80

[32] k. T. Chan, J. B. Neaton, and M. L. Cohen, Phys. Rev. B **77**, 235430 (2008). 6, 76, 77, 79, 82, 104

[33] A. H. C. Neto, V. N. Kotov, J. Nilsson, V. M. Pereira, N. M. R. Peres, and B. Uchoa, Solid State Communications **149**, 1094 (2009). 6

[34] J. Algdal, T. Balasubramanian, M. Breitholtz, T. Kihlgren, and L. Wallden, Surf. Sci. **601**, 1167 (2007). 6, 82

[35] G. Gumbs, D. Huang, and P.M. Echenique, Phys. Rev. B **79**, 035410 (2009). 6, 8

[36] V.M. Silkin, J. Zhao, F. Guinea, E.V. Chulkov, P.M. Echenique, and H. Petek, Phys. Rev. B **80**, 121408 (2009). 6, 8, 80, 97, 104

[37] K.F. Allison, D. Borka, I. Radovic, L. J. Hadzievski, and Z. L. Miskovic, Phys. Rev. B **80**, 195405 (2009). 6, 61, 62, 80

[38] M. Ishigami, J. H. Chen, W. G. Cullen, M. S. Fuhrer, and E. D. Williams, Nano Letters **7**, 1643 (2007). 6, 82

[39] S. Fratini and F. Guinea, Phys. Rev. B **77**, 195415 (2008). 6

[40] C. Jang, S. Adam, J. H. Chen, D. Williams, S. Das Sarma, and M. S. Fuhrer, Phys. Rev. Lett. **101**, 146805 (2008). 6

[41] F. Chen, J. L. Xia, and N. J. Tao NJ, Nano Letters **9**, 1621 (2009). 6

[42] F. Chen, J. L. Xia, D. K. Ferry, and N. J. Tao, Nano Letters **9**, 2571 (2009). 6

[43] B. Wunsch, T. Stauber, F. Sols, and F. Guinea, New Journal of Physics **8**m 318 (2006). 6, 8, 61, 79

[44] E.H. Hwang and S. Das Sarma, Phys. Rev. B **79**, 165404 (2007). 6, 8, 103

[45] L. Brey mand H.A. Fertig, Phys. Rev. B **80**, 035406 (2009). 7, 50, 79, 80

[46] G. S. Painter and D. E. Ellis, Phys. Rev. B **1**, 4747 (1970). 14

[47] J.-C. Charlier, P. C. Eklund, J. Zhu, and A. C. Ferrari, Topics in Applied Physics **111**, 673 (2008). xv, 15, 18

[48] S. Reich, J. Maultzsch, C. Thomsen, and P. Ordejón, Phys. Rev. B **66**, 035412 (2002). xv, 15, 18

[49] R. S. Deacon, K.-C. Chuang, R. J. Nicholas, K. S. Novoselov, and A. K. Geim, Phys. Rev. B **76**, 081406(R) (2007). 18

[50] J. P. Hobson and W. A. Nierenberg, Phys. Rev. **89**, 662 (1953). 29

[51] M. Abramowitz and I. A. Stegun, *Handbook of Mathematical Functions*, (National Bureau of Standards, Washington, 1965). 29, 32, 49

[52] V. Ryzhii, A. Satou, and T. Otsuji, Journal of Applied Physics **101**, 024509 (2007). 36

[53] P. Hohenberg and W. Kohn, Phys. Rev. **136**, B864 (1964). 50

[54] T. P. Doerr and Y. K. Yu, Am. J. Phys. **72**, 190 (2004).

[55] D. J. Mowbray, Z. L. Miskovic and F. O. Goodman, Phys. Rev. B **74**, 195435 (2006). 61

[56] N. D. Mermin, Phys. Rev. **137**, A1441 (1965). 46

[57] K. Yonei, J. Ozaki, and Y. Tomishima, J. Phys. Soc. Japan **56**, 2697 (1987). 46

[58] P.A. Khomyakov, G. Giovannetti, P.C. Rusu, G. Brocks, J. van den Brink, and P.J. Kelly, Phys. Rev. B **79**, 195425 (2009) 79

[59] D. B. Farmer, R. Golizadeh-Mojarad, V. Perebeinos, Y. M. Lin, G. S. Tulevski, J. C. Tsang, and P. Avouris, Nano Letter **9**, 388 (2009). 103, 104